

**Searches for New Physics in final states  
containing leptons,  $b$ -jets and  $E_T^{\text{miss}}$  at the  
ATLAS detector**



UNIVERSITY OF  

---

LIVERPOOL

Thesis submitted in accordance with the requirements of the  
University of Liverpool for the degree of Doctor in Philosophy by

**Matthew James Sullivan**

Department of Physics  
Oliver Lodge Laboratory  
University of Liverpool

September 2020

# Abstract

This is my abstract.

# Declaration

I hereby confirm this work is my own, except where other works are referenced. This work has not previously been submitted to any institute, including this one. This thesis does not exceed the relevant word count.

*Matthew James Sullivan*

---

# Acknowledgements

During my eight years at the University of Liverpool, the people helping to make it such a memorable period of my life have become innumerable, and to thank each and every person would require an equally long period of time. For those not acknowledged by name I can only give my thanks for being involved in this part of my life. It has been a true privilege to call this city my home and be a part of the Department of Physics throughout.

The first of many thanks goes to my mum, my dad and my sister, for their endless and unwavering support throughout my PhD. The level of support you all offer continues to astound me and I can only offer my gratitude in return. An honourable mention must go to my niece, Charlotte, who was born halfway through my PhD and has been the best niece one could ask for, although these words are, for now, lost on you.

Secondly, many thanks are owed to the non-physics friends, who have given me respite from the challenges of my PhD. Particularly, Holly, Brad, Pete, Alex, Ellie and Sean, who have supported and encouraged me through challenging professional and personal times. Your continued reminder to write this Thesis, however, is unforgiveable. Additionally, a big thanks to Hannah, who for the last ten years has been putting up with my nonsense, and hopefully will continue to do so. I hope over time I can begin to pay back the levels of support you have all given me.

These acknowledgements would be incomplete without a mention to the circumstances within which a large portion of it was written. The COVID-19 pandemic has had a devastating impact on individuals and families the world-over, causing both physical and mental struggle. On a personal level, numerous thanks are owed for enabling me to submit this work in this turbulent time. Firstly, to UKRI, for their generous financial support, enabling me to continue my work during these challenging times. Secondly, thanks are owed to the NHS, both due to their handling of the national crisis and for their continued healthcare support during, undoubtedly, the most stressful period of my life. However, the period of national lockdown due to the coronavirus has also provided unforeseen opportunities for personal development, and I submit this work having gained far more than anticipated. Countless thanks are owed to Jess, for managing to keep my stress-levels under control, for

---

the walks, the talks and the laughs. Without you, this work would have been submitted in a much heavier fashion.

Of course, many thanks are owed to the physics community within which I have been immersed. Firstly, to the Liverpool ATLAS group, who welcomed me into the collaboration in 2016 and have supported me throughout my PhD. The group, and the department, provided me with some incredible opportunities, for which I am extremely grateful. Secondly, to all of the physics friends, who have listened to my rants, help spot the bugs I couldn't find, and bluntly point out when I'm being stupid. Special thanks must go to James, Chips and Lauren for dealing with me when at my most difficult, and for the frequent trips to the pub, both in Liverpool and Geneva.

Finally, to my excellent supervisors, Monica D'Onofrio and Yanyan Gao. You have pushed me to levels beyond what I imagined I could achieve and have given me amazing opportunities for professional development. I can only apologise for being slow and stupid, and am extremely grateful for your patience in supervision.

# Contents

<b>List of Figures</b>	<b>x</b>
<b>List of Tables</b>	<b>xii</b>
<b>Introduction</b>	<b>1</b>
<b>I Theoretical overview and experimental apparatus</b>	<b>3</b>
<b>1 The Standard Model and Beyond</b>	<b>4</b>
1.1 The Standard Model . . . . .	4
1.2 Physics Beyond the Standard Model . . . . .	15
<b>2 The LHC and the ATLAS Experiment</b>	<b>21</b>
2.1 The LHC accelerator . . . . .	21
2.2 Luminosity and pileup . . . . .	22
2.3 ATLAS overview . . . . .	24
2.4 Magnet system . . . . .	26
2.5 Inner Detector . . . . .	27
2.6 Calorimetry . . . . .	29
2.7 Muon System . . . . .	31
2.8 ATLAS Trigger System . . . . .	32
<b>3 Data and Monte Carlo samples</b>	<b>34</b>
3.1 Datasets . . . . .	34
3.2 Monte Carlo simulation . . . . .	35
<b>4 Object reconstruction</b>	<b>47</b>
4.1 Reconstruction overview . . . . .	47
4.2 Leptons . . . . .	48
4.3 Jets . . . . .	52
4.4 $E_T^{\text{miss}}$ . . . . .	57
4.5 Overlap removal . . . . .	58

---

4.6	Event cleaning . . . . .	58
4.7	Object definitions summary . . . . .	59
<b>5</b>	<b>Analysis methods</b>	<b>61</b>
5.1	General search analysis strategy . . . . .	61
5.2	Discriminant variables . . . . .	62
5.3	Selection optimisation methods . . . . .	64
5.4	Estimating systematic uncertainties . . . . .	70
5.5	Statistical analysis . . . . .	73
<b>II</b>	<b>Searches for New Physics in Run-2 ATLAS data</b>	<b>77</b>
<b>6</b>	<b>Searches for <math>\tilde{\chi}_1^\pm \tilde{\chi}_2^0</math> pair-production</b>	<b>78</b>
6.1	SUSY signal model . . . . .	79
6.2	Event selection . . . . .	81
6.3	Background estimation . . . . .	81
6.4	Systematic uncertainties . . . . .	83
6.5	Results . . . . .	83
6.6	Studies with $139\text{fb}^{-1}$ . . . . .	89
<b>7</b>	<b>Search for Dark Matter production in association with a top quark</b>	<b>90</b>
7.1	2HDM+ $a$ signal model . . . . .	90
7.2	Event selection . . . . .	93
7.3	Background estimation . . . . .	94
7.4	Systematic uncertainties . . . . .	95
7.5	Results . . . . .	97
<b>III</b>	<b>High-Luminosity LHC studies</b>	<b>109</b>
<b>8</b>	<b>Sensitivity to <math>\tilde{\chi}_1^\pm \tilde{\chi}_2^0</math> pair-production at the HL-LHC</b>	<b>110</b>
8.1	MC simulation . . . . .	111
8.2	Detector simulation . . . . .	112
8.3	Event selection . . . . .	115
8.4	Systematic uncertainties . . . . .	119
8.5	Results . . . . .	121
	<b>Appendices</b>	<b>125</b>
<b>A</b>	<b>Sensitivity to <math>\tilde{\chi}_1^\pm \tilde{\chi}_2^0</math> pair-production at the HL-LHC</b>	<b>125</b>
A.1	Detector simulation parameterisations . . . . .	125

---

A.2	Cut & count studies . . . . .	129
A.3	Deep learning studies . . . . .	129
A.4	Extending $W$ +jets sample statistics . . . . .	132
<b>B</b>	<b>Testbeam studies of FE-I4 and RD53A performance at HL-LHC</b>	<b>134</b>
B.1	ATLAS ITk upgrade . . . . .	135
B.2	Experimental setup . . . . .	135
B.3	. . . . .	135
	<b>Bibliography</b>	<b>136</b>

# List of Figures

1.1	QED interaction vertex. . . . .	8
1.2	QCD interaction vertices. . . . .	9
1.3	Electroweak gauge boson interaction vertices. . . . .	11
1.4	Schematic of the Higgs potential. . . . .	12
1.5	Higgs interaction vertices . . . . .	14
1.6	SM Higgs branching ratios . . . . .	14
1.7	Running of SM coupling constants . . . . .	17
2.1	Diagram of the LHC accelerator complex . . . . .	22
2.2	Integrated luminosity as a function of time in Run-2 . . . . .	23
2.3	Pileup profile for Run-2 . . . . .	24
2.4	Diagram of the ATLAS detector . . . . .	25
2.5	Diagram of the ATLAS magnet system . . . . .	26
2.6	Diagram of the ATLAS Inner Detector . . . . .	27
2.7	Diagram of the ATLAS Calorimetry System . . . . .	30
2.8	Diagram of the ATLAS Muon Spectrometer . . . . .	32
2.9	Functional diagram of ATLAS trigger and DAQ system . . . . .	33
3.1	$E_T^{\text{miss}}$ trigger efficiency for 2015-2018 . . . . .	36
3.2	Overview of the MC simulation chain . . . . .	37
3.3	Feynman diagrams for $t\bar{t}$ at leading order . . . . .	38
3.4	Feynman diagrams for $Wt$ -channel single top at leading order . . . . .	40
3.5	Feynman diagrams for $Wt$ -channel single top at next-to-leading order . . . . .	41
3.6	Comparison of $E_T^{\text{miss}}$ distribution in CRST for DR and DS samples . . . . .	43
3.7	Comparison of $p_T^{b2}$ and $\Delta\phi(\ell, E_T^{\text{miss}})$ distributions in the proposed single top CR . . . . .	45
3.8	Comparison of $m_T$ and $m_{CT}$ distributions using $WWbb$ samples . . . . .	46
4.1	Representative diagram of particle signatures within ATLAS . . . . .	48
4.2	Electron identification efficiencies in Run-2 . . . . .	50
4.3	Muon reconstruction efficiencies in Run-2 . . . . .	51

---

4.4	Distributions of muon track- and calorimeter-based isolation . . . . .	52
5.1	Schematic diagram showing typical search regions configuration . . . . .	62
6.1	Diagram of $\tilde{\chi}_1^\pm \tilde{\chi}_2^0$ pair-production with a final state of 1 lepton, 2 $b$ -tagged jets and $E_T^{\text{miss}}$ . . . . .	79
6.2	Run-1 summary plot of searches for $\tilde{\chi}_1^\pm \tilde{\chi}_2^0$ pair-production . . . . .	79
6.3	Production cross-sections for various electroweak SUSY particles . . . . .	81
6.4	Post-fit distributions . . . . .	86
6.6	Exclusion limits for $\tilde{\chi}_1^\pm \tilde{\chi}_2^0$ production with $Wh$ signature . . . . .	88
7.1	Feynman diagram for the $tW$ +MET analysis . . . . .	91
7.2	Diagram of DM produced in association with a $t\bar{t}$ pair. . . . .	92
7.3	Production cross-section for DM plus top quark processes . . . . .	93
7.4	Key kinematic variables at preliminary selection level . . . . .	96
7.5	Post-fit $E_T^{\text{miss}}$ distributions in CRs . . . . .	101
7.6	Post-fit $E_T^{\text{miss}}$ distributions in VRs . . . . .	102
7.7	Post-fit N-1 distributions in SR . . . . .	103
7.8	Summary of data/MC agreement in all CR/VRs . . . . .	104
7.9	Exclusion limits for the DM $t$ signature . . . . .	105
7.10	Exclusion limits for the DM $t$ + $t\bar{t}$ signature . . . . .	106
8.1	Simulated $t\bar{t}$ event in the ATLAS ITk with $\langle\mu\rangle = 200$ . . . . .	111
8.2	Comparison of the key kinematic distributions for truth, truth-smearred and fully reconstructed $t\bar{t}$ samples . . . . .	115
8.3	Signal grid separation for HL-LHC projection . . . . .	117
8.4	Preselection-level distributions for HL-LHC projection . . . . .	119
8.5	BDT outputs for HL-LHC projection . . . . .	120
8.6	Limit plot for HL-LHC projection . . . . .	122
A.1	Electron performance parameterisations for HL-LHC detector simulation . . . . .	126
A.2	Muon performance parameterisations for HL-LHC detector simulation . . . . .	127
A.3	Jet performance parameterisations for HL-LHC detector simulation . . . . .	128
A.4	$E_T^{\text{miss}}$ performance parameterisations for HL-LHC detector simulation . . . . .	128
A.5	Expected sensitivity in each reoptimised signal region, and the best expected combination. . . . .	130
A.6	Diagram of DNN used in deep learning HL-LHC sensitivity estimate . . . . .	130
A.7	DNN outputs on benchmark SUSY signals. . . . .	131
A.8	$E_T^{\text{miss}}$ comparison of $W$ +jets nominal and extended sample. . . . .	133

# List of Tables

1.1	Summary table of the SM particles . . . . .	6
1.2	Chiral supermultiplets in the MSSM . . . . .	17
1.3	Gauge supermultiplets in the MSSM . . . . .	17
2.1	Summary of the Pixel Detector and SCT components . . . . .	28
3.1	Summary of $E_T^{\text{miss}}$ triggers used in Run-2 relevant for this thesis . . . . .	35
3.2	Table showing the MC estimates for the SM backgrounds in CRST . . . . .	42
3.3	Table of proposed single top CR selections . . . . .	43
3.4	Yields and purity in proposed single top CR . . . . .	44
3.5	Comparison of $Wt$ DR and DS predictions with dedicated $WWbb$ predictions	45
4.1	Summary of object definitions used in subsequent Chapters . . . . .	60
6.1	Summary of SUSY simplified model assumptions . . . . .	80
6.2	Preliminary event selection for $\tilde{\chi}_1^\pm \tilde{\chi}_2^0$ pair-production search . . . . .	82
6.3	Signal region definitions for $\tilde{\chi}_1^\pm \tilde{\chi}_2^0$ pair-production search . . . . .	82
6.4	Control region definitions . . . . .	82
6.5	Validation region definitions . . . . .	83
6.6	Summary of dominant experimental and modelling systematics . . . . .	83
6.7	Background-only fit results in the CRs . . . . .	84
6.8	Background-only fit results in the SRs . . . . .	85
6.9	Background normalisation factors . . . . .	85
6.10	From left to right, the observed 95% CL upper limits on the visible cross-sections $\sigma_{\text{vis}}$ , the observed ( $S_{\text{obs}}^{95}$ ) and expected ( $S_{\text{exp}}^{95}$ ) 95% CL upper limits on the number of signal events with $\pm 1\sigma$ excursions of the expectation, and the discovery $p$ -value ( $p_0$ ), truncated at 0.5. . . . .	89
7.1	Summary of 2HDM+ $a$ model parameters and choices . . . . .	93
7.2	Preliminary selections . . . . .	94
7.3	Signal region definitions . . . . .	95
7.4	Control region definitions . . . . .	95

---

7.5	Validation region definitions . . . . .	97
7.6	Summary of dominant experimental and modelling systematics . . . . .	97
7.7	Background-only fit results in the control regions . . . . .	98
7.8	Background-only fit results in the validation regions . . . . .	99
7.9	Background-only fit results in the signal region . . . . .	100
7.10	Background normalisation factors . . . . .	100
7.11	Expected and observed yields in inclusive discovery regions . . . . .	107
7.12	Model-independent limits from inclusive SRs . . . . .	108
8.1	Summary of ME and PS configurations used to generate SM MC samples. .	112
8.2	Summary of object definitions for leptons for HL-LHC projection . . . . .	115
8.3	Summary of object definitions for jets for HL-LHC projection . . . . .	116
8.4	Summary of preselection for HL-LHC projection . . . . .	116
8.5	Optimised BDT output cuts for the three SRs. . . . .	119
8.6	Extrapolated systematic uncertainties for HL-LHC projection. . . . .	121
8.7	Expected yields in all SRs after BDT cuts. . . . .	122
A.1	Reoptimised signal region selections for HL-LHC sensitivity study. . . . .	129

# 1 Introduction

2 Since its inception the Standard Model (SM) of particle physics has withstood huge  
3 amounts of experimental scrutiny. The SM provides a mathematical framework in which  
4 to describe *all* non-gravitational interactions of the known fundamental particles. With  
5 the discovery of the Higgs boson, a cornerstone of the SM, by the ATLAS and CMS col-  
6 laborations in 2012 [1, 2], the SM is considered complete.

7

8 While one cannot detract from the success of the SM's description of physics at the smallest  
9 scales, there are numerous open questions which have not yet been answered. The reconcil-  
10 iation of gravity with physics at the subatomic scale, the hierarchy problem, astrophysical  
11 evidence of dark matter, and the matter-antimatter asymmetry require explanations from  
12 physics Beyond the Standard Model (BSM). The experiments at the Large Hadron Col-  
13 lider (LHC) have a broad programme of direct and indirect searches for BSM physics.  
14 Aiding in this is the LHC itself, providing  $pp$  collisions at  $\sqrt{s} = 13$  TeV at luminosities  
15 around  $10^{34}\text{cm}^2\text{s}^{-1}$ . The huge datasets collected by both ATLAS and CMS, afforded  
16 by the LHC and its excellent performance, provide an ideal environment for BSM searches.

17

18 The physics analyses presented in this Thesis target two BSM scenarios; searches for  
19 Supersymmetry (SUSY) and searches for Dark Matter (DM) production. In both sce-  
20 narios, the SM Higgs sector is extended to include an additional Higgs doublet, hence  
21 these models being known as Two Higgs Doublet models (2HDM). With the addition of  
22 a pseudoscalar mediator,  $a$ , DM can couple to the SM extended Higgs sector, leading to  
23 a rich array of final states. The associated production of DM with a single top quark, a  
24 previously experimentally-uncovered final state, is studied in the context of the 2HDM+ $a$   
25 model. In addition to DM coupling to the SM through 2HDM+ $a$  scenarios, SUSY pro-  
26 vides a natural DM candidate. By adding an additional symmetry to the SM, particles  
27 gain 'superpartners', particles which differ in spin by 1/2 from their SM counterpart. The  
28 superpartners to the SM gauge bosons and Higgs mix and form a rich particle spectrum  
29 containing charged and neutral states, known as charginos and neutralinos. The lightest  
30 supersymmetric particle (LSP), in this case the lightest neutralino, is a leading candidate  
31 for DM. A search for the production of a chargino-neutralino pair decaying to LSPs is  
32 performed, using the SM Higgs and W boson as a mediator.

33

34 Both BSM scenarios studied in this Thesis are experimentally-challenging, due to their  
35 low rates when compared to irreducible SM processes. Advanced signal selection tech-  
36 niques using machine learning (ML) are studied, enabling the efficient selection of signal  
37 while providing strong SM background rejection. The upcoming High-Luminosity upgrade  
38 of the LHC and ATLAS will provide the opportunity to probe many BSM scenarios to  
39 levels never before possible, with an expected dataset of  $3000 \text{ fb}^{-1}$  being collected by AT-  
40 LAS by the end of operations. To prepare for the HL-LHC phase of operation, ATLAS  
41 will undergo a major upgrade of many detector components. The ATLAS inner tracker  
42 (ITk) will provide high-precision tracking in conditions where there as many as 200 in-  
43 elastic proton-proton collisions per bunch-crossing. The efficiency of the pixel modules of  
44 the ITk are studied after being irradiated to the expected HL-LHC dose. Combining ML  
45 methods with the huge high luminosity ATLAS dataset, the sensitivity to SUSY at the  
46 High-Luminosity LHC (HL-LHC) is also studied.

47

48 **Part I** first gives a theoretical overview of the SM, motivates the need for BSM physics,  
49 and then gives an overview of SUSY and the 2HDM+ $a$  model of DM production. It also  
50 gives a brief description of the LHC along with an overview of the ATLAS detector. Fi-  
51 nally, the datasets used in this thesis are discussed, along with discussion of the simulation  
52 methods and object definitions used in the subsequent Chapters.

53

54 **Part II** presents three analyses using  $pp$  data at  $\sqrt{s} = 13 \text{ TeV}$ . Chapter 6 presents a  
55 search for electroweak SUSY using  $36.1 \text{ fb}^{-1}$  data and subsequently  $139 \text{ fb}^{-1}$ . Chapter 7  
56 presents a search for DM production in association with a single top quark using  $139 \text{ fb}^{-1}$   
57 data.

58

59 **Part III** presents studies done in the context of the HL-LHC. Chapter 8 presents a  
60 prospects study done for an electroweak SUSY search using  $3000 \text{ fb}^{-1}$  at  $\sqrt{s} = 14 \text{ TeV}$ .  
61 Chapter B presents studies done on the performance of hybrid pixel modules for ATLAS'  
62 Inner Tracker (ITk) upgrade for the HL-LHC.

63

## Part I

64

# Theoretical overview and experimental apparatus

65

# Chapter 1

## The Standard Model and Beyond

This chapter presents an overview of the Standard Model (SM), along with the extensions to it which form the basis of the analyses in Chapters 6 and 7. The SM is currently our best description of nature but does not give a complete description of some fundamental physical phenomena, outlined in Section 1.2, which motivates searches for physics beyond the SM (BSM).

### 1.1 The Standard Model

The SM is the name given to the theory describing the fundamentals of particle interactions. Since its inception over half a century ago, it has withstood experimental scrutiny, each time providing a theoretical description of experimental data. The particle content of the SM was deemed complete in 2012, with the discovery of a particle consistent with the Higgs boson by the ATLAS [1] and CMS [2] collaborations.

As alluded to at the beginning of this chapter, the SM describes an incomplete description of nature, covering three of the four fundamental forces; electromagnetic, strong and weak interactions. Gravity, at the particle level, is, however, orders of magnitude weaker than the other three, and hence its effect would be too small to detect.

#### Overview

The SM particles are easily separable into two categories; fermions, which obey Fermi-Dirac statistics and have half-integer spin, and bosons, which obey Bose-Einstein statistics and have integer spin.

The fermions are further separable into two families, quarks and leptons, both of which have three generations. The quarks can be separated into ‘up-type’ and ‘down-type’, having electric charge  $+\frac{2}{3}$  and  $-\frac{1}{3}$ , respectively. The ‘up-type’ quarks are the up (u), charm (c)

92 and top (t) quarks, while the ‘down-type’ quarks are the down (d), strange (s) and bottom  
93 (b). The leptons can be separated into charged leptons and neutral leptons (known as  
94 neutrinos), with the charged leptons having an electric charge of  $-1$ . The charged leptons  
95 are the electron (e), the muon ( $\mu$ ) and the tau ( $\tau$ ), with a corresponding electron neutrino  
96 ( $\nu_e$ ), muon neutrino ( $\nu_\mu$ ) and tau neutrino ( $\nu_\tau$ ).

97

98 Composite particles can be formed from combinations of quarks. ‘Hadrons’ are defined  
99 as bound states of quarks, with mesons being formed from pairs of quarks and baryons  
100 being formed by three quarks. In recent years, more exotic bound states of quarks, such  
101 as tetra- and penta-quarks have been observed by the LHCb collaboration. **REF** The first  
102 generation quarks, i.e. the up quark and down quark, can be combined to produce pro-  
103 tons (uud) and neutrons (udd). Combining protons and neutrons with the first generation  
104 charged lepton, the electron, we give rise to nuclear physics and all physical matter in our  
105 universe.

106

107 The SM bosons are responsible for the interactions of the SM particles. Electromagnetic  
108 interactions are mediated by the photon ( $\gamma$ ), and only occur between electrically-charged  
109 particles. Gluons (g), massless and electrically-neutral bosons, mediate interaction between  
110 quarks, which carry the colour charge (discussed in section 1.1). The  $W^\pm$  and  $Z^0$  bosons  
111 mediate the weak interaction, which all SM particles are subject to.

112

113 The particle content of the SM is summarised in Table 1.1.

## 114 **Mathematical formulation of the SM**

115 The SM is a quantum field theory (QFT) based upon the product of symmetry groups:

$$\text{SU}(3)_C \times \text{SU}(2)_L \times \text{U}(1)_Y \tag{1.1.1}$$

116 The  $\text{SU}(3)_C$  component describes strong interactions (QCD), the  $\text{SU}(2)_L$  component  
117 describes the electroweak sector and  $\text{U}(1)_Y$  describes electromagnetic interactions.

118

119 In order to understand the mathematical formulation of the SM, the concepts of *groups* will  
120 be briefly discussed. A group is a set of mathematical objects,  $G$ , along with an operation,  
121 which obey the following ‘axioms’ [4]:

122

- *Closure*: For all  $a, b \in G$ ,  $a \cdot b \in G$

123

- *Associativity*: For all  $a, b$  and  $c \in G$ ,  $(a \cdot b) \cdot c = a \cdot (b \cdot c)$

124

- *Identity element*: An identity element,  $I$ , exists such that  $I \cdot a = a \cdot I = a$

125

- *Inverse element*: An inverse element of  $a$ ,  $a^{-1}$ , exists such that  $a \cdot a^{-1} = a^{-1} \cdot a = I$

Name	Symbol	Charge ( $e$ )	Spin	Mass
Fermions - Generation-I				
Up-quark	$u$	+2/3	1/2	2.16 MeV
Down-quark	$d$	-1/3	1/2	4.67 MeV
Electron	$e$	-1	1/2	0.511 MeV
Electron-neutrino	$\nu_e$	0	1/2	< 2 eV
Fermions - Generation-II				
Charm-quark	$c$	+2/3	1/2	1.27 GeV
Strange-quark	$s$	-1/3	1/2	93 MeV
Muon	$\mu$	-1	1/2	105.66 MeV
Muon-neutrino	$\nu_\mu$	0	1/2	< 2 eV
Fermions - Generation-III				
Top-quark	$t$	+2/3	1/2	172.9 GeV
Bottom-quark	$b$	-1/3	1/2	4.18 GeV
Tau	$\tau$	-1	1/2	1.78 GeV
Tau-neutrino	$\nu_\tau$	0	1/2	< 2 eV
Bosons				
$W$ boson	$W^\pm$	$\pm 1$	1	80.4 GeV
$Z$ boson	$Z$	0	1	91.2 GeV
Gluon	$g$	0	1	0
Photon	$\gamma$	0	1	0
Higgs boson	$H$	0	0	125.1 GeV

Table 1.1: A table describing the charge, mass and spin of the SM particles. Particle masses taken from [3].

126 The commutation relations of the members of a group are important to know. As a  
 127 reminder, the comutator of two elements of a group,  $a, b$  is defined as:

$$[a, b] = (a \cdot b - b \cdot a) \tag{1.1.2}$$

128 Groups where the commutator of any two elements is always 0 are known as ‘abelian’,  
 129 while groups where this does not hold are called ‘non-abelian’. Abelian groups have  $n^2$   
 130 generators of the underlying Lie algebra, while non-abelian groups have  $n^2 - 1$  generators.  
 131 While this seems conceptually-abstract, the number of generators of a group physically  
 132 corresponds to the number of ‘force-carriers’ present in a theory govered by that group.

133

134 In equation 1.1.1,  $U(n)$  and  $SU(n)$  refer to unitary groups and special unitary groups,  
 135 respectively.  $U(n)$  is the set of  $n \times n$  unitary matrices ( $U \cdot U^{-1} = I$ ), and  $SU(n)$  the subset

136 of  $U(n)$  which have a determinant of 1. The individual symmetry groups will be discussed  
 137 in more details in the following sections, starting with electromagnetic interactions and the  
 138  $U(1)$  group.

### 139 Quantum Electrodynamics

140 Electromagnetic interactions are described by Quantum Electrodynamics (QED). These  
 141 interactions are unique in the SM, as they have infinite range. We will derive the Lagrangian  
 142 describing QED, starting from the Dirac equation for free fermions:

$$\mathcal{L}_{\text{Dirac}} = \bar{\psi}(i\gamma^\mu\partial_\mu - m)\psi \quad (1.1.3)$$

143 Due to the  $U(1)$  symmetry, QED is symmetric under *global* phase transformations of the  
 144 form:

$$\psi(x) \rightarrow \psi'(x) = e^{i\alpha}\psi(x), \quad \bar{\psi}(x) \rightarrow \bar{\psi}'(x) = e^{-i\alpha}\bar{\psi}(x) \quad (1.1.4)$$

145 Under *local* transformations, where  $\alpha \rightarrow \alpha(x)$ , the Lagrangian in Equation 1.1.3 is not  
 146 gauge invariant:

$$i\bar{\psi}'\gamma^\mu\partial_\mu\psi' = i\bar{\psi}\gamma^\mu\partial_\mu\psi - \bar{\psi}\gamma^\mu\partial_\mu\alpha\psi \quad (1.1.5)$$

147 To resolve this, we define the covariant derivative:

$$D_\mu \equiv \partial_\mu + ieA_\mu \quad (1.1.6)$$

148 Note, with the introduction of the covariant derivative comes the introduction of the vector  
 149 field,  $A_\mu$ , which transforms as:

$$A_\mu \rightarrow A'_\mu = A_\mu - \frac{1}{e}\partial_\mu\alpha(x) \quad (1.1.7)$$

150 The result of a local transformation on the Dirac equation is now:

$$i\bar{\psi}'\gamma^\mu D'_\mu\psi' - m\bar{\psi}\psi = i\bar{\psi}\gamma^\mu\partial_\mu\psi - \bar{\psi}\gamma^\mu eA_\mu\psi - m\bar{\psi}\psi \quad (1.1.8)$$

151 Rearranging Equation 1.1.6 for  $\partial_\mu$  and substituting in, we see local gauge invariance holds  
 152 thanks to the introduction of the covariant derivative. Of particular interest is the term  
 153  $\bar{\psi}\gamma^\mu eA_\mu\psi$ , which couples the fermion fields to the vector field, which we associate to the  
 154 photon,  $\gamma$ , with the coupling constant  $e$  corresponding to the electrical charge of the  
 155 fermion. To complete the QED Lagrangian, one must add the electromagnetic Lagrangian  
 156 to the Dirac Lagrangian. (For concision, we now adopt the Feynman ‘slash’ notation:  
 157  $\not{\partial} = \gamma^\mu\partial_\mu$ ).

$$\mathcal{L}_{\text{QED}} = \mathcal{L}_{\text{Dirac}} + \mathcal{L}_{\text{EM}} = \bar{\psi}(i\not{\partial} - m)\psi - \frac{1}{4}F^{\mu\nu}F_{\mu\nu} \quad (1.1.9)$$

158 As the interaction term, introduced by using the covariant derivative, couples fermions to  
 159 the photon with a coupling  $e$ , QED interactions are only relevant for electrically-charged  
 160 fermions. Figure 1.1 shows the QED interaction vertex.

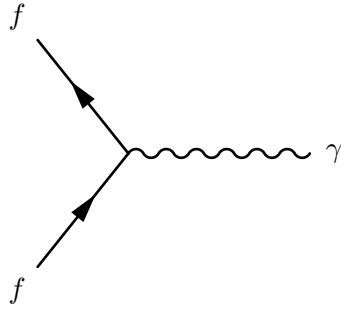


Figure 1.1: Feynman diagram showing the QED interaction vertex between a fermion and the photon.

## 161 Quantum Chromodynamics

162 Quantum Chromodynamics addresses the interactions between quarks and gluons. It is  
 163 governed by the  $SU(3)_C$  symmetry hence having  $N_C^2 - 1 = 8$  mediators. By virtue of  
 164 the symmetry group being a *special* unitary group, the theory is non-abelian, resulting in  
 165 gluons being able to self-interact. Similarly to QED, we begin from the Dirac Lagrangian  
 166 and introduce a covariant derivative, in this case defined as:

$$\partial^\mu = D^\mu \equiv \partial^\mu \delta_{ij} - ig_s t_{ij}^a G^{a\mu} \quad (1.1.10)$$

167 where  $\delta_{ij}$  is the Kroenecker delta (0 for  $i \neq j$ , 1 for  $i = j$ ),  $g_s$  the strong coupling  
 168 constant,  $t^a = \frac{\lambda^a}{2}$  the generators of the  $SU(3)_C$  symmetry group with  $\lambda^a$  being the Gell-  
 169 Mann matrices and  $G^a$  being the gluon gauge fields. Rewriting the Dirac equation from  
 170 Equation 1.1.3:

$$\mathcal{L}_{\text{QCD}} = \bar{\psi}_j (i\gamma_\mu \partial^\mu - m\delta_{ij}) \psi_i \quad (1.1.11)$$

171 In Equation 1.1.11,  $i$  and  $j$  index the quarks from 1 to 3 and  $a$  indexes the gluons  
 172 from 1 to 8. Replacing the regular partial derivate in Equation 1.1.10 with the covariant  
 173 derivative from Equation 1.1.11, we obtain:

$$\mathcal{L}_{\text{QCD}} = \bar{\psi}_j (i\gamma_\mu \partial^\mu \delta_{ij} - m\delta_{ij}) \psi_i - g_s (\bar{\psi}_j \gamma_\mu t_{ij}^a \psi_i) G^{a\mu} \quad (1.1.12)$$

174 Adding in the kinetic term for the gluon fields and again using the Feynman slash  
 175 notation, the full QCD Lagrangian is:

$$\mathcal{L}_{\text{QCD}} = \bar{\psi} (i\not{D} - m)\psi - \frac{1}{4} G_a^{\mu\nu} G_{\mu\nu}^a \quad (1.1.13)$$

176 Equation 1.1.13 is helpful to understand the gluon self-interaction, with 3-gluon and  
 177 4-gluon interactions present in the expansion of the  $G_{\mu\nu}^a G_a^{\mu\nu}$ .

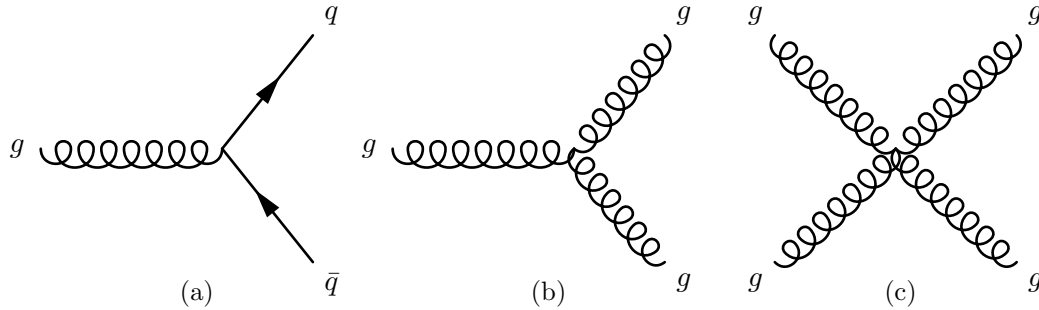


Figure 1.2: Feynman diagram showing the QCD quark-gluon interaction vertex (a), the triple gluon self-interaction (b) and the quartic gluon self-interaction (c).

178 Despite begin similar in mathematical structure to QED, QCD has two distinct features;  
 179 *asymptotic freedom* and *colour confinement*. The strong coupling constant,  $\alpha_s \equiv g_s^2/4\pi$ ,  
 180 is in fact not a constant but varies with the separation of the involved particles. This  
 181 is known as a *running coupling*. At large distances, or equivalently at low energies,  $\alpha_s$   
 182 asymptotically diverges meaning the coupling *grows stronger*. However, at low separation  
 183 or high energies, the strong interaction is very weak and the partons essentially never in-  
 184 teract, known as *asymptotic freedom*. This enables the use of perturbative calculations to  
 185 make accurate QCD predictions.

186  
 187 Colour confinement forbids the existence of a quark in isolation, instead forcing quarks  
 188 to exist in colourless, bound states, known as hadrons. Due to the running coupling, when  
 189 the separation of a quark-antiquark pair is increased, so does the energy of the strong in-  
 190 teraction between them. With increasing separation, it eventually becomes energetically-  
 191 favourable to produce another quark-antiquark pair. This quark-antiquark pair forms  
 192 colourless, bound states with the initial quark-antiquark pair. Top quarks are not colour  
 193 confined, as their decay time of around  $5 \times 10^{-25}$ s, is too short for hadronisation to occur.  
 194 An additional result of colour confinement is that the range of the strong force is extremely  
 195 short, around 1fm.

## 196 Weak interaction and Electroweak unification

197 The  $SU(2)_L$  group is responsible for the weak interaction. It is therefore expected that the  
 198 weak interaction has 3 mediators (from  $N^2 - 1$ );  $W_\mu^1$ ,  $W_\mu^2$  and  $W_\mu^3$ . The weak interaction  
 199 also introduces new quantum numbers known as weak isospin,  $T$ , as well as its third  
 200 component  $T^3$ . With these quantum numbers, we can define weak isospin doublets, using

201 the first generation leptons and quarks as examples:

$$\begin{pmatrix} \nu_L \\ e_L \end{pmatrix}; \begin{pmatrix} u_L \\ d_L \end{pmatrix} \quad (1.1.14)$$

202 Both of these weak isospin doublets have  $T = \frac{1}{2}$ , with the fermion in the ‘upper’ posi-  
203 tion having  $T^3 = +\frac{1}{2}$  and the fermion in the ‘lower’ position having  $T^3 = -\frac{1}{2}$ .

204

205 An extremely important concept for understanding the weak interaction is chirality. Chi-  
206 rality is an intrinsic property of particles, and determines how they behave in the weak  
207 interaction. The subscript ‘L’ is present as only fermions with ‘left-handed’ chirality (anti-  
208 fermions with ‘right-handed’ chirality) interact via the weak interaction. ‘Left-handed’  
209 fermions, and ‘right-handed’ anti-fermions have  $T = \frac{1}{2}$  and hence form isospin doublets,  
210 whereas ‘right-handed’ fermions and ‘left-handed’ anti-fermions have  $T = 0$  are hence are  
211 isospin singlets.

212

213 The introduction of weak isospin doublets enables a mechanism for quarks to change flavour  
214 through a charged-current interaction. For example, a ‘down-type’ quark can change into  
215 an ‘up-type’ quark through a transition of  $T^3$ . The Cabibbo-Kobayashi-Maskawa matrix,  
216 known as the CKM matrix, determines the probability of a quark,  $q$ , to transition to  
217 another flavour.

$$\begin{pmatrix} d' \\ s' \\ b' \end{pmatrix} = \begin{pmatrix} |V_{ud}| & |V_{us}| & |V_{ub}| \\ |V_{cd}| & |V_{cs}| & |V_{cb}| \\ |V_{td}| & |V_{ts}| & |V_{tb}| \end{pmatrix} \begin{pmatrix} d \\ s \\ b \end{pmatrix} \quad (1.1.15)$$

218 The CKM matrix is *almost* a diagonal matrix, with the on-diagonal elements being  
219 close to one, while the off-diagonal elements are small but non-zero. Therefore, the most  
220 probable quark flavour transitions are intra-generational, but inter-generation transitions  
221 are allowed.

222

223 It was shown by Glashow, Salam and Weinberg that the interaction can be unified with  
224 the electromagnetic interaction, with an overall symmetry group of  $SU(2)_L \times U(1)_Y$ . We  
225 now introduce the weak hypercharge,  $Y = 2(Q - T^3)$ , where  $Q$  is the electric charge. At  
226 low energies, the electromagnetic and weak interactions independently explain physical  
227 phenomena, such as hyperfine splitting and  $\beta$  decay in nuclei. The unification of these  
228 two interactions into the electroweak interaction must therefore preserve the two sepa-  
229 rate interactions at low energy. However, above the ‘unification energy’, the two separate  
230 interactions are merged into a one. This new, unified interactions has four mediators;  
231 two massive, charged  $W^\pm$  bosons, a massive, neutral  $Z$  and the massless, neutral  $\gamma$  from

232 the U(1) symmetry in QED. The interaction vertices of the three massive electroweak  
 233 gauge bosons are shown in Figure 1.3. Note, Figure 1.3b shows the interaction of only the  
 negatively-charged  $W$  boson interacting with leptons.

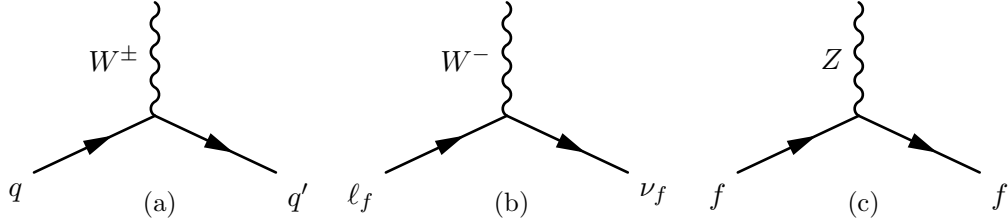


Figure 1.3: Feynman diagrams showing the massive electroweak gauge bosons interaction vertices. Note, as shown in (b), only the  $W^-$  couples to the lepton isospin doublet, whereas for the quark isospin doublets (a) both the  $W^\pm$  are involved.

234

235 The  $SU(2)_L \times U(1)_Y$  symmetry group is non-abelian, and thus the electroweak gauge  
 236 bosons can self-interact. Similarly to gluons in QCD, there are triple and quartic self-  
 237 couplings;  $W^\pm W^\mp Z/\gamma$ ,  $W^\pm W^\mp Z/\gamma Z\gamma$  and  $WWWW$ .

238 As discussed previously, to ensure local gauge invariance of the SM electroweak La-  
 239 grangian, we define the covariant derivative:

$$\partial_\mu \rightarrow D_\mu \equiv \partial_\mu + \frac{i}{2} g \vec{\tau} \cdot \vec{W}_\mu + i g' \frac{Y}{2} B_\mu \quad (1.1.16)$$

240 where  $\vec{W}_\mu$  and  $B_\mu$  are the gauge fields, and  $g$  and  $g'$  are the couplings, of the  $SU(2)_L$   
 241 and  $U(1)_Y$  symmetries, respectively. As the electroweak interaction only couples to ‘left-  
 242 handed’ fermions, we can define projection operators, which project out the left- and  
 243 right-handed components of a field:

$$P_L = \frac{1}{2}(1 - \gamma^5); P_R = \frac{1}{2}(1 + \gamma^5); \gamma^5 \equiv \begin{pmatrix} 0 & I_2 \\ I_2 & 0 \end{pmatrix} \quad (1.1.17)$$

244 We are then able to write the fermion field as  $\psi = P_L \psi + P_R \psi = \psi_L + \psi_R$ . The mass  
 245 term in the Lagrangian,  $m\bar{\psi}\psi$ , now expands as:

$$m\bar{\psi}\psi = m\bar{\psi}_R\psi_L + m\bar{\psi}_L\psi_R \quad (1.1.18)$$

246 The left- and right-handed components of the fermion field,  $\psi$ , transform differently  
 247 under the  $SU(2)_L \times U(1)_Y$  symmetry and therefore the mass term in Equation 1.1.18 breaks  
 248 local gauge symmetry. Therefore, we need to introduce a mechanism by which fermions,  
 249 and also the electroweak gauge bosons, become massive.

250 **The Higgs sector**

251 The Higgs mechanism, first proposed in 19XX, resolves the tensions between electroweak  
 252 unification and massive fermions by introducing an  $SU(2)_L$  doublet of complex, scalar  
 253 fields:

$$\Phi = \begin{pmatrix} \phi^+ \\ \phi^0 \end{pmatrix} = \frac{1}{\sqrt{2}} \begin{pmatrix} \phi_1 + i\phi_2 \\ \phi_3 + i\phi_4 \end{pmatrix} \quad (1.1.19)$$

254 This doublet has isospin  $T = \frac{1}{2}$  and hypercharge  $Y = 1$ . This field has a scalar potential  
 255 defined as:

$$V(\Phi) = \mu^2 \Phi^\dagger \Phi + \lambda (\Phi^\dagger \Phi)^2 \quad (1.1.20)$$

256 The two terms in Equation 1.1.20 can be identified as a mass term for the scalar boson  
 257 and a self-interaction term, respectively. Dependent upon the choices for  $\mu^2$  ( $\lambda > 0$ ), the  
 258 potential can take on two shapes; parabolic for  $\mu^2 > 0$  and a ‘wine bottle’ potential for  
 259  $\mu^2 < 0$ . For reasons discussed later, the Higgs potential has  $\mu^2 < 0$ , and the shape of this  
 260 potential is shown in Figure 1.4.

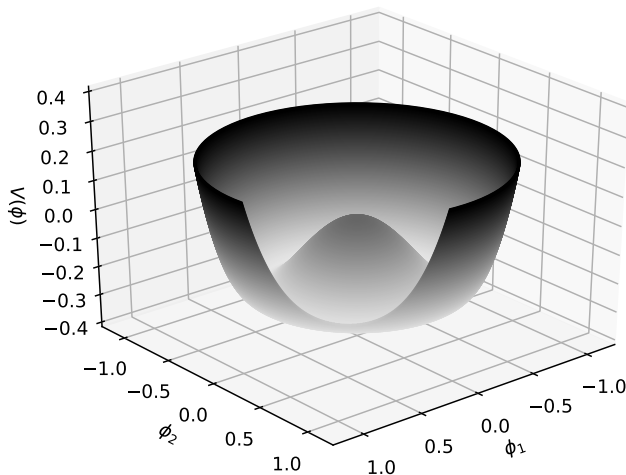


Figure 1.4: Schematic diagram showing the shape of the Higgs potential, known as the ‘Mexican hat’ potential.

261 The potential shown in Figure 1.4 evidently has a local minima at  $\phi_1, \phi_2 = 0$ . However,

262 the global minima is at non-zero values of  $\phi$ , and is given by:

$$\phi_{min} = \sqrt{-\frac{\mu^2}{2\lambda}} \quad (1.1.21)$$

263 We define  $v^2 = \mu^2/\lambda$ , where  $v$  is the vacuum expectation value (vev) of the the Higgs field.  
 264 The vev of the Higgs field is therefore, non-zero, and is experimentally determined to be  
 265  $\approx 246$  GeV. It is convenient to choose the vevs of the  $\phi_1$ ,  $\phi_2$  and  $\phi_4$  to zero, while for  $\phi_3$   
 266 the vev is:

$$\langle 0|\phi_3|0\rangle^2 = v^2 = \frac{\mu^2}{\lambda} \quad (1.1.22)$$

267 The choice for the spontaneous symmetry breaking to be done with the field  $\phi_3$  is to  
 268 allow the photon to remain massless. Expanding the Higgs field around the minima with  
 269  $\phi_3 = h + v$ , we eventually acquire a term for the Higgs mass of  $m_H = \sqrt{-2\mu^2}$ . Inserting  
 270 this field into 1.1.16, we obtain the mass terms for the electroweak gauge bosons:

$$\begin{aligned} m_W &= \frac{1}{2}gv \\ m_Z &= \frac{1}{2}\sqrt{g^2 + g'^2} v \\ m_\gamma &= 0 \end{aligned} \quad (1.1.23)$$

271 The Higgs Lagrangian contains couplings to not only the electroweak gauge bosons but  
 272 also the SM fermions. The strength of the couplings to the fermions are given by  $y_f$ ,  
 273 known as *Yukawa couplings*. This coupling enables the fermions to acquire masses in a  
 274 gauge-invariant way through the Higgs mechanism. The mass of a fermion,  $f$ , is given by:  
 275

$$m_f = y_f \frac{v}{\sqrt{2}} . \quad (1.1.24)$$

276 Fermion masses are experimentally-determined, hence determining the Yukawa coupling of  
 277 the Higgs to that fermion. The interactions of the Higgs with the electroweak gauge bosons  
 278 and SM fermions are shown in Figure 1.5. The Higgs decay branching ratios (BR) depends  
 279 both upon the Higgs mass and the Yukawa coupling of the Higgs to the SM particles.  
 280 Figure 1.6 shows the Higgs BRs for a SM Higgs boson with a mass in the range, 120-130  
 281 GeV. The largest Higgs BR is to a  $b\bar{b}$ -pair, which is important for the analyses detailed in  
 282 Chapters 6 and 8.

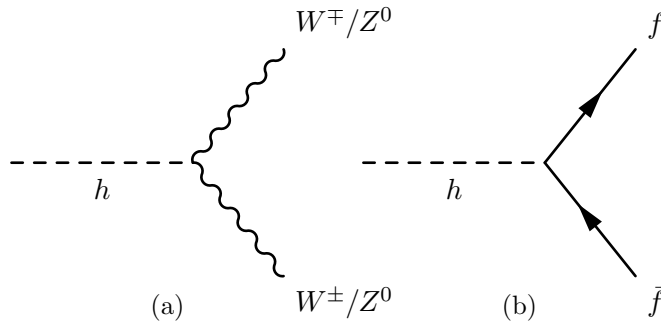


Figure 1.5: Feynman diagrams showing the Higgs interaction vertices with the electroweak gauge bosons (1.5a) and SM fermions (1.5b).

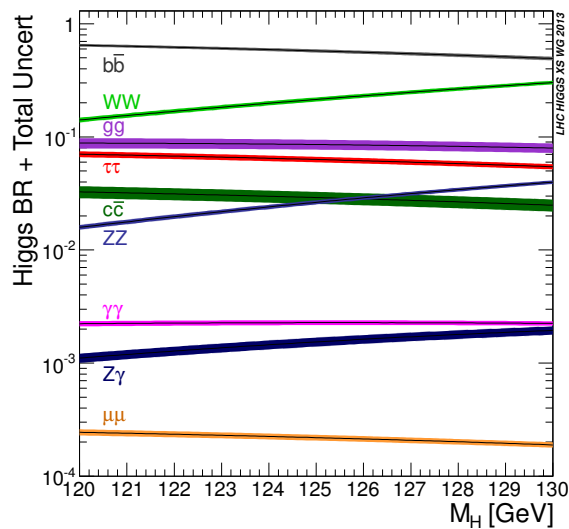


Figure 1.6: This plot shows the branching ratios of the SM Higgs decaying to SM particles in the mass range 120-130 GeV. **REF**

## 283 Open questions in the SM

284 The first of the open questions to be discussed is the hierarchy problem. While the SM does  
 285 not account for gravitational interactions, it is impossible to have a complete description  
 286 of nature, a so-called ‘Grand Unified Theory’ (GUT), without its inclusion. The hierarchy  
 287 problem arises when considering a unified theoretical description of all four, fundamental  
 288 forces. Gravity is expected to become the dominant interaction at the Planck scale, which  
 289 has an equivalent mass of  $O(10^{19})$  GeV. This is 17 orders of magnitude higher the elec-  
 290 troweak scale and the Higgs mass,  $O(10^2)$  GeV.

291

292 The Higgs mass consists of two terms; a ‘bare’ mass and the sum of the virtual corrections  
 293 from particles coupling to the Higgs. We treat the Planck scale,  $\Lambda_P$ , as a cut-off value for

294 the virtual contributions. Therefore, the physical Higgs mass can be written as:

$$m_H^2 = m_{H,\text{bare}}^2 + \delta m_H^2 = m_{H,\text{bare}}^2 - \frac{|g_f|^2}{8\pi^2} \Lambda_p^2 + \dots \quad (1.1.25)$$

295 Here, the neglected terms grows logarithmically in  $\Lambda_p$ . Assuming the SM is indeed valid  
 296 upto the Planck scale, then the second term is  $O(10^{19}\text{GeV})^2$ , requiring an equally-large  
 297 (to 1 part in over  $10^{30}$  orders of magnitude) bare Higgs mass. The Anthropic Principle  
 298 is sometimes invoked to justify this ‘fine-tuning’ [5], while extensions to the SM such as  
 299 Supersymmetry (SUSY) provide elegant, mathematical solutions to the hierarchy problem.

300

301 Next we discuss DM. Observations of anomalous gravitational behaviour, such as in the  
 302 rotational curves of galaxies, enable us to infer the existence of DM. Since we do not *visibly*  
 303 observe DM, it is inferred that DM does not interact electromagnetically, therefore being  
 304 electrically-neutral. We also require DM to be stable, as its effects are observed from the  
 305 early universe, in the CMB, until now.

306

307 Recent measurements of the DM abundance estimate that  $\Omega_{DM}h^2 = 0.1196 \pm 0.0031$ ,  
 308 meaning that DM makes up as much as 26% of the universe. The only DM candidate  
 309 within the SM are neutrinos as they are massive (inferred from neutrino mixing), neutral  
 310 and stable. Therefore, neutrinos actually form part of the DM density. However, their  
 311 contribution can be estimated as  $\Omega_\nu h^2 \approx \frac{\sum_i m_i}{91\text{eV}} < 0.003$ , a minor contribution to the total  
 312 DM abundance.

## 313 1.2 Physics Beyond the Standard Model

314 There are countless proposed extensions to the SM, each which can provide solutions to  
 315 some of the open questions. One such method is to postulate a DM candidate, and couple  
 316 it to the SM through some mediator. Section ?? describes one such model. Another way  
 317 of generating New Physics is to extend the symmetries of the SM. One such extension is  
 318 supersymmetry (SUSY), which is described in Section ??.

### 319 Supersymmetry

320 SUSY introduces an additional symmetry to the SM in which SM fermions can become  
 321 bosons and SM bosons can become fermions. An operator,  $Q$ , is introduced which enables  
 322 transformations between bosonic and fermionic states, as follows:

$$\begin{aligned} Q|\text{boson}\rangle &= |\text{fermion}\rangle \\ Q|\text{fermion}\rangle &= |\text{boson}\rangle . \end{aligned} \quad (1.2.1)$$

323 The symmetry group of SUSY is of the form  $SU(3)_C \times SU(2)_L \times U(1)_Y \times \text{SUSY}$  such that  
 324 when a SM particle undergoes a SUSY transformation, the SM quantum numbers are un-  
 325 changed. Under this symmetry group, each of the SM particles gains a superpartner with  
 326 spin differing by  $1/2$ . The SM particles and their superpartners can be placed into either  
 327 chiral multiplets or gauge multiplets.

328

329 The SM fermions and their bosonic, spin-0 superpartners form chiral multiplets. The  
 330 superpartners to the SM fermions have an ‘s’ prepended to their name, short for scalar.  
 331 For example, the superpartner to the SM top quark is named the ‘stop’ quark. The SM  
 332 bosons have ‘ino’ appended to their name, an example of this being the superpartners to  
 333 the SM gluon being named gluinos. The SM vector bosons and their superpartners form  
 334 gauge multiplets. In order to give masses to all of the particles, SUSY requires two Higgs  
 335 doublets with weak isospin  $Y = \pm 1/2$ . This extended Higgs sector gives rise to four gauge  
 336 eigenstates to the Higgs scalars:  $\tilde{H}_u^+$ ,  $\tilde{H}_u^0$ ,  $\tilde{H}_d^0$  and  $\tilde{H}_d^-$ . These four eigenstates mix to  
 337 form five mass eigenstates:  $h^0$ ,  $H^0$ ,  $A^0$  and  $H^\pm$ . The SM Higgs boson discovered in 2012  
 338 is identified as the lightest CP-even SUSY Higgs,  $h^0$ , while the remaining mass eigenstates  
 339 are much higher masses and are decoupled. A summary of the chiral supermultiplets and  
 340 gauge supermultiplets are shown in Tables 1.2 and 1.3, respectively.

341

342 The Coleman-Mandula theorem **REF** requires that the operators  $Q$  and  $Q^\dagger$  have the  
 343 following (anti-)commutation rules:

$$\begin{aligned} Q_\alpha, Q_\beta^\dagger &= -2\sigma_{\alpha\beta}^\mu P_\mu \\ Q_\alpha, Q_\beta &= Q_\alpha^\dagger, Q_\beta^\dagger = 0 \\ [P^\mu, Q] &= [P^\mu, Q^\dagger] = 0 \end{aligned} \tag{1.2.2}$$

344 Here,  $\sigma_{\alpha\beta}^\mu$  are the Pauli matrices and  $P_\mu$  is the

$$\delta m_{H,S}^2 = \frac{\lambda_s}{16\pi^2} \Lambda_P^2 - 2m_s^2 \ln \left( \frac{\Lambda_P}{m_s} \right) \tag{1.2.3}$$

### 345 Unification of fundamental interactions

346 As previously discussed, it was shown by Glashow, Salam and Weinberg that the electro-  
 347 magnetic and weak interactions unify above the electroweak scale, resulting in the combined  
 348 electroweak interaction. It is postulated that above some grand unified theory (GUT) scale,  
 349 the electromagnetic, weak and strong forces unify. However, in the SM, the evolution of  
 350 the couplings of the three forces never converge. However, as described, SUSY introduces  
 351 additional particles which alter the running of the coupling constants, allowing them to  
 352 unify at the GUT scale. The running of the couplings are shown in Figure 1.7 for both the

Names	Symbol	Spin-0	Spin-1/2	$SU(3)_C \times SU(2)_L \times U(1)_Y$
squarks, quarks (3 generations)	$Q$	$(\tilde{u}_L \tilde{d}_L)$	$(u_L d_L)$	$(\mathbf{3}, \mathbf{2}, \frac{1}{6})$
	$\bar{u}$	$\tilde{u}_R^*$	$u_R^\dagger$	$(\bar{\mathbf{3}}, \mathbf{1}, -\frac{2}{3})$
	$\bar{d}$	$\tilde{d}_R^*$	$d_R^\dagger$	$(\bar{\mathbf{3}}, \mathbf{1}, \frac{1}{3})$
sleptons, leptons (3 generations)	$L$	$(\tilde{\nu} \tilde{e}_L)$	$(\nu e_L)$	$(\mathbf{1}, \mathbf{2}, -\frac{1}{2})$
	$\bar{e}$	$\tilde{e}_R^*$	$e_R^\dagger$	$(\mathbf{1}, \mathbf{1}, 1)$
Higgs, higgsinos	$H_u$	$(H_u^+ H_u^0)$	$(\tilde{H}_u^+ \tilde{H}_u^0)$	$(\mathbf{1}, \mathbf{2}, +\frac{1}{2})$
	$H_d$	$(H_d^0 H_d^-)$	$(\tilde{H}_d^0 \tilde{H}_d^-)$	$(\mathbf{1}, \mathbf{2}, -\frac{1}{2})$

Table 1.2: Chiral supermultiplets in the MSSM.

Names	Spin-1/2	Spin-1	$SU(3)_C \times SU(2)_L \times U(1)_Y$
gluino, gluon	$\tilde{g}$	$g$	$(\mathbf{8}, \mathbf{1}, 0)$
winos, $W$ bosons	$\tilde{W}^\pm \tilde{W}^0$	$W^\pm W^0$	$(\mathbf{1}, \mathbf{3}, 0)$
bino, $B$ boson	$\tilde{B}^0$	$B^0$	$(\mathbf{1}, \mathbf{1}, 0)$

Table 1.3: Gauge supermultiplets in the MSSM.

SM and SUSY.

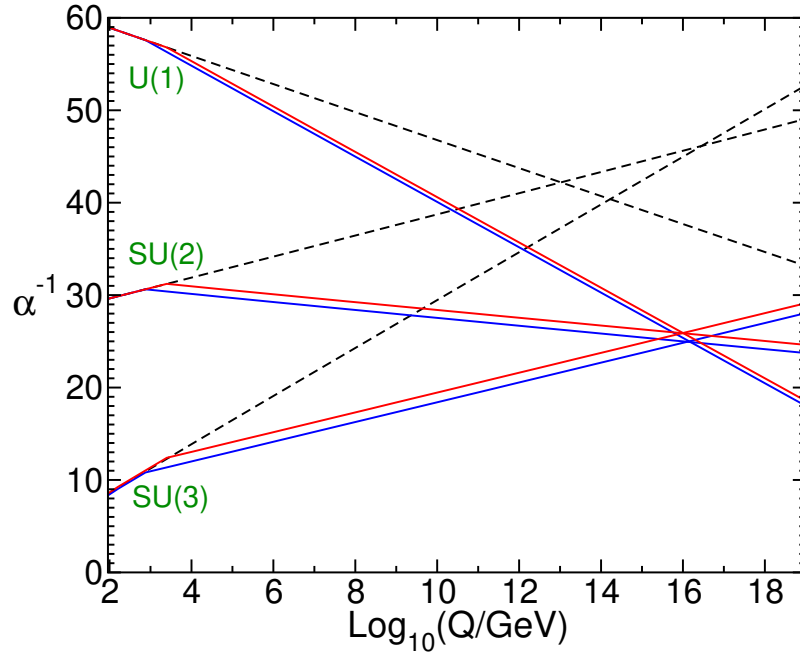


Figure 1.7: Diagram showing how the coupling constants evolve in SM-only (dashed) and SUSY (solid) scenarios. For the SUSY particles, the masses are varied from 750 GeV to 2.5 TeV.

### 354 Resolution to the hierarchy problem

355 As previously discussed, the squared-mass of the Higgs boson,  $m_H^2$ , is comprised of two  
 356 components; a bare mass,  $m_{H,\text{bare}}^2$ , and the quantum corrections to the Higgs mass through  
 357 fermion couplings,  $\delta m_H^2$ . The correction to the Higgs mass for a given fermion,  $f$ , is given  
 358 by

$$\delta m_{H,f}^2 = \frac{|y_f|^2}{16\pi^2} [-2\Lambda_p^2 + 6m_f^2 \ln(\Lambda_p/m_f)] , \quad (1.2.4)$$

359 where,  $m_f$  is the mass of the fermion and  $y_f$  is the Yukawa coupling of that fermion to the  
 360 Higgs boson. From Equation 1.2.4, it is evident that the top quark which has  $y_f \approx 1$ , yields  
 361 the largest correction at around 30 orders of magnitude larger than the measured Higgs  
 362 squared-mass, meaning there is either a high degree of ‘fine-tuning’ or there are additional  
 363 quantum corrections from New Physics. SUSY introduces two scalars for each SM fermion  
 364 (one for each of the left- and right-handed fields). The correction to the Higgs mass for a  
 365 scalar,  $S$  is given by

$$\delta m_{H,f}^2 = \frac{\lambda_S}{16\pi^2} [\Lambda_p^2 - 2m_S^2 \ln(\Lambda_p/m_S)] , \quad (1.2.5)$$

366 where  $m_S$  is the mass of the scalar and  $\lambda_S = |y_f^2|$ . Assuming that the scalars have the same  
 367 masses as their SM counterparts, the quadratic component of the corrections to the Higgs  
 368 mass exactly cancel. However, if the superpartners and their SM particles have identical  
 369 masses, observations of SUSY particles would have been made long before the LHC. At  
 370 the time of writing however, no observation of a SUSY particle has been made. In light of  
 371 this, it can be inferred that SUSY must be a spontaneously broken symmetry, in a similar  
 372 manner to the electroweak symmetry of the SM. The exact mechanism through which this  
 373 occurs is not yet known. However, it is possible to break the SUSY symmetry ‘by hand’  
 374 by introducing additional terms in the Lagrangian, as follows:

$$\mathcal{L} = \mathcal{L}_{\text{SUSY}} + \mathcal{L}_{\text{soft}} . \quad (1.2.6)$$

375 In Equation 1.2.6,  $\mathcal{L}_{\text{SUSY}}$  contains all of the Yukawa and gauge interactions, while  $\mathcal{L}_{\text{soft}}$   
 376 contains coupling parameters with positive mass and gauge parameters. The preservation  
 377 of the unbroken SUSY is very important for the resolution of the hierarchy problem, as  
 378 described in the following section.

### 379 R-parity

380 SUSY introduces an additional quantum number, known as R-parity,  $R_p$ . The R-parity  
 381 is constructed using the spin (S), the baryon number (B) and lepton number (L) of the  
 382 incoming and outgoing particles from an interaction vertex. The R-parity is defined as:

$$R_p = (-1)^{3(B-L)+2S} . \quad (1.2.7)$$

383 Using Equation 1.2.7, it can be seen that the SM particles all have  $R_P = +1$ , while  
384 the SUSY particles have  $R_P = -1$ . In SUSY models which conserve R-parity, processes  
385 which violate lepton and baryon number conservation are disallowed, which prevents the  
386 rapid decay of protons to leptons + mesons, a result which is consistent with experimental  
387 observation. The conservation of R-parity has three important consequences:

- 388 • The LSP is required to be stable. In models where the LSP is neutral and weakly-  
389 interacting with the SM, it becomes an excellent candidate for Dark Matter.
- 390 • Each SUSY particle must decay via a chain containing an odd number of LSPs,  
391 mostly just one.
- 392 • SUSY particles are pair-produced in  $pp$  collisions.

### 393 **Electroweak sector mixing**

394 The winos, bino and Higgsinos can mix to form a rich spectrum of electroweak mass eigen-  
395 states. The bino,  $\tilde{B}^0$ , the neutral wino  $\tilde{W}^0$  and the neutralino higgsinos  $\tilde{H}_u^0$  and  $\tilde{H}_d^0$  can mix  
396 to form four neutral mass eigenstates known as neutralinos. The charged winos,  $\tilde{W}^\pm$  and  
397 the charged higgsinos  $\tilde{H}_u^\pm$  and  $\tilde{H}_d^\pm$  can mix to form two charged mass eigenstates known  
398 as charginos. The neutralinos, denoted by  $\tilde{\chi}_i^0$ , where  $i = 1, 2, 3, 4$ , while the charginos are  
399 denoted by  $\tilde{\chi}_i^\pm$ , where  $i = 1, 2$ . By convention, the charginos and neutralinos are labelled  
400 in ascending mass. The lightest neutralino,  $\tilde{\chi}_1^0$ , is generally the lightest supersymmetric  
401 particle (LSP).

402

403 In the R-parity conserving case, the LSP is stable while the heavier charginos and neutrali-  
404 nos ( $\tilde{\chi}_2^\pm, \tilde{\chi}_{3,4}^0$ ) can decay through a chain of decays until a final state containing LSPs and  
405 SM particles is reached. The two-body decay chains of charginos and neutralinos are shown  
406 in Figure 1.8, assuming that the diagrams containing  $H^0, A^0$  and  $H^\pm$  are disfavoured com-  
407 pared to diagrams with  $h^0$  due to its lower mass, and that squarks are heavy and hence  
408 also disfavoured. In the case that the diagrams shown are kinematically-forbidden, decays  
409 can proceed via three-body decays involving SM fermions.

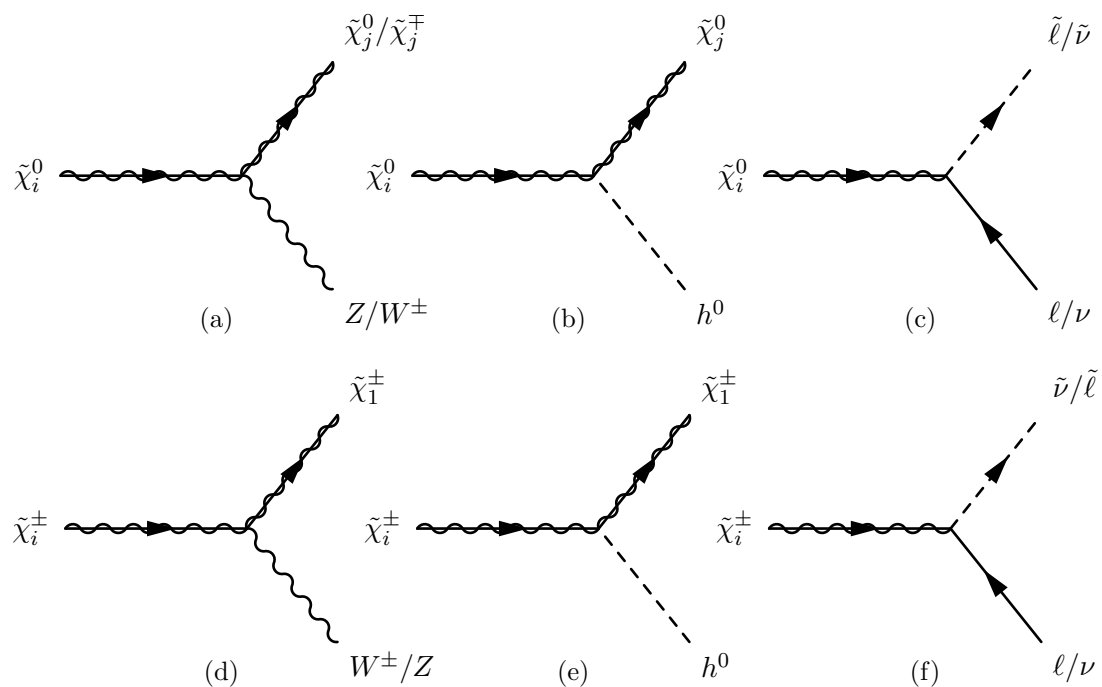


Figure 1.8: Diagrams showing the two-body decays of a given neutralino,  $\tilde{\chi}_i^0$  (1.8a, 1.8b and 1.8c) and chargino,  $\tilde{\chi}_i^\pm$  (1.8d, 1.8e and 1.8f).

## 411 Chapter 2

# 412 The LHC and the ATLAS 413 Experiment

414 The physics analyses detailed in the forthcoming chapters made use of data collected by  
415 the ATLAS detector, one of the four main experiments situated around the Large Hadron  
416 Collider (LHC) at the European Organisation for Nuclear Research (CERN). CERN is  
417 home to the the largest particle physics experiment to date, the LHC. Lying beneath the  
418 Franco-Swiss border at a depth of around 100m, it spans a circumference of almost 27km.  
419 The LHC is a hadron-hadron collider, accelerating counter-circulating beams of protons  
420 (or heavy-ions for a short period every year) to provide collisions at four interactions  
421 points around the LHC; ATLAS, CMS, LHCb and ALICE. This thesis focuses entirely on  
422 proton-proton collisions recorded by the ATLAS experiment.

### 423 2.1 The LHC accelerator

424 The protons for the LHC beams are provided by a bottle of hydrogen gas. Protons are  
425 isolated by applying a strong electric field to hydrogen atoms, stripping away the electrons.  
426 These isolated protons are then transferred to a linear accelerator (LINAC2), where they  
427 undergo the initial acceleration to 50 MeV. Proton acceleration is achieved using Radio  
428 Frequency (RF) cavities. In the Proton Synchrotron (PS), the proton beam is divided into  
429 proton packets known as ‘bunches’, spaced by 25ns intervals, with each bunch containing  
430 around  $\mathcal{O}(10^{11})$  protons. The 50 MeV proton bunches are further accelerated to an energy  
431 of 1.4 GeV by the Proton Synchrotron Booster (PSB) and subsequently to an energy  
432 of 25 GeV by the PS. The Super Proton Synchrotron (SPS) is the penultimate stage of  
433 acceleration, accelerating the 25 GeV proton bunches to an energy of 450 GeV. These  
434 proton bunches are injected into the LHC to produce two counter-circulating beams and  
435 are accelerated from 450 GeV to 6.5 TeV by RF cavities.

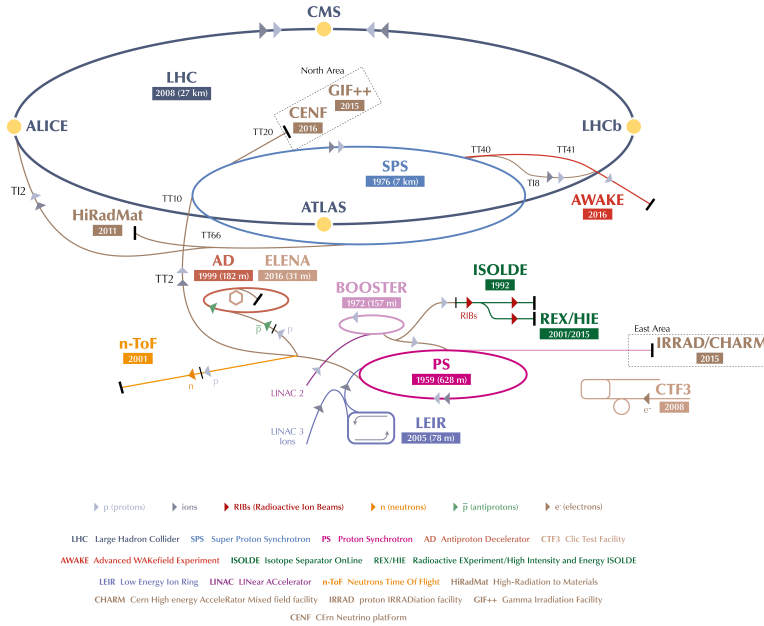


Figure 2.1: A diagram of the CERN accelerator complex. Of importance to the LHC accelerator are LINAC2, PSB, PS, SPS and LHC. [6]

## 2.2 Luminosity and pileup

The amount of data being delivered by LHC and recorded by its experiments is measured by the *luminosity*. The instantaneous luminosity,  $\mathcal{L}$ , of a beam is defined as the number of incident particles per square centimetre per second [ $\text{cm}^{-2}\text{s}^{-1}$ ]. For a circular collider, the expression for the instantaneous luminosity of two colliding beams is given by [7]:

$$\mathcal{L} = f \frac{N_p^2 n_b}{4\pi\sigma_x\sigma_y} F. \quad (2.2.1)$$

In Equation 2.2.1,  $N_p$  is the number of protons per bunch,  $n_b$  the number of bunches in each beam,  $f$  the frequency of bunch crossings ( $1/25\text{ns} = 40\text{MHz}$ ),  $\sigma$  the size of the bunch at the interaction point (IP) and  $F$  a geometrical correction factor accounting for a non-zero crossing angle at the IP. The integrated luminosity (often shortened to ‘luminosity’), is defined as the time-integral of the instantaneous luminosity:  $L = \int \mathcal{L} dt$ .

The luminosity is a measure of the total number of incident particles in a given area in a given time period and has units of an inverse area in square centimetres [ $\text{cm}^{-2}$ ]. However, due to the huge number of incident particles every second, these units are rarely used; instead, integrated luminosity is often quoted in units of ‘barns’, where 1 barn (b) is defined as  $10^{-24}\text{cm}^2$ . For a cross-section quoted in barns, the total number of expected

452 events,  $N_{\text{exp}}$ , in a dataset with integrated luminosity  $L$  and cross-section  $\sigma_{pp \rightarrow X}$  is given  
 453 by  $N_{\text{exp}} = \sigma_{pp \rightarrow X} L$ .

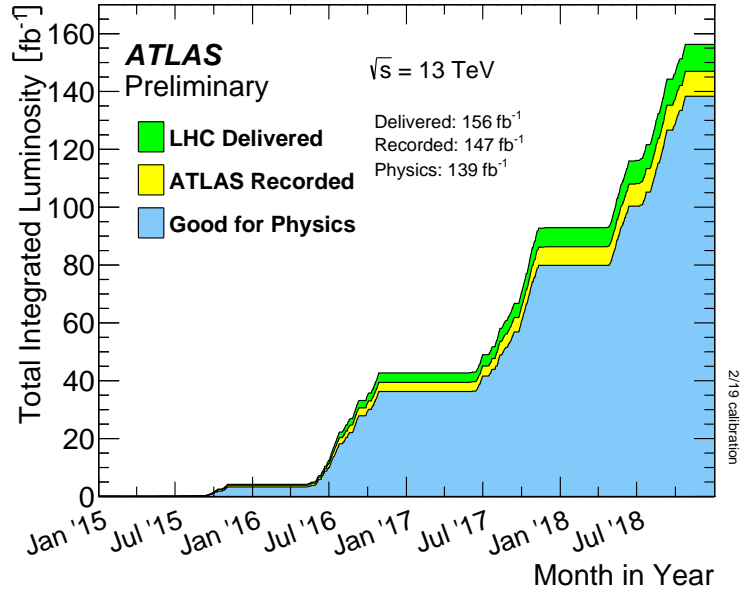


Figure 2.2: Plot showing the total integrated luminosity as a function of time during the Run-2 data-taking period. In total, the LHC delivered  $156 \text{ fb}^{-1}$  of data, with ATLAS recording  $147 \text{ fb}^{-1}$  and  $139 \text{ fb}^{-1}$  being established as suitable for physics analysis.

453

454

455 Due to the bunched beam structure and the intensity of the bunches, multiple inelas-  
 456 tic proton-proton collisions are possible per bunch crossing. Pileup is an important effect  
 457 in high energy physics experiments such as ATLAS, as large amounts of pileup degrade  
 458 the reconstruction performance of an experiment. Pileup events can come from either the  
 459 same bunch crossing, known as in-time pileup, or from the bunch crossing just before or  
 460 after the bunch-crossing being considered, known as out-of-time pileup. The collision, or  
 461 vertex, with at least two tracks and with the highest  $\Sigma p_T^2$  is usually defined as the pri-  
 462 mary vertex, or ‘hard scatter’, in an event. All other vertices, and the resultant final state  
 463 particles, from the same bunch crossing are considered ‘pileup’ events. Figure 2.3 shows  
 464 the pileup profile for each data-taking year for Run-2 of the LHC. The mean number of  
 465 interactions per bunch-crossing is taken as the mean of the Poisson distribution of the  
 466 number of interactions per bunch-crossing calculated for each bunch. It is calculated using  
 467 the per-bunch luminosity, defined as:

$$\mu = L_{\text{bunch}} \times \frac{\sigma_{\text{inel}}}{f_r} . \quad (2.2.2)$$

468 In Eq. 2.2.2,  $L_{\text{bunch}}$  is the per-bunch instantaneous luminosity,  $\sigma_{\text{inel}}$  is the inelastic cross-  
 469 section ( $\sim 80 \text{ mb}$  for Run-2), and  $f_r$  is the bunch-crossing frequency.

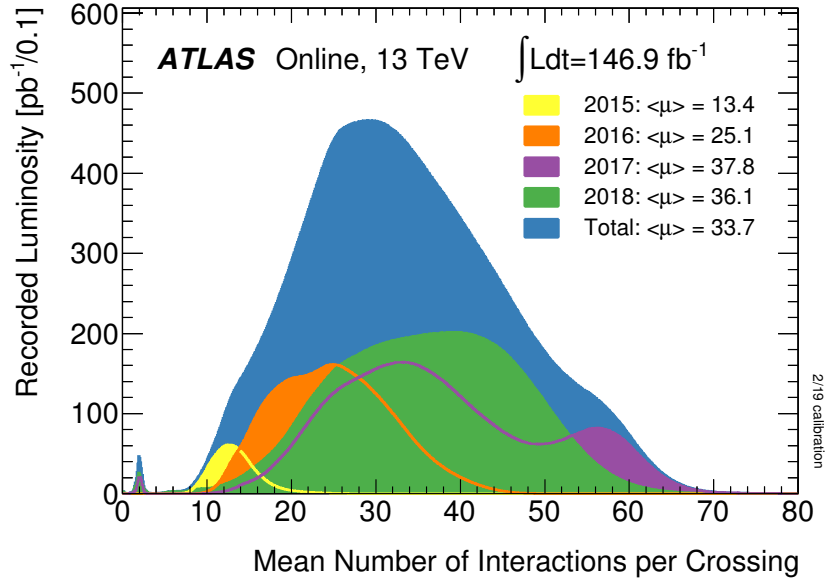


Figure 2.3: Mean number of proton-proton interactions per bunch crossing for Run-2 (2015-2018). The mean number of interactions per bunch-crossing is taken as the mean of the Poisson distribution of the number of interactions per bunch-crossing calculated for each bunch.

## 2.3 ATLAS overview

ATLAS, *A Toroidal LHC ApparatuS*, is one of the two general purpose detectors (GPDs) and is the largest of all of the LHC experiments, at 44m in length and 25m in width and weighing around 7000 tons. Figure 2.4 shows a schematic diagram of the ATLAS detector and its major subsystems. ATLAS is an almost hermetic detector, providing near-full  $4\pi$  tracking and calorimetry through multiple detector subsystems. The ATLAS detector design was optimised for [8]:

- High-efficiency for charged particle reconstruction and identification.
- High-precision calorimetry, providing high-precision electron/photon identification and measurement along with accurate hadronic/ $E_T^{\text{miss}}$  measurements.
- Precise muon momentum measurements using only the muon system, at even the highest luminosity.
- Ability to trigger on objects with low momentum.

ATLAS has four major subsystems; the Inner Detector (ID), the Electromagnetic Calorimeter (ECAL), the Hadronic Calorimeter (HCAL) and the Muon Spectrometer (MS), arranged in concentric layers about the beam pipe. ATLAS is designed to be symmetric in the forward-backward plane about the interaction point (IP), and when discussed

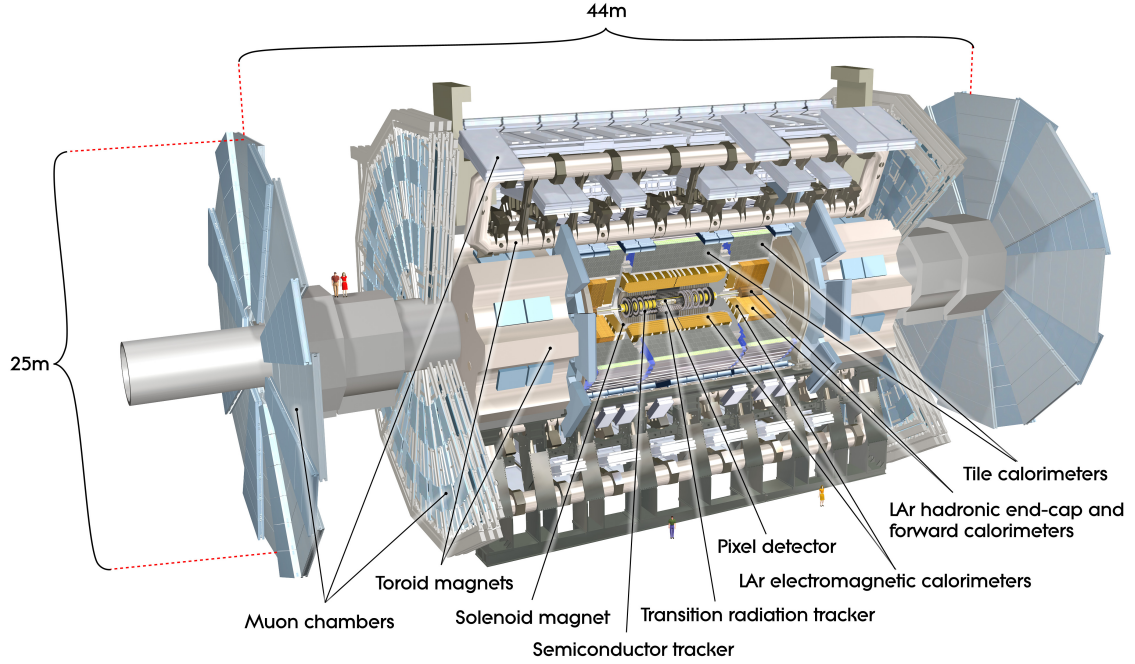


Figure 2.4: Cut-away diagram of the ATLAS detector. [9]

487 is often separated into three segments; the central region, the barrel region and the endcap  
 488 region.

489

490 ATLAS uses a ‘right-handed’ coordinate system; the z-axis is defined in the beam di-  
 491 rection, with the positive x-axis defined to point from the interaction point to the centre  
 492 of the LHC and the positive y-axis being in the upwards direction. Side A of ATLAS, the  
 493 side closer to Geneva Airport, is defined with positive z values, and Side C, closer to the  
 494 Jura mountains, with negative z values.

495

496 The azimuthal angle,  $\phi$ , and the polar angle,  $\theta$ , are defined as the angle around the beam  
 497 axis and the angle from the beam, respectively. From the polar angle, the pseudorapidity  
 498 is defined as  $\eta = -\ln \tan(\frac{\theta}{2})$ . As the partons are highly boosted in the z-direction, and  
 499 the partonic momentum fraction is not exactly known, object measurements are usually  
 500 made in the plane perpendicular to the beam, the transverse plane, such as an object’s  
 501 transverse momentum,  $p_T$  or missing transverse momentum,  $E_T^{\text{miss}}$ .

## 502 2.4 Magnet system

503 When a charged particle of charge  $q$  moves with velocity  $v$  through a magnetic field of  
 504 strength  $|\vec{B}|$ , the force on that particle is given by the Lorentz force,

$$\vec{F} = q\vec{v} \times \vec{B}, \quad (2.4.1)$$

505 where  $\vec{v} \times \vec{B}$  denotes the cross-product of the velocity vector of the particle with the vector  
 506 describing the magnetic field. Due to the presence of the a cross-product in the Lorentz  
 507 force, the force experienced by the charged particle will be perpendicular to both the  
 508 velocity vector and the magnetic field. The deflection of particle tracks by the magnet  
 509 system enables the measurement of the momentum of an incident particle. The ATLAS  
 510 magnet system is constructed from two superconducting magnet systems which enable this;  
 511 a central solenoid (CS) which is surrounded by three toroid magnets. A diagram of the  
 ATLAS magnet system is shown in Figure 2.5.

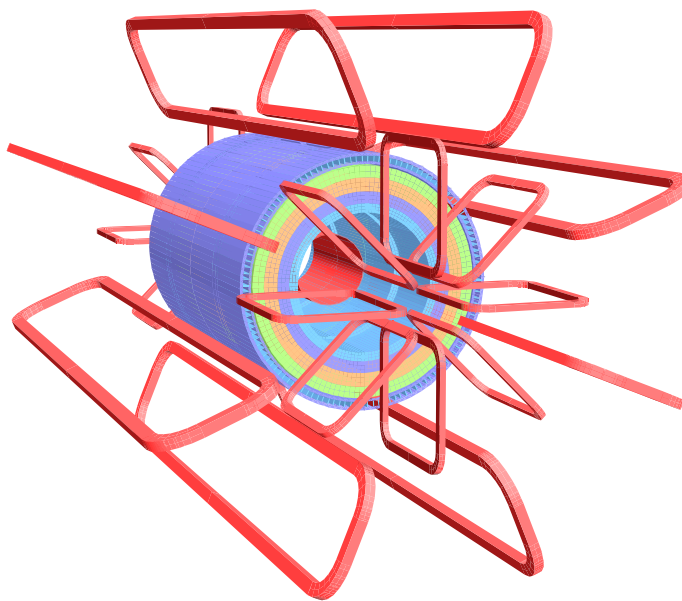


Figure 2.5: Diagram of the ATLAS magnet system, showing the barrel and end-cap toroids in red, while the CS is shown encased by calorimeter layers. [8]

512  
 513 The central solenoid (CS) provides a 2T magnetic field to the Inner Detector, peaking  
 514 at around 2.6T at the magnet itself. The barrel toroid (BT) and endcap toroid (ECT)  
 515 provides a magnetic field between 0.5-1 T for the muon spectrometer, peaking at 3.9T and  
 516 4.1T, respectively. Superconductivity of the magnet system is achieved using liquid helium  
 517 cooled to around 4.5 K.

## 518 2.5 Inner Detector

519 The ATLAS Inner Detector (ID), shown in Fig. 2.6, is the innermost layer of the ATLAS  
 520 detector. It is designed to provide high-precision tracking, vertex information, and for the  
 521 identification of particles. The ID has 3 components; the Pixel detector, the Semiconductor  
 522 Tracker (SCT) and the Transition Radiation Tracker (TRT). The Pixel detector and SCT  
 523 use silicon pixels and strips, respectively, while the latter uses straw detectors to provide  
 524 tracking information. The ID is immersed in a 2T magnetic field provided by the CS,  
 525 allowing precise momentum measurement through the measurement of track deflection.  
 526 The Pixel and SCT detectors provide coverage in  $|\eta| < 2.5$ , while the TRT provides further  
 527 tracking information up to  $|\eta| < 2.0$ .

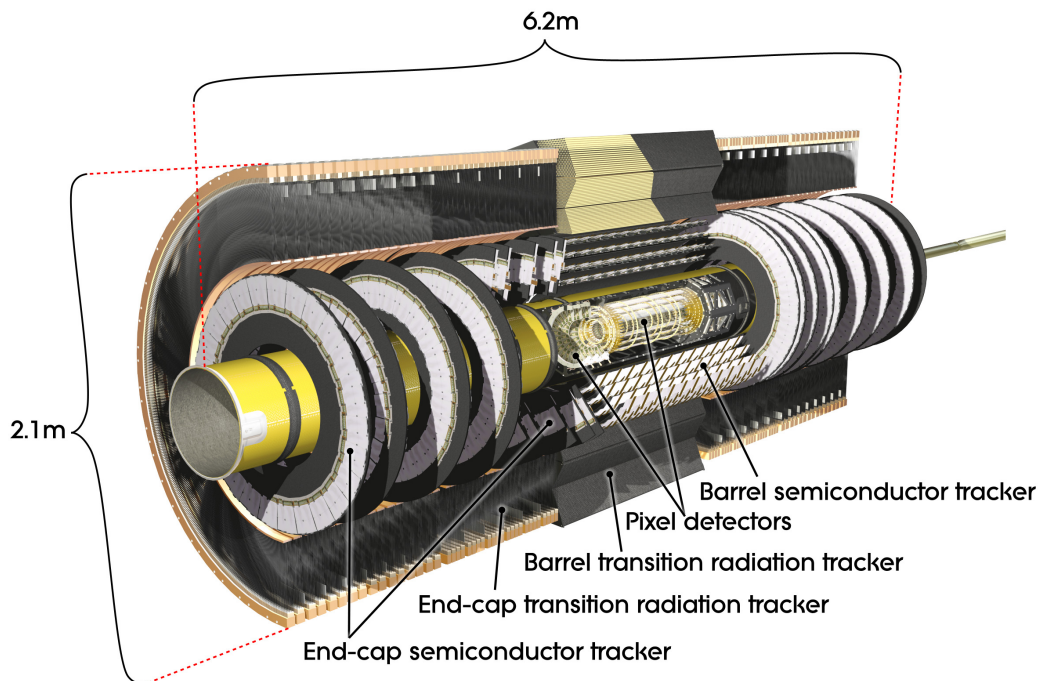


Figure 2.6: Cut-away diagram of the ATLAS Inner Detector. [9]

### 528 Pixel Detector

529 The Pixel Detector uses silicon semiconductor pixels to register particle hits from incident  
 530 particles. Materials which exhibit semiconductive behaviour, such as silicon, have conduc-  
 531 tivity between that of an insulator and a conductor. The silicon pixels used in the Pixel  
 532 Detector are constructed using a p-n junction. A p-n junction is the boundary between two  
 533 silicon semiconductors which are doped to have excess of electrons (n-doped), or an excess  
 534 of holes (p-doped). By applying a forward bias voltage to the pixel, the free electrons and  
 535 holes can migrate across the junction through the depletion region. Conversely, when ap-  
 536 plying a reverse bias, the free electrons and holes are pulled away from the junction. When

Detector component	Modules	Pixel pitch [ $\mu\text{m}$ ]	Resolution [ $\mu\text{m}$ ]
<b>Pixel Detector</b>			
IBL	224	50 x 250	8 ( $R - \phi$ ), 40 ( $z$ )
Barrel	1456	50 x 400	10 ( $R - \phi$ ), 115 ( $z$ )
End-caps	288	50 x 400	10 ( $R - \phi$ ), 115 ( $R$ )
<b>SCT</b>			
Barrel	2112	80	17 ( $R - \phi$ ), 580 ( $z$ )
End-caps	1976	80	17 ( $R - \phi$ ), 580 ( $R$ )

Table 2.1: Table giving a summary of the Pixel Detector and SCT module sizes and resolutions. [8, 10]

537 a sufficient reverse bias is applied, the pixel becomes fully depleted, meaning there is no  
538 current flow between the p-doped and n-doped side of the pixel. When a charged particle  
539 passes through a pixel, electrons and holes are liberated which drift to the electrodes of  
540 the pixel due to applied bias voltage, resulting in the collection of charge which is read out  
541 as a particle hit.

542

543 The Pixel Detector is the ID subsystem closest to the IP. It provides high-granularity,  
544 high-precision measurements of charged particles at radii as little as 3.3cm from the beam  
545 pipe. The system itself is constructed from three barrel modules at radii of  $\sim 4\text{cm}$ ,  $\sim 10\text{cm}$   
546 and  $\sim 13\text{cm}$ , with five disks on either side at radii between 11cm and 20cm. The Pixel  
547 detector has 1744 silicon pixel sensors with a nominal pixel pitch of  $50 \times 400\mu\text{m}^2$  and a  
548 thickness of  $250\mu\text{m}$ . The barrel layers of the Pixel Detector contain 67 million readout  
549 channels, and the disks contain a further 13 million.

550

551 Since the initial detector design, a fourth layer has been added to the Pixel Detector,  
552 at a radius of  $\sim 3\text{cm}$ . This layer is known as the ‘Insertable B-Layer’, or IBL. The IBL was  
553 developed and installed to improve the tracking and  $b$ -tagging performance of the ID in  
554 instantaneous luminosity conditions which exceeded the initial Pixel Detector design. The  
555 Pixel Detector’s efficiency was expected to degrade due to the additional pileup produced  
556 by the higher-than-design instantaneous luminosity, but the inclusion of the IBL helped  
557 to combat this efficiency degradation while also providing an improvement to the impact  
558 parameter resolution. The pixel sensors used in the IBL have a pitch of  $50 \times 250\mu\text{m}^2$ . Table  
559 2.1 summarises the semiconductor modules used in both the Pixel Detector and SCT.

## 560 Semiconductor Tracker

561 The SCT surrounds the Pixel detector, using detection techniques similar to that previously  
562 described for the Pixel detector. The SCT provides up to eight precision measurements

563 per track, aiding in high-precision measurement of charged particle momentum, as well as  
564 contributing to the measurement of the impact parameter and vertex position. The SCT  
565 is constructed from eight layers of silicon microstrip detectors, consisting of 4088 modules.  
566 The eight layers of barrel SCT modules have a total of 2112 microstrip modules with  $80\mu\text{m}$   
567 pitch, at radii between 30cm and 52cm. The SCT provides spatial resolution of  $16\mu\text{m}$  in  $R\phi$   
568 and  $580\mu\text{m}$  in  $z$ , allowing for tracks to be distinguished if they are separated by  $\sim 200\mu\text{m}$ .

## 569 Transition Radiation Tracker

570 The TRT is the outermost layer of the ID, sitting at radii between  $554\text{mm} < r < 1106\text{mm}$ .  
571 The TRT is a straw-tube detector, utilising drift tube detectors to provide upto 36 ad-  
572 ditional measurements of each track. The drift tubes in the TRT are constructed from  
573 Kapton tubes, each of 4mm diameter, with a gold-plated tungsten wire in the centre of  
574 each drift tube with a diameter of  $31\mu\text{m}$ . The wire at the centre of each tube is at ground  
575 potential, while the wall of the tubes are at -1.5 kV. The tubes are filled with a mixture  
576 of xenon (70%), carbon dioxide (27%) and oxygen (3%). When a charged particle passes  
577 through a straw tube, electrons from the gas are liberated through ionisation processes.  
578 These electrons then drift toward the wire in the centre of the straw tube. The current  
579 flow created by the free electrons is registered as a particle hit. In total, the barrel TRT  
580 contains  $\sim 50000$  straws, while the end-caps contain 320000. Polymer fibres and foils fill  
581 the gaps between the straws in the barrel and endcap, respectively. The interface between  
582 the straws and the polymers used to fill the gaps can cause highly-relativistic particles to  
583 emit transition radiation. The probability of the emission of transition radiation depends  
584 upon the relativistic factor  $\gamma = E/m$ , and is hence strongest for lighter particles. Particle  
585 identification using transition radiation is performed to distinguish electrons from pions.

## 586 2.6 Calorimetry

587 The calorimeters in the ATLAS detector are designed to accurately measure the energy  
588 of incident particles. The calorimeter system can be separated into the Electromagnetic  
589 calorimeter (ECAL), the Hadronic calorimeter and the Forward Calorimeter (FCal) sys-  
590 tems, all of which are sampling calorimeters. The ECAL is designed to measure the  
591 energies of incident electrons and photons, as well as any electromagnetically-interacting  
592 components of jets. The Hadronic Calorimeter is designed for measuring the energy of  
593 strongly-interacting objects, namely jets.

594

595 The ATLAS calorimeter systems use alternating layers of absorber material and active  
596 detector material. When a particle enters the absorber material of a calorimeter, a cascade  
597 of particle decays is initiated, known as a shower. Particles which interact via the EM  
598 interaction produce EM showers, in which photons pair-produce electrons and positrons,

599 both of which undergo Bremsstrahlung radiation of photons. Particles which interact via  
 600 the strong force produce much more complex showers. Particle-nucleus interactions in the  
 601 HCAL can produce additional hadrons, such as pions. Charged hadrons, will lose energy  
 602 when traversing the absorber material through ionisation processes. In addition, neutral  
 603 pions in their decay to two photons,  $\pi^0 \rightarrow \gamma\gamma$ , can induce an EM shower component.

604  
 605 The depth of the ATLAS calorimeters is optimised to contain EM showers within the  
 606 ECAL and hadronic showers in the HCAL, hence minimising punch-through into the next  
 607 detector layer. The radiation length,  $X_0$ , of a material is the mean length over which an  
 608 electron will lose all but  $1/e$  of its initial energy, while the interaction length of a material,  
 609  $\lambda$ , characterises the mean distance a hadron will travel through a material before undergo-  
 610 ing a nuclear interaction. The depth of each calorimeter is optimised to fully contain their  
 611 respective shower type.

612  
 613 The two calorimeter systems provide full coverage in  $\phi$  and calorimetry in the range  
 614  $|\eta| < 4.9$ . Complete  $\phi$  coverage is needed for precise reconstruction of  $E_T^{\text{miss}}$ , a prin-  
 615 ciple component of searches using ATLAS. A diagram of the ATLAS calorimeter system  
 616 is shown in Fig. 2.7.

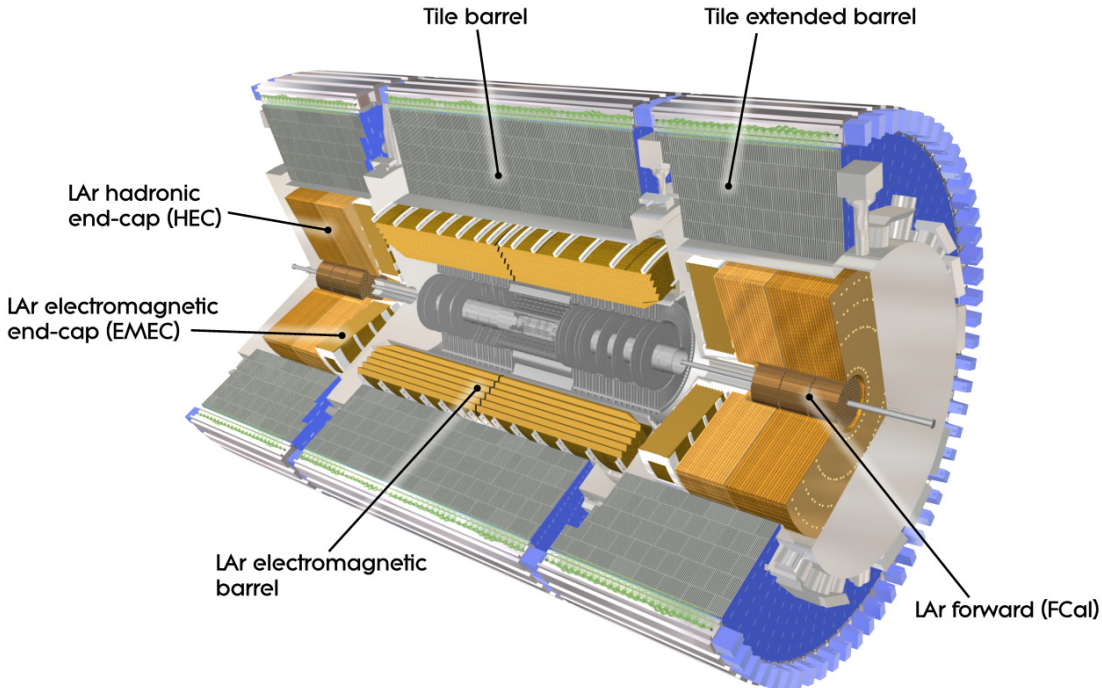


Figure 2.7: Cut-away diagram of the ATLAS Electromagnetic and Hadronic calorimeters. [9]

## 617 **Electromagnetic Calorimeter**

618 The ECAL is comprised of the barrel EM calorimeter which covers the pseudorapidity range  
619  $|\eta| < 1.475$  and the two end-cap EM calorimeters, each covering  $1.375 < |\eta| < 3.2$ . The  
620 ECAL is constructed using lead as the absorber material, while using liquid argon (LAr)  
621 as the active material. When a charged particle passes through the LAr, ionisation occurs,  
622 producing electrons. Using similar principles to the drift tubes described for the TRT, an  
623 electric field is applied, such that the ionisation electrons drift toward the electrodes. The  
624 thickness of the ECAL ranges from 22-38 radiation lengths to fully contain EM showers.

## 625 **Hadronic Calorimeter**

626 The Hadronic Calorimeter, as shown in Figure 2.7, can also be separated into several sub-  
627 systems; the scintillating-tile calorimeter (HCAL), the LAr hadronic endcap calorimeter  
628 (HEC) and the forward calorimeter (FCal).

629  
630 The tile calorimeter covers the range  $|\eta| < 1.7$  and sits adjacent to the the ECAL. It  
631 is separated into a central barrel and two extended barrels. Each of these barrels is com-  
632 prised of 64 modules with a size of  $\Delta\phi \sim 0.1$  made of steel plate absorbers and scintillating  
633 plastic tiles. When charged particles pass through these scintillating tiles, photons with UV  
634 wavelengths are produced from polystyrene. These photons are absorbed and re-emitted  
635 as visible-light photons by wavelength-shifting fluors. This light is collected by fibres and  
636 is transmitted to photomultiplier tubes (PMTs).

637  
638 The HEC is similar in construction to the ECAL, using LAr as the active medium, but  
639 instead of using lead as an absorber, uses copper. The HEC provides coverage in the range  
640  $1.5 < |\eta| < 3.2$ . The HEC is constructed with two sets of wheels, one per end-cap, HEC1  
641 and HEC2, respectively. Each of the four HEC wheels (a front and back wheel per end-cap)  
642 is constructed from 32 identical wedge-shaped modules.

## 643 **Forward Calorimeter**

644 The FCal provides coverage over  $3.1 < |\eta| < 4.9$ . Each FCal is split into three components;  
645 FCal1 is an electromagnetic module, while FCal2 and FCal3 are hadronic modules. FCal1  
646 uses copper as an absorber material, whereas FCal2 and FCal3 use tungsten. All FCal  
647 modules use LAr as the active component.

## 648 **2.7 Muon System**

649 The Muon Spectrometer (MS) is the outermost part of ATLAS. Muons pass through the  
650 entire ATLAS detector before decaying, with a flight distance of  $c\tau \sim 700\text{m}$ , and do not

651 undergo EM showering in the same way as electrons or photons. The main purpose of the  
 652 MS is to detect charged particles escaping the calorimeter systems and measure their mo-  
 653 mentum within the  $|\eta| < 2.7$  range, also providing triggering capabilities within  $|\eta| < 2.4$ .

654

655 The MS comprises four subsystems; Monitored Drift-Tube (MDT) chambers, Cathode  
 656 Strip Chambers (CSCs), Resistive Plate Chambers (RPCs) and Thin Gap Chambers  
 657 (TGCs). The 1150 MDTs cover the  $|\eta| < 2.7$  range with a resolution of  $35\mu\text{m}$  per cham-  
 658 ber. At the innermost layer of the MS, the MDTs are replaced by CSCs in the range  
 659  $2.0 < |\eta| < 2.7$  due to their higher rate capability. The CSCs have a  $z$  resolution of  $40\mu\text{m}$ ,  
 660 and a  $\phi$  resolution of 5mm.

661

662 The triggering capability of the MS is provided by the RPCs and TGCs in the barrel  
 663 and endcaps, respectively. The RPCs have a spacial resolution in  $z$  ( $\phi$ ) of 10mm (10mm)  
 664 and a temporal resolution of 1.5ns, while the TGCs have a spacial resolution in  $R$  ( $\phi$ ) of  
 665 2-6mm (3-7mm) and a temporal resolution of 4ns.

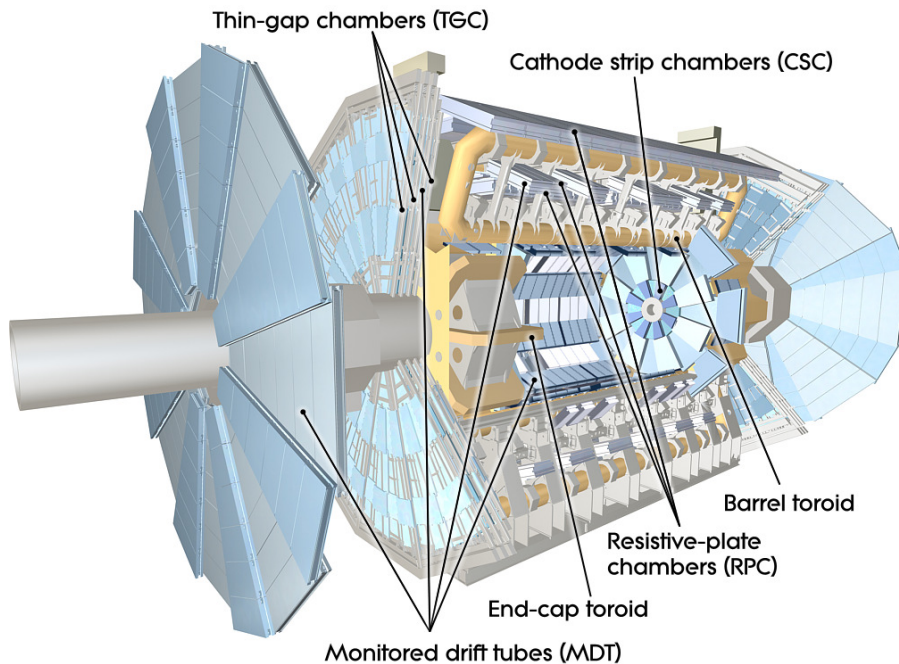


Figure 2.8: Cut-away diagram of the ATLAS Muon Spectrometer. [9]

## 666 2.8 ATLAS Trigger System

667 The temporal bunch-separation provided by LHC in Run-2 is 25ns, meaning the proton-  
 668 proton bunch-crossing frequency is 40 MHz. However, saving all of these events to disk  
 669 is not possible due to the huge bandwidth and storage required, with each event requir-

ing around 1.3MB of storage. Therefore, events which are deemed ‘uninteresting’ are not  
 stored. To achieve this, ATLAS employs a trigger system, which makes rapid decisions on  
 whether to save the event to disk.

673

The ATLAS trigger system consists of the Level-1 (L1) hardware trigger and the software-  
 based High-Level trigger (HLT). The L1 trigger uses coarse detector information from the  
 calorimeters and MS to identify muons, electrons, photons, jets and hadronically-decaying  
 taus with high transverse momentum, or events containing large amounts of total trans-  
 verse energy and  $E_T^{\text{miss}}$ . The L1 trigger uses a subset of the ATLAS subsystems; the RPC  
 and TGC are used for muons, while the calorimeter subsystems are used for EM clusters,  
 jets, tau leptons,  $E_T^{\text{miss}}$  and large total transverse energy. The L1 trigger operates at a  
 maximum of 100kHz, with each decision being made in less than  $2.5\mu\text{s}$ . Regions-of-interest  
 (RoIs) are identified by the L1 trigger; these are regions in  $\eta$  and  $\phi$  containing potential  
 physics objects. These RoIs are used as seeds in the HLT.

684

The software based HLT takes the full event information from the L1 RoI seeds and in-  
 vestigates the RoIs. The event reconstruction used in the HLT is then used to accept or  
 reject the event. The HLT further reduces the event rate to around 1.5kHz. A functional  
 diagram of the trigger and data acquisition system is shown in Figure 2.9.

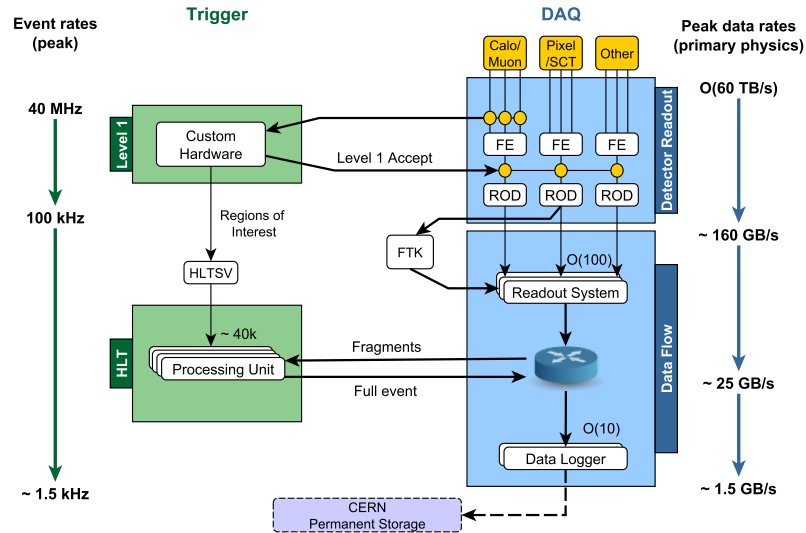


Figure 2.9: A functional diagram of the ATLAS trigger and data acquisition system (TDAQ). The diagram shows the flow of data from detector readout, through the L1 trigger, to the HLT and eventual disk storage. The steps following this are discussed in Chapter 4.

## Chapter 3

# Data and Monte Carlo samples

This Chapter discusses the datasets used in the physics analyses detailed in Chapter 6 and 7, along with the running conditions during data-taking and the triggers used to collect the data. Along with the datasets, the procedure through which Monte Carlo (MC) samples are generated is discussed, along with a brief discussion of the MC generators used in the subsequent Chapters. Finally, this Chapter discusses the complexities of simulating the single top  $Wt$ -channel process due to interference with the  $t\bar{t}$ , and presents studies performed to quantify the effect.

### 3.1 Datasets

The physics analyses discussed in Chapters 6 and 7 used data collected during the Run-2 data-taking period (2015-2018) in  $pp$  collisions at  $\sqrt{s} = 13$  TeV, accumulating  $139\text{fb}^{-1}$  ( $\pm 1.7\%$ ) of collision data in total. The physics analysis described in Chapter 6 used a subset of this data, taken in 2015-2016, with a total integrated luminosity of  $36.1\text{fb}^{-1}$  ( $\pm 2.1\%$ ). In Run-2, proton bunches are separated by 25ns, compared to 50ns in Run-1. Each proton bunch contains  $\mathcal{O}(10^{11})$  protons and as such each bunch-crossing can have multiple  $pp$  interactions. Each proton-proton collision which produces at least two tracks with  $p_T > 0.4$  is classified as a vertex. The collision vertex in each bunch-crossing with the highest  $\sum p_T^2$  of tracks is identified as the Primary Vertex (PV). All other vertices are considered a background to the primary vertex, known as ‘pileup’. Pileup at the LHC is one of the greatest challenges for accurate track reconstruction, and will continue to be so in the HL-LHC phase of operation. The pileup conditions for Run-2 are shown in Figure 2.3.

### Triggers

As previously discussed, it is not possible to save all events to disk due to the huge bandwidth required to readout, partially-reconstruct and trigger on events in real-time. Events passing an L1 trigger are selected and processed with the HLT, and thus events are col-

715 lected at a reduced rate of approximately 1.5kHz. This reduced event rate integrated over  
 716 Run-2 still provides a huge dataset in which to search for evidence of New Physics. At a  
 717 collider experiment, a common signature of the production of BSM particles is the presence  
 718 of large amounts of  $E_T^{\text{miss}}$  in an event, due to the presence of non-SM particles in the final  
 719 state. The analyses described in Chapter 6 and 7 both used  $E_T^{\text{miss}}$  triggers to select events  
 720 in data which may contain non-SM particles. Table 3.1 shows the list of triggers used in  
 721 each data-taking year for the analysis detailed in Chapters 6 and 7.

Year	Triggers
2015	HLT_xe70_mht
2016	HLT_xe90_mht_L1XE50
	HLT_xe100_mht_L1XE50
2017	HLT_xe110_mht_L1XE50
	HLT_xe90_pufit_L1XE50
	HLT_xe110_pufit_L1XE55
2018	HLT_xe110_pufit_xe70_L1XE50
	HLT_xe120_pufit_L1XE50
	HLT_xe110_pufit_xe65_L1XE50
	HLT_xe110_pufit_xe70_L1XE50

Table 3.1: A table showing the list of  $E_T^{\text{miss}}$  triggers used in the analyses described in Chapter 6 and Chapter 7. The trigger highlighted in red is used only in the analysis described in Chapter 6.

722 Due to the evolving conditions throughout each year of data-taking, there are frequently  
 723 multiple triggers listed per year. These are ‘period-dependent’ triggers, and as instanta-  
 724 neous luminosities grow and the pileup profile shifts to higher  $\langle \mu \rangle$ , so too do the trigger  
 725 thresholds. The efficiency of the  $E_T^{\text{miss}}$  trigger in the years 2015-2018 is shown in Figure  
 726 3.1.

727 In order to ensure the trigger accepts events in data and from all MC processes with  
 728 equal efficiency, the analyses detailed in Chapters 6 and 7 require all events are on the  
 729 trigger ‘plateau’, the region of constant efficiency, shown in Figure 3.1 at values above 200  
 730 GeV.

## 731 3.2 Monte Carlo simulation

732 An accurate, precise simulation procedure is required in order to make meaningful compar-  
 733 isons between SM predictions and the data collected by ATLAS, described in the previous  
 734 section. This is known as Monte Carlo (MC) simulation. A generic MC simulation works  
 735 by randomly sampling a process-specific distribution many times to obtain a sample of

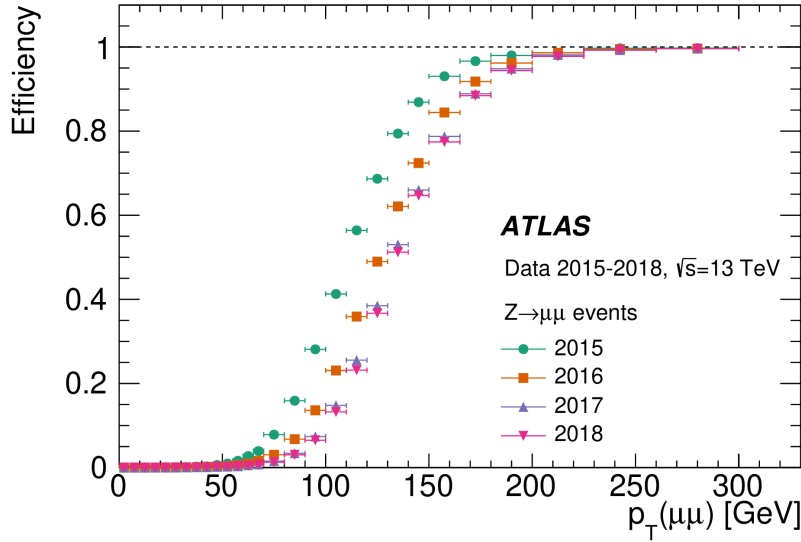


Figure 3.1: A plot showing the efficiency of the lowest unrescaled  $E_T^{\text{miss}}$  trigger from 2015-2018, known as the ‘turn-on’ curve.

736 predictions for that process. In the context of this thesis, MC simulation is used to pro-  
 737 duce simulated samples of SM and BSM processes, produced at the LHC and subsequently  
 738 detected by ATLAS. This simulation process is known as *event generation*.

### 739 MC event generation

740 This section describes the various steps involved in simulating physical processes through  
 741 MC simulation. Typically, this involves: *matrix element calculations (ME)*, *parton show-*  
 742 *ering (PS)*, *hadronisation* and simulation of the *underlying event (UE)*. This chain is rep-  
 743 resented in Figure 3.2. The incoming partons produce a PV, shown by the red circle and  
 744 representing the ME calculation. The remaining partons from the incoming protons are  
 745 also able to interact, producing multi-parton interactions (MPI), resulting in additional,  
 746 softer particles. These softer interactions represent the UE and are shown by the additional  
 747 blue partons and the purple oval. From the PV and the ME portion of the simulation, the  
 748 PS is shown by the red cascade of partons being sequentially emitted. The light green ovals  
 749 show the hadrons present after the PS and the subsequent green circles show the decay  
 750 of these hadrons. Each stage of the event generation procedure will be briefly discussed  
 751 before summarising the MC simulations used to generate background samples used in the  
 752 analyses detailed in Chapters 6 and 7. The details of the signal MC samples will be given  
 753 in the relevant chapters.

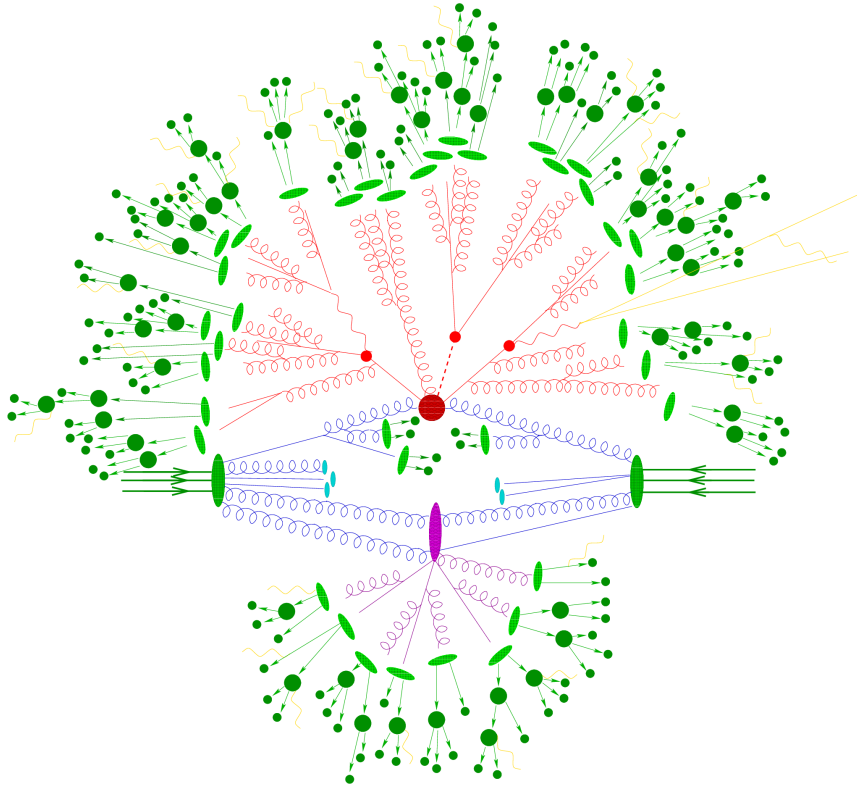


Figure 3.2: A representative diagram showing the MC simulation chain. Blah blah blah.

### 754 Parton distribution functions

755 Due to the composite nature of protons, the collisions at the LHC are actually interactions  
 756 of the partons within the proton;  $qq$  or  $gg$ , for example. Both the valence quarks ( $uud$ ,  
 757 for a proton) and sea quarks (virtual quark-antiquark pairs continually being created and  
 758 annihilated inside the proton) contribute to the parton-parton collisions. Therefore, to  
 759 accurately predict physical processes, the partons within the proton must be well-modelled,  
 760 along with the fraction of the total proton momentum that each parton carries, known as  
 761 the Bjorken  $x$ . Parton Distribution Functions (PDFs) predict the probability that a parton  
 762 of a given type is present inside the proton with a given  $x$ , at a squared energy-scale  $Q^2$ .  
 763 PDF sets are determined through fits to data, namely deep inelastic scattering (DIS) data,  
 764 with data from ATLAS and CMS being included in the most recent global fits to data. [11]

765 PDFs can be calculated to differing orders in QCD, namely leading order (LO), next-to-  
 766 leading order (NLO) and next-to-next-to-leading order (NNLO). The treatment of quark  
 767 flavours is also a consideration when evaluating PDFs. The four-flavour scheme (4FS) and  
 768 five-flavour scheme are the most common treatments of partons for PDFs. In the 4FS,  
 769  $b$ -quarks are treated as massive partons, unlike the other parton types, and the proton  
 770 content is limited to gluons and the  $u$ ,  $d$ ,  $c$  and  $s$  quarks. In the 5FS, all partons are  
 771 treated as massless and the proton can contain gluons and all quarks except the top quark.  
 772 In both flavour-schemes, the  $b$ -quark is included in the final state.

773 **Hard scatter**

774 The hard scatter calculation evaluates the process in which the incoming partons interact  
 775 and undergo some transition into different final state particles, and is the highest-energy  
 776 process evaluated during event generation. The hard scatter calculation is performed by  
 777 evaluating the Feynman diagrams which represent the process of interest to yield the  
 778 matrix element (ME). MEs can be calculated at different orders in QCD. LO MEs have  
 779 two vertices, and hence the ME goes like  $\mathcal{M} \propto \alpha_S^2$ , while the cross-section goes like  $\sigma \propto$   
 780  $|\mathcal{M}^2| \propto \alpha_S^4$ . Most processes relevant at the LHC are calculated at NLO, with  $\mathcal{M} \propto \alpha_S^3$ .  
 Representative LO diagrams for  $t\bar{t}$  are shown in Figure 3.3.

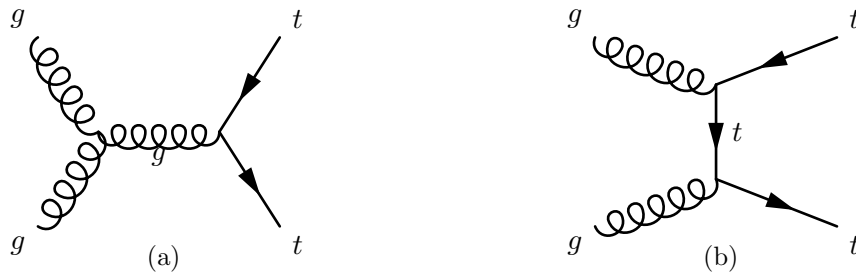


Figure 3.3: This figure shows LO Feynman diagrams for the  $t\bar{t}$  process. These diagrams are also relevant for the discussion of  $t\bar{t}$ - $Wt$  interference later in this Chapter.

781

782 The hard scatter calculation often results in unstable particles in the final state. The  
 783 subsequent stages of the event generation process evolve these hard, unstable particles from  
 784 the highest energy levels down to softer, stable particles.

785 **Parton shower**

786 The PS procedure evolves the hard scatter from an energy scale  $Q^2$  down to the hadro-  
 787 nisation scale  $Q_0^2$  through sequential emissions of quarks and gluons, including soft and  
 788 co-linear emissions. This procedure is repeated until all partons in the event reach the  
 789 ‘cut-off’ point of the hadronisation scale, at around 1 GeV. This procedure takes the event  
 790 from one with only a few final state particles to a complex final state with many quarks  
 791 and gluons.

792 Considerations must be made when applying a PS algorithm to events with additional  
 793 partons in the final state, such as MEs calculated at NLO. For example, an event with  $n$ -jets  
 794 in the final state can be produced in two ways; by evolving an event, through soft/colinear  
 795 emission, produced at the ME-level with  $n$  partons in the final state, or by introducing an  
 796 additional hard parton emission in the PS procedure to an  $n - 1$  parton event. The overlap  
 797 between these two possibilities is treated using a matching/merging procedure.

## 798 Hadronisation

799 The hadronisation procedure starts after the PS at the cut-off scale of around 1 GeV. This  
800 procedure combines the partons present after the PS into colour-neutral states, as required  
801 by QCD. There are two widely-used models of hadronisation; the Lund String model, and  
802 the clustering model. Unstable hadrons are able to decay through allowed SM transitions  
803 until all particles in the final state are stable.

## 804 Underlying event

805 The underlying event refers to all partonic interactions other than the hard scatter. These  
806 interactions can arise from the partons from the incoming protons not involved in the hard  
807 scatter as well as from any additional partons radiated in the event. Additional jets can  
808 arise from the UE, although these are typically much softer than jets produced in the hard  
809 scatter.

## 810 Simulation of SM backgrounds

811 This section details the event generators used for simulating the SM background samples  
812 for the analyses described in the subsequent chapters. For the HL-LHC prospects study  
813 detailed in Chapter 8, the MC samples used were generated without being passed through  
814 the ATLAS detector simulation, but instead a parameterised detector simulation for the  
815 HL-LHC ATLAS detector. This is explained in more detail in Chapter 8 and Appendix A.

## 816 Top processes

817 The POWHEG event generator is used to simulate the hard scatter for both  $t\bar{t}$  and single top  
818 ( $t$ ,  $s$  and  $Wt$ -channels) processes, where the ME is evaluated at NLO accuracy in QCD.  
819 The ME generation is interfaced to PYTHIA for parton showering. The analysis detailed  
820 in Chapter 6 uses PYTHIA6 for PS, while the analysis detailed in Chapter 7 uses a more  
821 recent version, PYTHIA8. The CT10 PDF set is used and the samples are normalised to  
822 the next-to-next-to-leading order and next-to-next-to-leading logarithmic (NNLL) cross-  
823 sections. Simulating  $Wt$ -channel processes at NLO requires additional consideration due  
824 to interference with the  $t\bar{t}$  process, which will be discussed later in this chapter.

825 The  $t\bar{t}V$  ( $V = W, Z$ ) and  $tWZ$  processes are simulated using the `aMC@NLO` generator  
826 to evaluate the ME at NLO accuracy, while  $tZ$  MEs are calculated by `MadGraph`. All  
827 setups are interfaced to PYTHIA8 for PS and use the `NNPDF2.3LO` PDF set.  $t\bar{t}V$  and  $tWZ$   
828 backgrounds are normalised to NLO predictions, while the  $tZ$  background is normalised  
829 to LO.

830 The  $t\bar{t}H$  process is also simulated using `aMC@NLO` for the ME calculation, but is inter-  
831 faced to `HERWIG` for PS. The `CTEQ6L1` PDF set is used and the background is normalised  
832 to the NLO prediction.

833 **Vector boson process**

834  $V$ +jets ( $V = W, Z$ ) processes are simulated using **SHERPA2.2.1** with upto 2 jets at NLO  
 835 accuracy and upto 4 jets at LO. The ME calculation is interfaced to the **SHERPA PS** algo-  
 836 rithm. The **NMPDFNNLO** PDF set is used for generation, with the samples normalised to the  
 837 NNLO prediction.

838 Diboson processes ( $VV$  with  $V = W, Z$ ) are simulated using the **SHERPA2.2.1** generator  
 839 for the ME calculation, performed at NLO accuracy for upto 1 jet and LO for upto 3 jets.  
 840 The **NMPDFNNLO** PDF set is used for the event generation, and the predictions are normalised  
 841 to NLO predictions.

 842 **Simulating  $Wt$ -channel single top at NLO**

843 In many search channels, the  $t\bar{t}$  and single top backgrounds are among the most prominent  
 844 backgrounds due to their relatively high cross-sections and complex, irreducible, multi-  
 845 particle final states which can exactly mimic the final states of many New Physics processes.  
 846 Making predictions of these SM processes at the highest precision possible therefore enables  
 847 searches for New Physics to set the best possible statistical limits, but particular care  
 848 must be taken to treat the interference of  $t\bar{t}$  and  $Wt$ -channel single top correctly. Both the  
 849  $t\bar{t}$  and single top backgrounds are simulated at NLO and normalised to NNLO cross-section  
 850 calculations. At LO,  $Wt$ -channel single top will almost always have a final state containing  
 851  $WWb$ , distinct from the  $WWb\bar{b}$  final state in  $t\bar{t}$  production, as seen by comparing Figure  
 3.3 and 3.4.

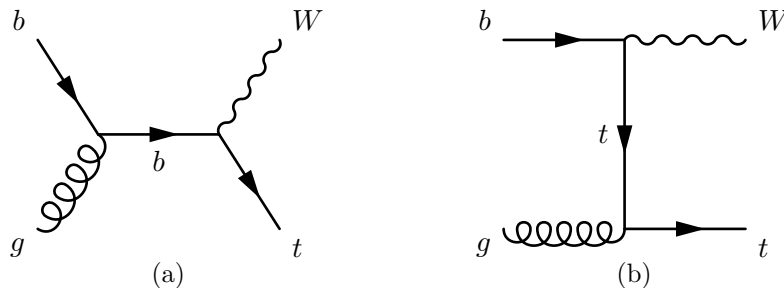


Figure 3.4: Feynman diagrams showing  $Wt$ -channel production at LO, where the final state is distinct from the  $t\bar{t}$  process.

852

853 However, simulating  $Wt$ -channel single top at NLO introduces diagrams which have a  
 854  $WWb\bar{b}$  final state, meaning the  $t\bar{t}$  and  $Wt$  processes can interfere. NLO diagrams for  $Wt$ -  
 855 channel single top are shown in Figure 3.5. When considering the  $WWb\bar{b}$  final state, the  
 856 amplitude can be written as the sum of contributions from the  $t\bar{t}$  and  $Wt$  process. As there  
 857 is overlap between the two processes, diagrams with two resonant (on-shell) top quarks,  
 858 known as ‘double-resonance’ diagrams are attributed to the  $t\bar{t}$  process, while diagrams with  
 859 a single resonant (on-shell) top quark are referred to as ‘single-resonance’ diagrams and

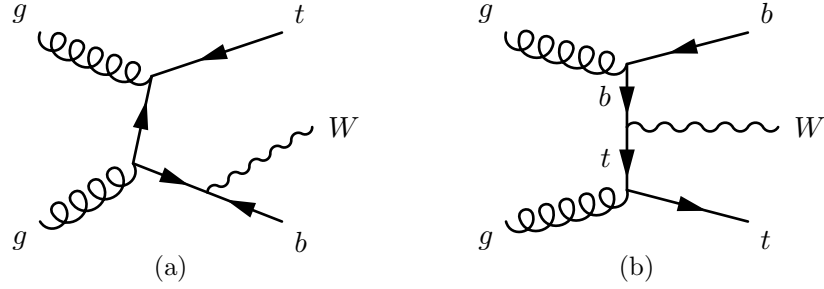


Figure 3.5: Feynman diagrams showing  $Wt$ -channel production at NLO. These diagrams interfere with the  $t\bar{t}$  process due to their identical final state. The  $Wt$  diagrams at NLO can be separated into the number of resonant top quarks present. Figure 3.5b shows a ‘single-resonance’ diagram, while Figure 3.5a shows a ‘double-resonance’ diagram.

860 are attributed to  $Wt$  production. The amplitude can be written as:

$$\mathcal{A}_{WWbb} = \mathcal{A}_{DR} + \mathcal{A}_{SR} \quad (3.2.1)$$

861 where  $DR$  and  $SR$  correspond to the double-resonant and single-resonant components,  
 862 respectively. The production goes with the square of the amplitude, which is where the  
 863 interference terms arise:

$$|\mathcal{A}_{WWbb}|^2 = |\mathcal{A}_{1R}|^2 + |\mathcal{A}_{2R}|^2 + 2\mathcal{R}e(\mathcal{A}_{1R}^*\mathcal{A}_{2R}) \quad (3.2.2)$$

864 The first term on the right side is the contribution from double-resonance diagrams, the  
 865 second term from single-resonance diagrams and the last term from interference between  
 866 the two sets of diagrams. All top-pair MC samples used in this thesis are generated using  
 867 only the diagrams which contribute to  $\mathcal{A}_{2R}$ , having exactly two resonant top quarks. The  
 868 nominal choice for modelling the single top  $Wt$ -channel process uses only the diagrams  
 869 which contribute to  $\mathcal{A}_{1R}$ , neglecting diagrams with two resonant top quarks and hence  
 870 removing any interference from the cross-section. However, it is important to assess the  
 871 size and impact of the interference, especially in the extreme regions of phase space often  
 872 covered by searches for New Physics, as the interference becomes important in regions  
 873 where  $m_{Wb} \sim m_t$ . Two schemes for assessing the impact of the  $t\bar{t}$ - $Wt$  interference are  
 874 used in this thesis and will be discussed in the following subsections.

### 875 **Diagram removal vs. diagram subtraction**

876 As previously mentioned, the nominal method of simulating the  $Wt$ -channel single top  
 877 process is to remove all diagrams with two resonant top quarks; this method is known  
 878 as the *diagram removal* (DR) scheme [12]. An alternate scheme of generation, known as  
 879 *diagram subtraction* (DS) [12] is defined such that single- and double-resonance diagrams

880 are included, and the contribution from the double resonance diagrams is subtracted at  
 881 the cross-section level as follows:

$$d\sigma^{DS} = d\sigma^{WWbb} - d\sigma^{subt} \quad (3.2.3)$$

882 In Equation 3.2.3, the first term on the right is proportional to Equation 3.2.2. In the  
 883 analysis detailed in Chapter 6, the differences between the DR and DS schemes for gen-  
 884 erating the  $Wt$  process were found to  $\mathcal{O}(100\%)$  in *all* analysis regions due to poor MC  
 885 statistics in the DS sample. The difference in the DR and DS prediction in the single top  
 CR of this analysis (described in Table 3.3) is shown in Table 3.2. As seen in Table 3.2, the

Process	MC prediction
$t\bar{t}$	$17.72 \pm 1.85$
Single top (DR)	$28.54 \pm 1.72$
Single top (DS)	$6.61 \pm 1.9$
$W$ +jets	$5.80 \pm 1.32$
$t\bar{t}V$	$3.14 \pm 0.27$
Diboson	$0.84 \pm 0.26$
Small backgrounds	$0.10 \pm 0.05$
Total MC (DR)	$56.1 \pm 2.9$
Total MC (DS)	$34.2 \pm 3.0$
Data	64

Table 3.2: A table showing the estimated yields from MC of SM processes in CRST. The data-MC discrepancy is much larger with the DS  $Wt$  prediction and the region becomes dominated by top-pair production.

886  
 887 DR and DS schemes make drastically different predictions for the single top yield in this  
 888 region. In the case of the DS prediction, the single top purity in this region is no longer  
 889 dominant, becoming subdominant to top-pair production. The data-MC difference of the  
 890 two predictions can be seen in Figure 3.6, showing the  $E_T^{\text{miss}}$  distributions in CRST with  
 891 both the DR and DS  $Wt$  samples.

892 Due to the large differences in the DR and DS predictions observed, an alternate scheme  
 893 for estimating the interference uncertainty was used, and is detailed in the next section.

894 In the analysis detailed in Chapter 7, studies were performed to find a kinematic region to  
 895 use as a CR for the  $Wt$  background, a relatively minor but irreducible background to the  
 896 signal. Using a similar method to those used to optimise the signal selection, as described  
 897 in Section 5.3, a region where the single top background was dominant was found using  
 898 a combination of an adapted random grid search and a genetic algorithm. The kinematic  
 899 selections for this region are summarised in Table 3.3.

900 The estimated yields and purity obtained using these selections are given in Table 3.4.

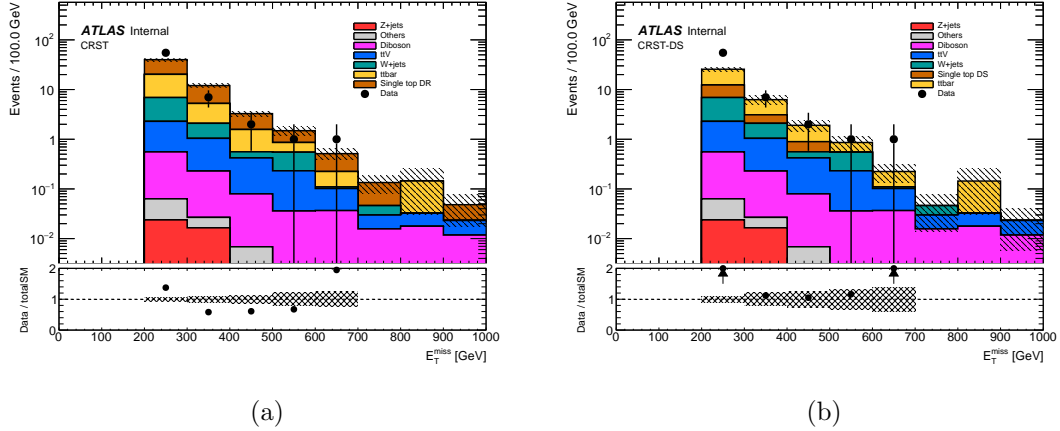


Figure 3.6: Plots showing the  $E_T^{miss}$  distribution in the single top CR of the analysis detailed in Chapter ?? . Figure 3.6a shows the data-MC comparison using the DR single top sample, while Figure 3.6b shows the same comparison using the DS single top sample.

Variable	Selection
$am_{T2}$	$> 220$ GeV
$m_W^{had}$	$< 60$ GeV
$m_T$	$\in [40, 100]$ GeV
$p_T^{b2}$	$> 50$
$\Delta\phi(\ell, E_T^{miss})$	$< 0.5$

Table 3.3: This table shows the selections used, in addition to the preselection cuts listed in Table 7.2, for the single top CR study for the analysis detailed in Chapter 7.

901 The distributions of the subleading  $b$ -jet  $p_T$  and  $\Delta\phi(\ell, E_T^{miss})$ , used to define and isolate  
 902 the  $Wt$  background, is shown in Figure 3.7 for both the DR and DS schemes.

903 Due to the extreme differences in predictions between the DR and DS schemes, and the  
 904 relatively small contribution of  $Wt$  in the SR, this CR was not used in the final analysis,  
 905 detailed in Chapter 7.

### 906 Coherent simulation of $WWbb$ final state

907 An alternative to the comparison of the DR and DS schemes was also used in the analy-  
 908 sis detailed in Chapter 6. This approach uses three sets of complementary MC samples,  
 909 ‘singleres’, ‘doubleres’ and ‘sum’, to simulate the  $WWbb$  final state, generated at LO and  
 910 at truth-level. The ‘singleres’ samples include diagrams with exactly one resonant top  
 911 quark, corresponding to  $\mathcal{A}_{1R}$ , the ‘doubleres’ samples include diagrams with two resonant  
 912 top quarks, corresponding to  $\mathcal{A}_{2R}$  and the ‘sum’ samples include all diagrams with at least  
 913 one resonant top quark, corresponding to  $\mathcal{A}_{WWbb}$ . As these samples are generated at LO,  
 914 these samples are used only as a comparison between themselves, and not the nominal DR

Process	MC prediction
$t\bar{t}$	$135.52 \pm 1.87$
Single top (DR)	$253.39 \pm 8.04$
Single top (DS)	$39.08 \pm 3.2$
$W$ +jets	$134.75 \pm 4.35$
$t\bar{t}V$	$3.41 \pm 0.25$
$Z$ +jets	$0.83 \pm 0.14$
Diboson	$7.66 \pm 0.85$
$t\bar{t}H$	$1.37 \pm 0.1$
$tWZ$	$0.02 \pm 0.03$
Purity (DR)	47.2%
Purity (DS)	12.1%
Data	363

Table 3.4: This table shows the predicted background yields for all SM backgrounds considered, along with the purity of single top for both the DR and DS schemes, and finally the observed data in this region. As can be seen there is a huge discrepancy between the two  $Wt$  generation schemes, with the data being enveloped by the two predictions.

915 prediction, generated at NLO. Figure 3.8 shows comparisons of the shape and normalisa-  
 916 tion of the  $m_T$  and  $m_{CT}$  distributions for the three samples at preselection level and in  
 917 the single top CR.

918 Using the three sets of samples, it is possible to directly estimate the impact of the inter-  
 919 ference, by comparing the MC prediction for the  $Wt$  process with and without interference  
 920 effects. The estimated yield for the  $Wt$  process with the interference effects,  $N_{MC}^{Wt+int}$ , is  
 921 given by:

$$N_{MC}^{Wt+int} = N_{MC}^{sum} - N_{MC}^{doubles} \quad (3.2.4)$$

922 This estimated yield can be directly compared with the prediction for the  $Wt$  process,  
 923  $N_{MC}^{Wt}$ . Table 3.5 shows a comparison of the nominal  $Wt$  DR prediction compared with the  
 924 DS prediction, along with the predictions for the dedicated  $WWbb$  samples, and finally  
 925 showing the predicted  $Wt$  yield including interference effects, calculated using Equation  
 926 3.2.4. It is

927 The uncertainties derived using these samples are detailed in Section ??.

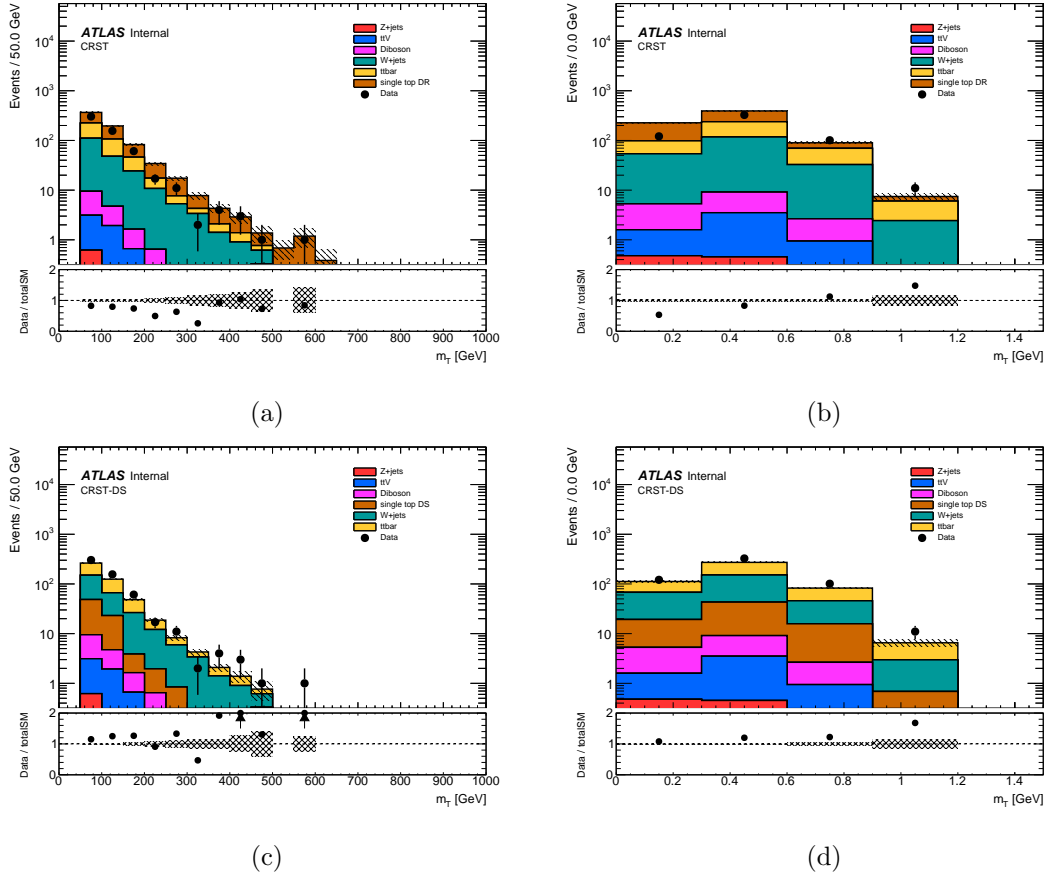


Figure 3.7: This figure compares the two key variables used to isolate the  $Wt$  background for the DR and DS schemes. Large differences are observed between the DR and DS schemes, with the observed data being enveloped by the two.

Region	TRLM	TRMM	TRHM	STCR
Single top (DR)	$22.81 \pm 3.12$	$19.67 \pm 1.51$	$53.11 \pm 2.51$	$28.54 \pm 1.72$
Single top (DS)	$12.25 \pm 2.17$	$13.22 \pm 2.16$	$28.43 \pm 2.97$	$6.61 \pm 1.9$
WWbb singleres	$6.68 \pm 0.05$	$8.62 \pm 0.06$	$21.38 \pm 0.1$	$23.44 \pm 0.11$
WWbb doubleres	$23.28 \pm 0.38$	$80.73 \pm 0.48$	$598.7 \pm 1.29$	$22.26 \pm 0.3$
WWbb sum	$25.37 \pm 0.4$	$84.94 \pm 0.5$	$610.37 \pm 1.34$	$29.97 \pm 0.34$
WWbb singleres + interference	$2.09 \pm 0.55$	$4.21 \pm 0.69$	$11.67 \pm 1.86$	$7.71 \pm 0.45$

Table 3.5: This table shows a comparison of the nominal DR  $Wt$  prediction with the DS prediction, and the predictions of the three sets of  $WWbb$  samples. The value quoted for the  $WWbb$  singleres + interference prediction is calculated using Equation 3.2.4. The DR and DS predictions both use samples reconstructed with the full ATLAS detector simulation, while the  $WWbb$  samples are generated at truth-level.

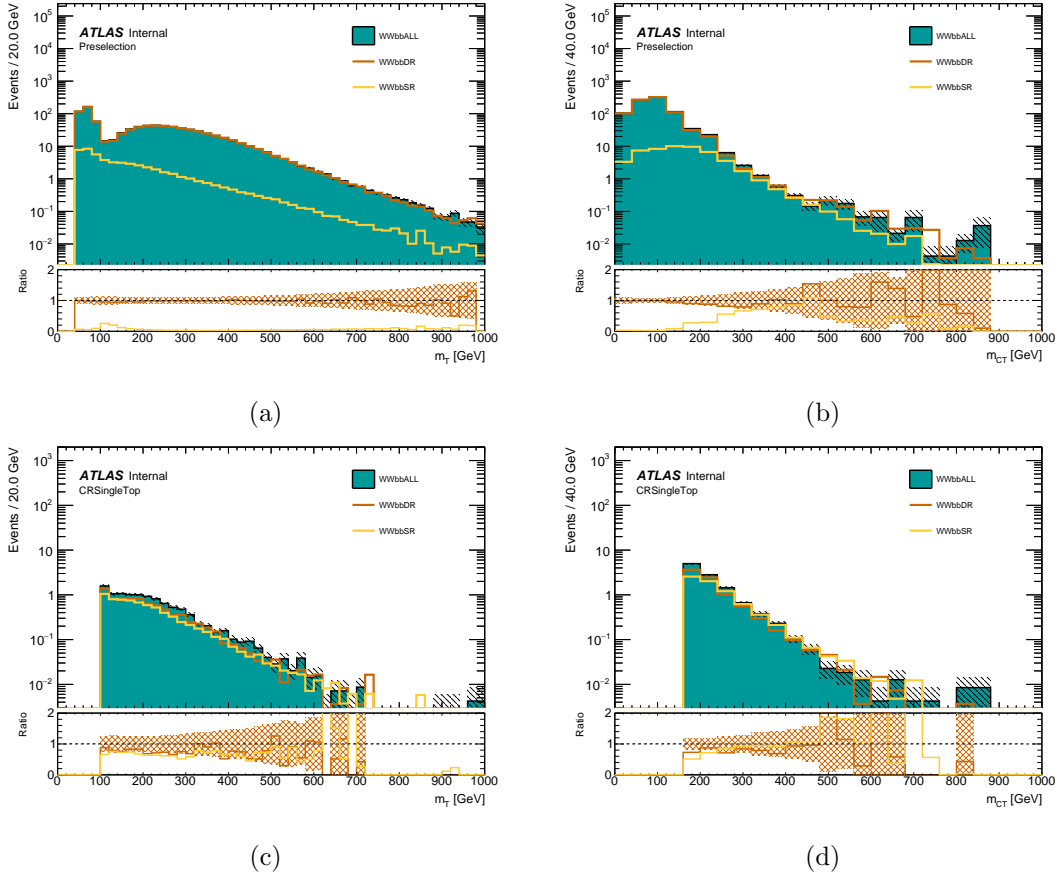


Figure 3.8: This figure shows the difference in shape and normalisation of for the  $WWbb$  singleres, doubleres and sum samples. The ratio in the bottom panel shows the ratio of the singleres and doubleres to the sum, while the hatched error bar shows the sum in quadrature of the MC statistical uncertainty of the sum and doubleres sample. This error is equivalent to the statistical uncertainty on the estimate of the  $Wt$  singleres + interference.

## 928 Chapter 4

# 929 Object reconstruction

930 Particles produced by the  $pp$  collisions inside ATLAS can interact with the detector sub-  
931 systems, as described in Chapter 2, with each type of particle leaving a unique signature.  
932 The combination of the tracking and calorimetry information enables the reconstruction  
933 of the underlying physics of an event. When combining this information, particles are  
934 referred to as physics ‘objects’, with the objects of interest to this Thesis being leptons,  
935 jets and  $E_T^{\text{miss}}$ . This Chapter begins by giving an overview of the different signatures of  
936 each particle type, before summarising the reconstruction techniques for each object.

### 937 4.1 Reconstruction overview

938 The interaction of particles with the detector subsystems is determined by several factors.  
939 Firstly, charged particles create small electrical signals when passing through the tracking  
940 layers of the detector due to ionisation effects, whereas neutral particles pass through the  
941 tracking layers without leaving a signature. Secondly, the particle type will determine  
942 the type of particle shower that occurs when entering the calorimeters, with electrons and  
943 photons depositing almost all of their energy in the ECAL, with particles which interact  
944 via the strong interaction depositing energy in the HCAL. Finally, the presence of particles  
945 which do not interact with the detector subsystems, namely neutrinos and any BSM parti-  
946 cles produced in the event, can be inferred from the total transverse momentum imbalance  
947 of the system, the  $E_T^{\text{miss}}$ . Figure 4.1 shows a representative diagram of the signatures of  
948 various particle types which are reconstructed within ATLAS.

949  
950 By introducing loose requirements on the combination of the tracking and calorimetry  
951 information, ‘baseline’ objects are defined, placing requirements on the  $p_T$ ,  $\eta$  and isolation  
952 of the object. Particle signatures in the same region of the detector can be reconstructed  
953 into multiple objects simultaneously, and thus to circumvent double counting a procedure  
954 is defined to remove overlap between objects, described later in this Chapter. Finally, a  
955 tighter set of requirements is placed upon the objects on a per-analysis basis, known as

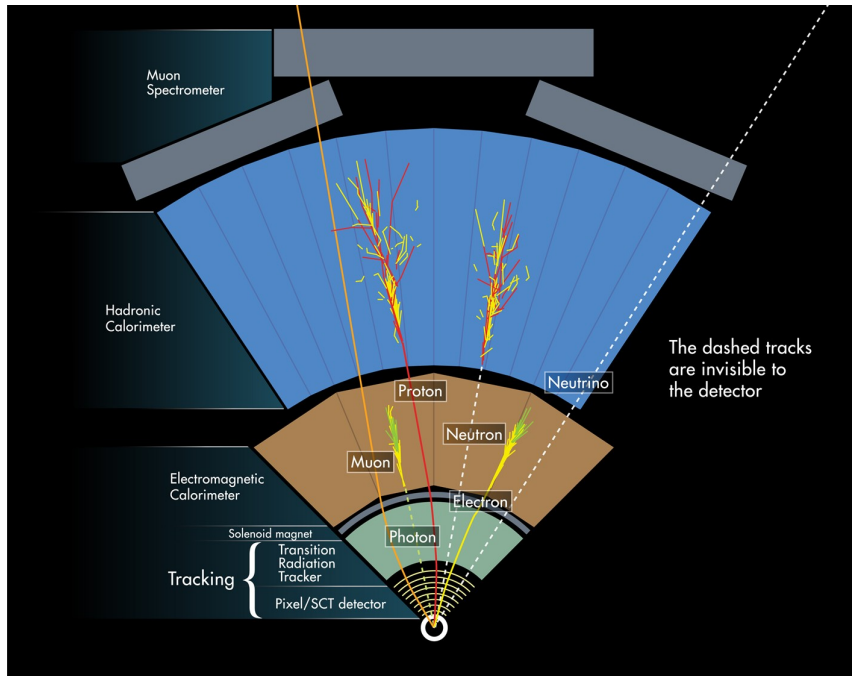


Figure 4.1: This diagram shows the various signatures left by different particles in the ATLAS detector. Solid lines represent a signature left in the corresponding detector subsystem, while dashed lines show the particle did not interact with that detector subsystem. [13]

956 ‘signal’ requirements, which define the objects which enter an analysis.

## 957 4.2 Leptons

958 The signals of interest in the analyses detailed in Chapters 6 and 7 both have a single  
 959 lepton in the final state. In both cases, the lepton originates from the decay of a  $W$  boson  
 960 to  $\ell\nu$ , where the charged lepton is either an electron or muon. This Section will describe  
 961 the reconstruction of electrons and muons, as well as briefly discussing the reconstruction  
 962 of photons and tau leptons.

### 963 Electrons and photons

964 The reconstruction of electrons and photons use information from the ID and ECAL. While  
 965 electrons interact with both subsystems, photons leave no hits in the ID, with their only  
 966 signature being an EM shower in the ECAL. However, photons can undergo a conversion to  
 967 an electron-positron pair when they interact with detector material, and hence the recon-  
 968 struction of electrons and photons proceeds in the same way. Both electrons and photons  
 969 are reconstructed within the range  $|\eta| < 2.47$ , such that full tracking coverage from the  
 970 pixel detector and SCT are available [14,15]. For the first step of electron/ $\gamma$  reconstruction,  
 971 the ECAL is segmented into a  $200 \times 256$  grid in  $\eta \times \phi$ . The energy deposited by an electron

972 or photon at a given  $\eta, \phi$  grid point is evaluated by summing the energy deposits in all  
973 layers of the ECAL, forming a ‘tower’. A sliding-window of size  $3 \times 5$  towers is scanned  
974 over the  $\eta \times \phi$  grid; any point of the grid where the summed  $E_T$  of all towers within the  
975 window exceeds 2.5 GeV is used as a seed for the clustering step.

976

977 In order to identify the ECAL cluster as an electron or photon, the seed clusters are  
978 loosely matched to tracks in the ID. Tracks are extrapolated from the ID to the middle  
979 layer of the ECAL, with any track satisfying  $\Delta\eta < 0.05$  and  $-0.10 < \Delta\phi < 0.05$  considered  
980 as matched to the seed cluster. Seed clusters with at least one matched track are electron  
981 candidates while seed clusters with 0 matched tracks are photon candidates. Finally, the  
982 reconstructed energy of the candidate is determined by extending the window around the  
983 seed cluster to a size of  $3 \times 7$  towers for  $|\eta| < 1.37$  and  $5 \times 5$  for  $1.52 < |\eta| < 2.47$  and  
984 summing the energy deposits within the extended window.

985

986 Identification algorithms are applied to electron and photon candidates in order to quan-  
987 tify the quality of reconstruction and evaluate any potential misidentification. Photons  
988 radiated by electrons through Bremsstrahlung can pair produce electron-positron pairs,  
989 which subsequently interact with the detector material, providing a background to the  
990 prompt electron from the PV. Electron identification is performed in the region  $|\eta| < 2.47$   
991 using a likelihood discriminant, which takes as inputs tracking and calorimetry informa-  
992 tion, as well as quantities constructed from a combination of both tracking and calorimetry  
993 information. Photon identification is performed using selections on calorimeter quantities,  
994 such as quantities related to the shape of the EM shower in the ECAL, as described in [15].

995

996 In order to be applicable to a range of analyses, each with various electron selection ef-  
997 ficiency and background rejection requirements, three working points are defined. The  
998 working points, Loose, Medium and Tight, have efficiencies of 93%, 88% and 80% for a  
999 prompt electron with  $E_T = 40\text{GeV}$ , respectively. The efficiencies of the three working  
1000 points is shown as a function of electron  $E_T$  and  $\eta$  in Figure 4.2.

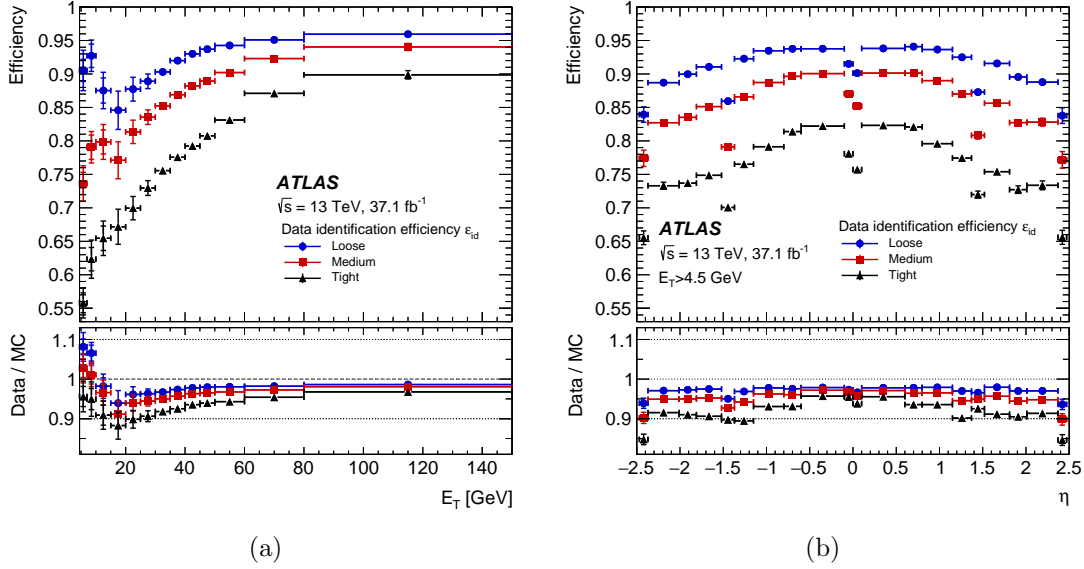


Figure 4.2: Plots showing the electron identification efficiencies for the Loose, Medium and Tight working points, measured in  $Z \rightarrow ee$  events [14], as a function of electron  $p_T$  (4.2a) and  $\eta$  (4.2b).

## 1001 Muons

1002 Muons are identified using inputs from the inner detector (ID) and the muon spectrometer  
 1003 (MS), with additional information being provided by the calorimeters. The ID provides  
 1004 tracking information in the range  $|\eta| < 2.5$ , while the MS provides tracking information in  
 1005 the range  $|\eta| < 2.7$ . Muon reconstruction proceeds independently in the ID and MS; in the  
 1006 ID, muons are treated like any other charged particle, which has been previously discussed  
 1007 in the context of electrons and shall not be repeated here. Muon reconstruction in the MS  
 1008 proceeds by first searching for hit patterns in the individual MS cells, known as segments,  
 1009 and then fitting segments together from different layers to form track candidates. There  
 1010 are four types of reconstructed muon in ATLAS; *Combined (CB)*, *Segment-tagged (ST)*,  
 1011 *Calorimeter-tagged (CT)* and *Extrapolated (ME)* muons. Combined muons use hits in both  
 1012 the ID and MS detectors to build muon tracks, typically taking an ‘outside-in’ approach  
 1013 by starting reconstruction in the MS and matching the track candidate to a track in the ID.

1014

1015 Similarly to electrons, working points are defined for muon identification, enabling analyses  
 1016 to find an optimum balance of muon selection efficiency and background rejection. There  
 1017 are four muon ID working points defined; Loose, Medium, Tight and High- $p_T$ , determining  
 1018 the quality of a muon reconstruction based upon the  $q/p$  significance and  $\rho'$ , defined in [16],  
 1019 as well as the normalised  $\chi^2$  of the combined track fit. The muon reconstruction efficiency  
 1020 as a function of the  $\eta$  is shown in Figure 4.3 for each of the muon identification working  
 1021 points. Muons originating from heavy particles such as the  $W$  boson are often well sepa-

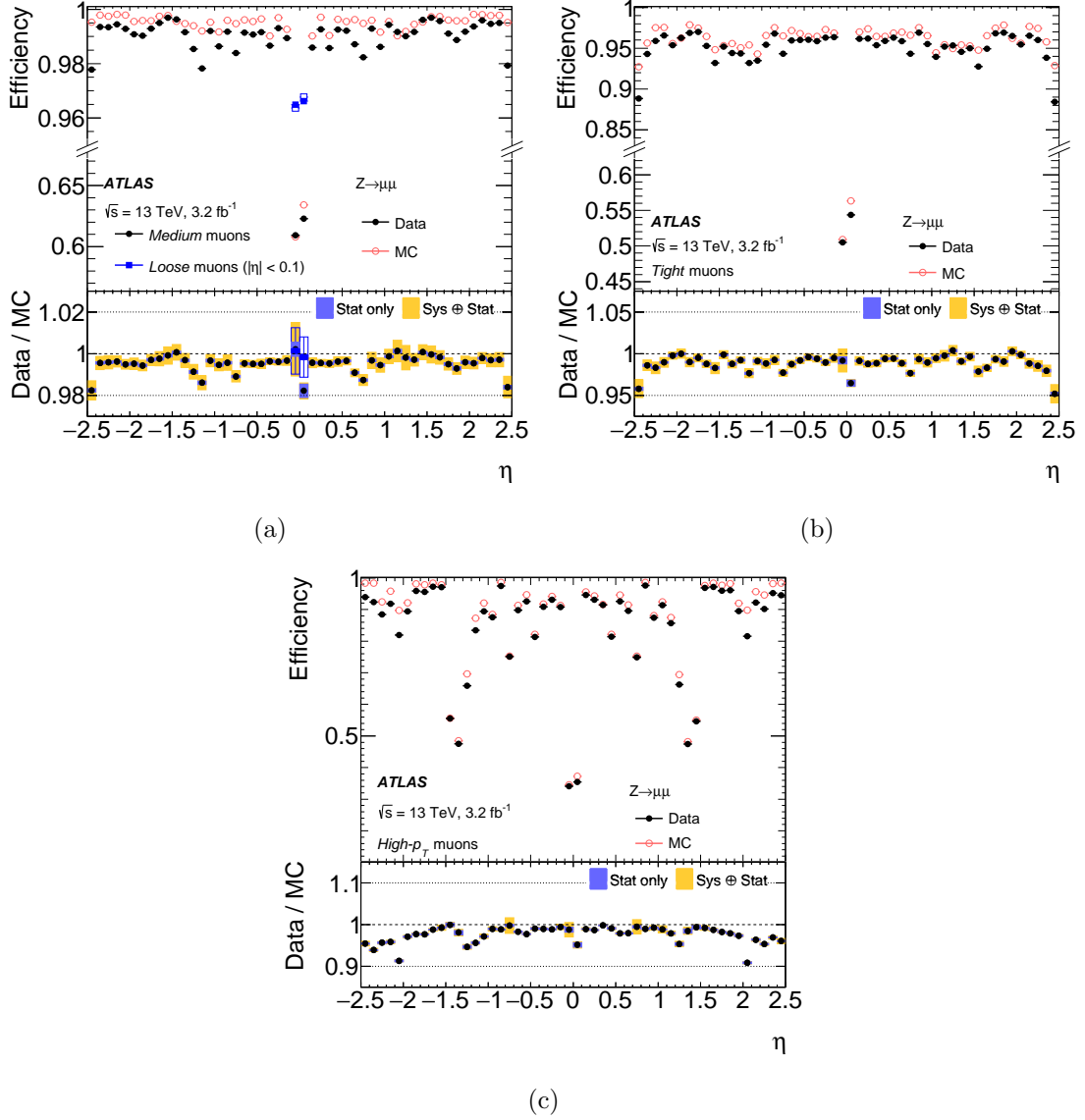


Figure 4.3: Plots showing the muon reconstruction efficiencies for the Loose and Medium (4.3a), Tight (4.3b) and High- $p_T$  (4.3c) working points. All efficiencies are measured in  $Z \rightarrow \mu\mu$  events.

1022 rated from any surrounding particles. Requiring that there is no surrounding activity from  
 1023 a muon, known as the isolation criteria, can be extremely useful for rejecting backgrounds  
 1024 such as QCD. Two muon isolation variables, one track-based and one calorimeter-based,  
 1025 are used to evaluate if a muon is isolated. The distributions of the track- and calorimeter-  
 1026 based isolation variables can be seen in Figure 4.4. Seven muon isolation working points  
 1027 are defined to enable analyses to select an appropriate level of isolation for the signal un-  
 1028 der investigation. The explicit definitions of the muon isolation working points is given  
 1029 in [16].

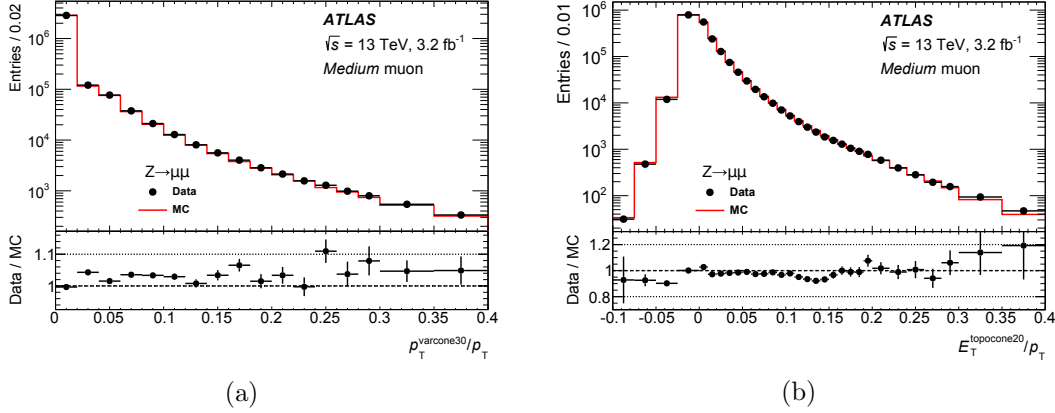


Figure 4.4: Plots showing the distribution of the muon track-based (4.4a) and calorimeter-based (4.4b) for muons identified in  $Z \rightarrow \mu\mu$  events with the Medium working point.

## 1030 Taus

1031 Taus, the heaviest of the charged leptons can decay either leptonically ( $\tau \rightarrow \ell \nu_\ell \nu_\tau$ ,  
 1032  $\ell = e, \mu$ ) or hadronically ( $\tau \rightarrow \text{hadrons } \nu_\tau$ ). The case with a leptonically-decaying tau,  
 1033 denoted by  $\tau_{lep}$ , is simply reconstructed as either an electron or muon, with the neutrinos  
 1034 contributing to the real component of the  $E_T^{\text{miss}}$ . However, there is a dedicated reconstruction  
 1035 and identification flow for hadronically-decaying taus, denoted by  $\tau_{had}$ .  $\tau_{had}$  candidates  
 1036 are seeded from jets (the reconstruction of which is detailed later in this Chapter), with  
 1037  $p_T > 10$  GeV and  $|\eta| < 2.5$ . A tau candidate is identified as the track vertex with the  
 1038 largest momentum fraction from tracks within  $\Delta R < 0.2$  of a seed jet, as well as satisfying  
 1039 the additional requirements detailed in [17]. Tau identification is performed using a BDT,  
 1040 trained to reject QCD backgrounds, using tracking information and the calorimeter cluster-  
 1041 ing information used to reconstruct jets.

1042

## 1043 4.3 Jets

1044 When proton bunches cross inside ATLAS, the environment is extremely dense with quarks  
 1045 and gluons. Strong interactions between partons in the incoming bunches of protons can  
 1046 result in the ejection of quarks and gluons in the transverse plane. The outgoing quarks  
 1047 and gluons evolve through a sequence of hadronisation, gluon splittings and radiations, as  
 1048 described in Section ?? into a complex, highly-collimated collection of particles known as  
 1049 *jets*. The parton-dense environment of each bunch-crossing means  $pp$  collision events usu-  
 1050 ally have numerous jets which can be from the hard scatter event, the proton remnants, or  
 1051 from pileup events. Jets provide an experimental tool for studying the strong interactions  
 1052 of the hard scatter, and are extremely important in the analyses presented in Chapters  
 1053 6 and 7, with both signal processes containing jets originating from the presence of  $b$ -quarks.

1054

1055 For the analyses detailed in Chapters 6 and 7, jet reconstruction begins by first clustering  
 1056 calorimeter cells which are topologically-connected in 3-dimensions, known as ‘topoclus-  
 1057 ters’ [18]. The requirement of cells being topologically-connected helps minimise the  
 1058 misidentification of jets due to electronic noise and pileup, and makes use of the high-  
 1059 granularity of the ATLAS calorimeters. Each calorimeter cell is expected to have a baseline  
 1060 level of noise,  $\sigma_{\text{noise}}$ , which is defined as:

$$\sigma_{\text{noise}} = \sqrt{(\sigma_{\text{noise}}^{\text{electronic}})^2 + (\sigma_{\text{noise}}^{\text{pileup}})^2} \quad (4.3.1)$$

1061 The first step in reconstructing jets using topoclusters proceeds by finding calorimeter  
 1062 cells where the energy deposit is  $E_{\text{cell}} > 4\sigma_{\text{noise}}$ . All cells with  $E_{\text{cell}} > 4\sigma_{\text{noise}}$  form the  
 1063 seed for ‘proto-clusters’, the seed for the following steps of the algorithm. The clustering  
 1064 algorithm then proceeds by finding all cells neighbouring a seed which satisfy  $E_{\text{cell}} > 2\sigma_{\text{noise}}$ .  
 1065 Finally, the clustering algorithm stops when no neighbouring cells satisfies  $E_{\text{cell}} > 2\sigma_{\text{noise}}$   
 1066 but satisfy  $E_{\text{cell}} > 0$ . In the context of this clustering algorithm, ‘neighbouring cells’ can  
 1067 be either adjacent cells in the same layer of the calorimeter, or cells in different calorime-  
 1068 ter layers which have some overlap in  $\eta, \phi$  space. Any protocluster containing more than  
 1069 one local maxima, a cell which has a greater energy deposition than its surrounding cells,  
 1070 are separated around their respective maxima so as not to bias the jet clustering algorithm.

1071

1072 All topoclusters are calibrated to an appropriate energy scale, either hadronic or EM,  
 1073 to account for the energy losses in reconstruction. The ATLAS calorimeters are non-  
 1074 compensating, meaning that an incoming electron,  $e$ , and hadron,  $h$ , both of energy  $E$ ,  
 1075 will have a ratio of measured energy  $E_e/E_h > 1$ . A fraction of the energy of hadronic  
 1076 showers goes unmeasured as it is absorbed in the binding energy of nucleons which are  
 1077 released as the shower evolves in the HCAL [19]. To account for this, corrections are ap-  
 1078 plied to signals identified as coming from a hadronic source. Corrections are also applied  
 1079 to estimate the true energy lost due to the noise-suppression requirements used for forming  
 1080 proto-clusters, as well as corrections for energy loss in any inactive detector material in  
 1081 the region near to the cluster.

## 1082 Jet clustering algorithms

1083 Jet reconstruction proceeds by clustering together the topoclusters described in the previ-  
 1084 ous Section into jets which are determined to have originated from the same parton. Jet  
 1085 clustering algorithms can be separated into cone algorithms and sequential algorithms.

1086 **Cone algorithms** The first jet clustering algorithm was developed in the 1970’s and  
 1087 used in  $e^+e^- \rightarrow q\bar{q} \rightarrow 2j$  events. Events were identified as containing two jets if at least

1088  $1-\epsilon$  of the event’s total energy was contained in two cones with opening half-angle  $\delta$ . The  
 1089 choice of the parameters  $\epsilon$  and  $\delta$  is almost entirely arbitrary, and hence the algorithm can  
 1090 reconstruct vastly different final state jets and multiplicities depending entirely upon the  
 1091 parameter choice. In addition, in  $pp$  collisions the concept of total energy is obfuscated  
 1092 by the fact that the interacting protons contain partons with only a fraction of the total  
 1093 proton energy, with the residual energy either forming the underlying event or escaping  
 1094 down the beam pipe.

1095

1096 Most cone algorithms reconstruct jets through an iterative procedure, hence being known  
 1097 as iterative cones (IC). These algorithms proceed by first selecting a seed particle,  $i$ , and  
 1098 summing the momenta of all particles,  $j$ , satisfying the below condition:

$$\Delta R_{ij} = \sqrt{(y_i - y_j)^2 + (\phi_i - \phi_j)^2} < R. \quad (4.3.2)$$

1099 In the equation above,  $R$  represents the jet radius, which is the modern-day equivalent of  
 1100 the  $\delta$  parameter discussed earlier. This process is repeated, each time taking the result  
 1101 of the previous iteration as the new seed, until the resulting jet cone is stable. This class  
 1102 of algorithms are not fully specified without specifying a definition for seed particles, and  
 1103 for outlining a procedure for removing overlap between cones. Cone algorithms are also  
 1104 plagued by infrared and collinear (IRC) unsafety. An infrared-safe jet clustering algorithm  
 1105 will reconstruct the same set of final state jets regardless of additional soft emissions in an  
 1106 event, while a collinear-safe jet clustering algorithm will reconstruct the same set of final  
 1107 state jets if a parton of energy  $E$  is replaced by two collinear partons whose summed energy  
 1108 is equal to  $E$ . Most IC jet clustering algorithms use the hardest particle in an event as the  
 1109 seed which can violate collinear safety if the hardest particle in the event is replaced by  
 1110 two collinear particles. In this case, the hardest particle in the event may change, meaning  
 1111 the reconstructed final state jets may also change.

1112 **Sequential algorithms** Sequential jet clustering algorithms work in a similar, iterative  
 1113 manner as for IC algorithms, except using a ‘bottom-up’ approach to the clustering. The  
 1114 first use of a sequential clustering algorithm was also in the context of electron-positron col-  
 1115 lisions. There are three widely-used sequential clustering algorithms today; the inclusive- $k_t$   
 1116 algorithm, the Cambridge/Aachen algorithm and the the anti- $k_t$  algorithm. All three of  
 1117 these algorithms can be specified by the following equations.

$$d_{ij} = \min \left( p_{T,i}^{2p}, p_{T,j}^{2p} \right) \frac{\Delta R_{ij}^2}{R^2} \quad (4.3.3)$$

1118

$$\Delta R_{ij}^2 = (y_i - y_j)^2 + (\phi_i - \phi_j)^2 \quad (4.3.4)$$

1119

$$d_{iB} = p_{T,i}^{2p} \quad (4.3.5)$$

1120 In the inclusive- $k_t$  algorithm, the value of  $p$  in Equation 4.3.5 is set to  $+1$ . This algorithm  
 1121 proceeds by iterating over all particles  $j$  within a radius  $R$  of  $i$ , calculating all  $d_{ij}$  and  $d_{iB}$   
 1122 and finding the minimum. If  $d_{ij} < d_{iB}$ , the two particles are combined into a new particle  
 1123 and the algorithm proceeds from the start. If  $d_{ij} > d_{iB}$ , the particle  $i$  is determined to be  
 1124 a final-state jet and is removed from the list of particles, before the algorithm restarts from  
 1125 the beginning. Due to the construction of  $d_{ij}$  in the inclusive- $k_t$  algorithm, an arbitrary  
 1126 number of particles can become final state jets, leading to extremely complex events.  
 1127 The anti- $k_t$  algorithm follows the same procedure as for the inclusive- $k_t$  algorithm, but  
 1128 provides resolution to this issue by setting  $p = -1$  in Equation 4.3.5. Therefore, in the  
 1129 anti- $k_t$  algorithm, jet clustering proceeds from hard seeds, and sequentially adds softer  
 1130 particles until the jet is stable and is classified as a final-state jet. In this thesis, the anti- $k_t$   
 1131 algorithm is used to clustering all jets, with the jet radius parameter  $R$  set equal to 0.4 in  
 1132 all analyses detailed in the subsequent Chapters.

### 1133 Flavour-tagging

1134 For both measurements of SM processes and searches for BSM physics, being able to iden-  
 1135 tify jets originating from heavy flavour ( $c, b$ ) quarks is an extremely useful tool.  $b$ -quarks  
 1136 produced in the hard scatter hadronise and then travel a significant distance before decay-  
 1137 ing. The lifetime of  $b$ -hadrons is relatively long at around  $1.5ps$  because of suppression in  
 1138 the CKM elements for  $V_{ub}$  and  $V_{cb}$ , meaning a  $b$ -hadron can travel several millimetres before  
 1139 decaying. The result of this is the presence of a second decay vertex distinct from the PV,  
 1140 with tracks which have large impact parameters. The impact parameters of a track,  $d_0$  and  
 1141  $z_0$ , represent the transverse and longitudinal distance of closest approach to the PV, re-  
 1142 spectively. This distinctive signature enables jets originating from a  $b$ -quark to be ‘tagged’.

1143

1144 The MV2c10  $b$ -tagging algorithm is used to flavour-tag all  $b$ -jets in the analyses detailed  
 1145 in this Thesis. This algorithm is comprised of a Boosted Decision Tree (BDT), which are  
 1146 described in Section 5.3, which has 21 input variables as described in [20]. The MV2c10  
 1147 algorithm aims to distinguish  $b$ -jets from jets originating from a charm quark, named  $c$ -  
 1148 jets, jets originating from hadronic tau decays, named  $\tau$ -jets and jets originating from  
 1149 light-flavour quarks ( $u, d, s$ ). The output of the MV2c10 BDT is shown in Figure 4.5.

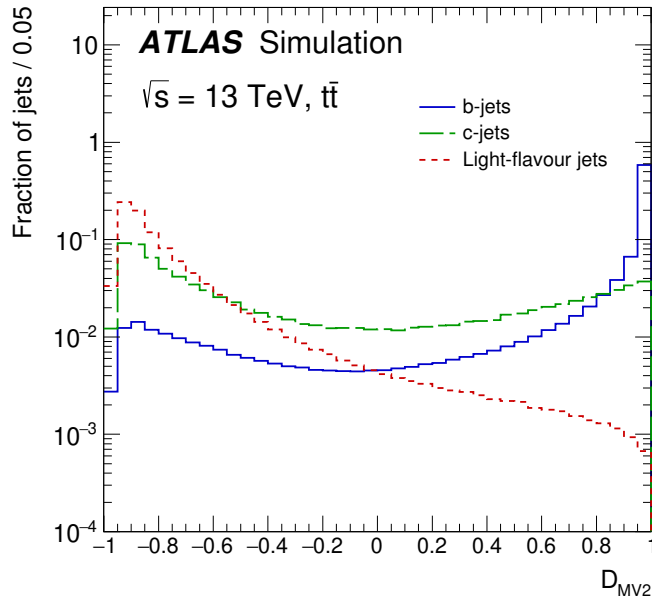


Figure 4.5

1150 Four  $b$ -tagging efficiency working points are available, providing an optimal balance of  
 1151  $b$ -tagging efficiency,  $\epsilon_b$ , and  $c/\tau$ /light-jet rejection. The working point used in the analyses  
 1152 detailed in Chapters 6 and 7 is the  $\epsilon_b = 77\%$  working point, which has a  $c$ -jet rejection of  
 1153 4.9, a  $\tau$ -jet rejection of 15 and a light-jet rejection of 110. The jet rejection rate is defined  
 1154 as the inverse of the selection efficiency,  $1/\epsilon_j$ , where  $j = c, \tau, \text{light}$ . The efficiency of the  
 1155 MV2c10  $b$ -tagging algorithm as a function of jet  $p_T$  is shown in Figure 4.6, along with the  
 corresponding scale factors.

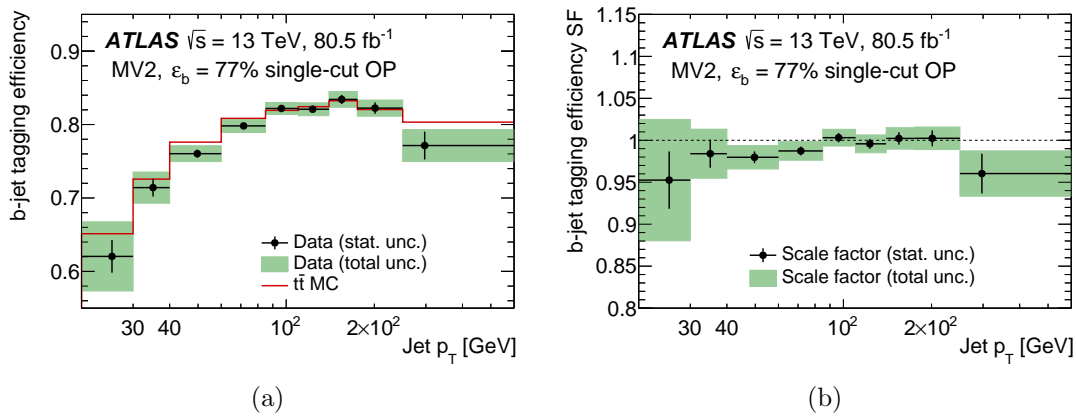


Figure 4.6

1157 **4.4**  $E_T^{\text{miss}}$ 

1158 In searches for New Physics, it is expected that any BSM particles produced in the  $pp$  colli-  
 1159 sions will escape direct detection. Therefore, in order to perform such searches, being able  
 1160 to reconstruct any momentum imbalance, indicating the presence of undetected particles,  
 1161 is crucial. The hermetic design of the ATLAS detector with near  $4\pi$  solid angle coverage,  
 1162 as described in Chapter 2, enables the reconstruction of the momentum imbalance in each  
 1163 event, known as the missing transverse momentum,  $E_T^{\text{miss}}$ .

1164

1165 While the presence of  $E_T^{\text{miss}}$  is a signature of the production of BSM particles, it is not  
 1166 a unique signature of New Physics. As previously mentioned and as shown in Figure  
 1167 4.1, neutrinos pass through the entirety of the ATLAS detector without interacting, and  
 1168 as such any SM decay involving neutrinos can be an irreducible background to a BSM  
 1169 signal. Aside from real  $E_T^{\text{miss}}$  from neutrinos, the accurate measurement of the  $E_T^{\text{miss}}$  is  
 1170 complicated by detector imperfections; for example, physics objects being mismeasured,  
 1171 or particles passing through inactive detector material.

1172

1173 The  $E_T^{\text{miss}}$  is calculated in  $x$  and  $y$  components, as shown in Equation 4.4.1, such that  
 1174 the  $E_T^{\text{miss}}$  vector is given by  $\mathbf{E}_T^{\text{miss}} = (E_x^{\text{miss}}, E_y^{\text{miss}})$ .

$$E_{x(y)}^{\text{miss}} = - \sum_i p_{x(y),i}^{\text{hard}} - \sum_i p_{x(y),i}^{\text{soft}}. \quad (4.4.1)$$

1175 The vectorial representation of  $E_T^{\text{miss}}$  allows both the magnitude and direction in  $\phi$  to be  
 1176 used in physics analyses. The magnitude and direction of the  $\mathbf{E}_T^{\text{miss}}$ ,  $E_T^{\text{miss}}$  and  $\phi^{\text{miss}}$ , are  
 1177 given by Equations 4.4.2 and 4.4.3, respectively.

$$E_T^{\text{miss}} = \sqrt{(E_x^{\text{miss}})^2 + (E_y^{\text{miss}})^2} \quad (4.4.2)$$

1178

$$\phi^{\text{miss}} = \tan^{-1} \left( \frac{E_y^{\text{miss}}}{E_x^{\text{miss}}} \right) \quad (4.4.3)$$

1179 The reconstructed  $E_T^{\text{miss}}$  in ATLAS is constructed from two components; the ‘hard-event’  
 1180 component,  $E_T^{\text{miss, hard}}$ , and the ‘soft-signal’ component,  $E_T^{\text{miss, soft}}$ . The former arises from  
 1181 the reconstruction of the analysis-level electrons, photons, muons,  $\tau_{had}$ , and jets, while the  
 1182 latter arises from tracks and calorimeter deposits which are not associated with any of the  
 1183 final state objects. The analyses described in Chapters 6 and 7 use the Track Soft Term  
 1184 (TST) algorithm to calculate  $E_T^{\text{miss, soft}}$ , including all ID tracks associated with the PV  
 1185 but not associated with any final state object. Using only tracks associated with the PV,  
 1186 and excluded soft, neutral particle contributions, makes the soft  $E_T^{\text{miss}}$  term robust against  
 1187 pileup effects.

## 1188 4.5 Overlap removal

1189 It is possible for multiple objects to be reconstructed from the same detector signatures,  
 1190 such as calorimeter deposits, such that there are overlapping reconstructed objects. It is  
 1191 therefore necessary to define a prescription through which to resolve this overlap. The  
 1192 overlap removal procedure is performed on loosely reconstructed, ‘baseline’ objects and  
 1193 proceeds as follows:

- 1194 - If two electrons share a track in the ID, the lower  $p_T$  electron is rejected.
- 1195 - If an electron shares an ID track with a muon, the electron is rejected.
- 1196 - Any non  $b$ -tagged jets within  $\Delta R = 0.2$  of an electron are rejected, or within  $\Delta R =$   
 1197  $0.2$  of a muon if the jet has  $< 3$  tracks or if the muon and jet are ghost-associated.
- 1198 - For the remaining jets, any electrons or muons satisfying  $\Delta R < \min(0.4, 0.04 +$   
 1199  $10\text{GeV}/p_T)$  are rejected.

1200 Objects remaining after the overlap removal procedure which pass the analysis-level recon-  
 1201 struction criteria form the final analysis objects.

## 1202 4.6 Event cleaning

1203 In order to ensure recorded data events entering analyses are of good quality, a set of event  
 1204 cleaning requirements are used. These requirements aim to remove any events which have  
 1205 noisy detector signals or events which are poorly measured. These are summarised below.

1206 **Good Run List** The Good Run List (GRL) is a record of all runs recorded by the  
 1207 ATLAS detector, which are deemed suitable for use in analyses. Typically, each run is  
 1208 broken down into 60s segments, known as *luminosity blocks*. Luminosity blocks in each  
 1209 run passing basic data quality requirements are included on the GRL. Events which were  
 1210 recorded in luminosity blocks or runs which are not included in the GRL are automatically  
 1211 rejected.

1212 **Trigger** Each analysis has differing trigger requirements depending on the signal topology  
 1213 of interest. In this thesis, the single lepton and  $E_T^{\text{miss}}$  triggers are the most relevant. When  
 1214 using the single lepton trigger, it is required that the fully-reconstructed lepton in the event  
 1215 matches the lepton in the region of interest which fired the trigger.

1216 **Primary Vertex** All events must have a primary vertex (PV). As previously described,  
 1217 the PV is defined as the vertex having at least two tracks with the highest  $\sum p_T^2$ . Events  
 1218 which do not have a vertex satisfying these requirements are rejected.

1219 **SCT, LAr and Tile calorimeter cleaning** Noise bursts in the LAr calorimeter or  
1220 Tile calorimeter trips can give incorrect measurements of the amount of electromagnetic  
1221 or hadronic activity in an event, affecting the data quality. Events where such calorimeter  
1222 activity was recorded are rejected. Events recorded during a reset of the SCT caused by a  
1223 single-event are also rejected.

1224 **Debug Stream** Events which cause the ATLAS software-level trigger, the HLT, to crash  
1225 or timeout form the input to the debug stream. These events are stored and reconstructed  
1226 offline, where they are assigned to the debug stream. It is particular important for analyses  
1227 searching for New Physics to check events in the debug stream.

## 1228 **4.7 Object definitions summary**

1229 The working points and selections on acceptance used to define ‘signal’ objects in the  
1230 analyses detailed in Chapters 6 and 7 are summarised in Table 4.1.

Dataset	SUSY $1l\bar{b}b+E_T^{\text{miss}}$		2HDM+a tW+ $E_T^{\text{miss}}$
	$36.1\text{fb}^{-1}$	$139\text{fb}^{-1}$	$139\text{fb}^{-1}$
<i>Electrons</i>			
ID	TightLLH		
Isolation	Gradient (Loose)	FCLoose	FCLoose
		(FCHighPtCaloOnly for $p_T > 200$ GeV)	
$p_T$	$> 25$ GeV	$> 7$ GeV	$> 20$ GeV
$ \eta $		$< 2.47$	
<i>Muons</i>			
ID	Medium		
Isolation	Gradient (Loose)	FCLoose	FCLoose_FixedRad
$p_T$	$> 25$ GeV	$> 6$ GeV	$> 20$ GeV
$ \eta $	$< 2.7$	$< 2.5$	$< 2.5$
<i>Jets</i>			
Algorithm	anti- $k_t$ , R = 0.4		
$p_T$	$> 25$ GeV	$> 30$ GeV	$> 30$ GeV
$ \eta $	$< 2.8$	$< 2.8$	$< 2.5$
<i>b-jets</i>			
Tagger	MV2c10		
$p_T$	$> 25$ GeV	$> 20$ GeV	$> 20$ GeV
$ \eta $		$< 2.5$	
b-jet efficiency	FixedCutBEff, $\epsilon = 77\%$		

Table 4.1: A summary of the object definitions used in the analyses detailed in Chapters 6 and 7.

## 1231 Chapter 5

# 1232 Analysis methods

1233 This Chapter aims to summarise the methods and tools used to perform the searches for  
1234 New Physics described in the subsequent Chapters. Firstly, the general analysis strategy  
1235 used in a search for New Physics is presented, with more relevant and specific detail given in  
1236 Chapters 6 and 7. The key discriminatory variables used in this Thesis to select candidate  
1237 signal events are described in Section 5.2. Section 5.3 of this Chapter describes some  
1238 of the multivariate and machine learning (ML) methods used to select and optimise the  
1239 acceptance of signal into the analyses, giving an overview of both conventional and more  
1240 modern data selection techniques such as machine learning. Finally, Section 5.5 gives an  
1241 overview of the statistical analysis performed and the methods used to draw statistical  
1242 conclusions from the analyses detailed in the subsequent Chapters.

### 1243 5.1 General search analysis strategy

1244 Physics analyses targeting a BSM scenario generally define three classes of regions of phase  
1245 space. *Signal regions* (SRs) are defined as regions of kinematic phase space which are en-  
1246 riched in the signal of interest. SRs can be defined by placing selections on kinematic and  
1247 angular observables, such as the  $E_T^{\text{miss}}$  or the angular difference between two jets  $\Delta\phi(j_1, j_2)$ ,  
1248 or through more abstract techniques such as placing a selection on some classifier trained  
1249 to distinguish the signal of interest from the SM background. The latter will be discussed  
1250 in Section 5.3.

1251

1252 *Control regions* (CRs) are defined as regions whose composition is dominated by a par-  
1253 ticular background process, such as  $t\bar{t}$ , while also having negligible signal contamination.  
1254 Generally, SRs in searches are in an extreme part of kinematic phase space, far from where  
1255 the SM background MC was validated, hence it is necessary to ensure reasonable agree-  
1256 ment between data and the SM predictions for the background estimates in the CRs. A SM  
1257 estimate is made for the controlled background in the corresponding CR by normalising  
1258 the MC predictions to the observed data in that CR by fitting a floating normalisation

1259 factor, typically denoted by  $\mu_{\text{process}}$ . The background normalisation factor,  $\mu_{\text{process}}$ , is both  
 1260 determined from and subsequently applied to *all* analysis regions included in the statistical  
 1261 analysis. This will be discussed further in Section 5.5.

1262

1263 *Validation regions* (VRs) are used as a method of ensuring the background estimation  
 1264 from the CR extrapolated to the SR is robust. Generally, this is achieved by defining VRs  
 1265 which differ from the SR definition by inverting only one SR selection. By defining multiple  
 1266 VRs, each with a different SR selection inverted, the extrapolation from CR to SR can be  
 1267 validated. However, VRs must also have low signal contamination, such that it is indeed  
 1268 the background estimate that is being validated.

1269

1270 A simplified diagram showing how CRs, VRs and SRs can be defined in terms of two  
 observables is shown in Figure 5.1.

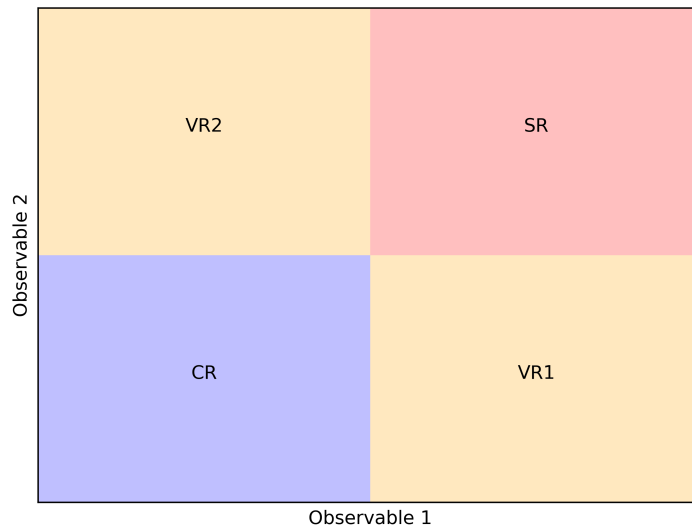


Figure 5.1: A simplified schematic diagram showing an example of a CR, VRs and an SR, all defined by placing orthogonal selections on two observables. The background estimation made in the CR is extrapolated and validated through VR1 and VR2 into the SR.

1271

## 1272 5.2 Discriminant variables

1273 The analyses detailed in Chapters 6 and 7 have similar final states signatures including a  
 1274 single lepton,  $b$ -tagged jets and  $E_{\text{T}}^{\text{miss}}$ , and hence have very similar SM backgrounds to the  
 1275 respective signals. In particular, the presence of intermediate  $W$  bosons and  $E_{\text{T}}^{\text{miss}}$  in the  
 1276 signal processes presented in Chapters ?? and 7 makes SM processes involving  $W$  bosons  
 1277 which decay leptonically an irreducible background to the signal. In addition, backgrounds

1278 containing at least one top quark, where an intermediate  $W$  boson from  $t \rightarrow Wb$  decays  
 1279 leptonically, are also irreducible due to the presence of a lepton,  $E_T^{\text{miss}}$  and  $b$ -tagged jets.  
 1280 In the analyses presented in Chapters 6 and 7, the  $t\bar{t}$ ,  $Wt$  and  $W$ +jets processes are the  
 1281 largest, irreducible backgrounds to the signals of interest. This Section aims to summarise  
 1282 the variables used to reject these SM backgrounds while retaining the signal.

1283

1284 The first, and perhaps most obvious, variable used to discriminate between a BSM signal  
 1285 and the SM backgrounds is  $E_T^{\text{miss}}$ . The construction of the  $E_T^{\text{miss}}$  is described in Chapter 4.  
 1286 Processes which contain BSM particles have real  $E_T^{\text{miss}}$  if the BSM particles do not decay  
 1287 to visible particles, and hence could produce an excess of events in the  $E_T^{\text{miss}}$  distribution.  
 1288 In such events, the amount of  $E_T^{\text{miss}}$  is expected to be larger than the SM background, due  
 1289 to the presence of the additional BSM particles. However, real  $E_T^{\text{miss}}$  from neutrinos in  
 1290  $W \rightarrow \ell\nu$  or  $Z \rightarrow \nu\nu$  decays as well as  $E_T^{\text{miss}}$  from misreconstructed jets can obscure a BSM  
 1291 signal. Therefore, a combination of the  $E_T^{\text{miss}}$  distribution with other kinematic selections  
 1292 is employed.

1293

1294 The transverse mass variable,  $m_T$ , can be used to reconstruct a single, massive particle  
 1295 undergoing a semi-invisible decay to one visible particle and one invisible particle. In this  
 1296 Thesis, the  $m_T$  variable is used to reconstruct  $W$  bosons, decaying to a charged lepton and  
 1297 a neutrino. In the case of an event with no BSM contributions, the only source of  $E_T^{\text{miss}}$  is  
 1298 from the neutrino produced in the decay of the  $W$  boson and as such the  $m_T$  distribution  
 1299 has a kinematic endpoint around  $m_W$ . Detector effects smear the kinematic endpoint of  
 1300 the  $m_T$  distribution to around 100 GeV. The presence of  $E_T^{\text{miss}}$  from BSM particles will  
 1301 produce a significantly different  $m_T$  distribution with a significantly longer tail compared  
 1302 to a SM-only case, and is therefore a powerful discriminant. The definition of  $m_T$  is given  
 1303 in Equation 5.2.1.

$$m_T = \sqrt{2p_T(\ell)E_T^{\text{miss}}(1 - \cos\Delta\phi(\mathbf{p}_T(\ell), \mathbf{p}_T^{\text{miss}}))} \quad (5.2.1)$$

1304 In Equation 5.2.1,  $p_T(\ell)$  is the transverse momentum of the lepton in the event while  
 1305  $\Delta\phi(\mathbf{p}_T(\ell), \mathbf{p}_T^{\text{miss}})$  specifies the azimuthal angle between the lepton and the  $E_T^{\text{miss}}$ . For the  
 1306 signal process of interest in the analysis detailed in Chapter 7, there are two intermediate  
 1307  $W$  bosons, producing the single lepton final state as follows:  $Wt \rightarrow W(Wb) \rightarrow (\ell\nu)(qq')b$ .  
 1308 In addition to reconstructing the leptonically-decaying  $W$  boson using the  $m_T$  variable,  
 1309 the reconstruction of the hadronically-decaying  $W$  boson was achieved using an iterative  
 1310 reconstruction procedure, as described in [21]. The algorithm begins by clustering all of  
 1311 the  $R = 0.4$  anti- $k_t$  jets in an event into large,  $R = 3.0$  jets. The radius of these large  
 1312 jets is then iteratively reduced until a radius which matches the  $p_T$  of the jet, defined by  
 1313  $R(p_T) = 2 \times m_W/p_T$ , is reached. The mass of these ‘reclustered’  $W$  boson candidates is  
 1314 denoted  $m_W^{\text{had}}$ .

1315

1316 The contranverse mass [22, 23],  $m_{CT}$ , is designed to reconstruct the masses of pair-  
 1317 produced particles which both decay in the same, semi-invisible manner. This is par-  
 1318 ticularly useful for rejecting the  $t\bar{t}$  process, where both legs decay into a  $W$  boson and a  
 1319  $b$ -quark, followed by a subsequent decay of the  $W$  bosons. The  $m_{CT}$  is defined in Equation  
 1320 5.2.2.

$$m_{CT}^2 = (E_T(v_1) + E_T(v_2))^2 - (\mathbf{p}_T(v_1) - \mathbf{p}_T(v_2))^2 \quad (5.2.2)$$

1321 The version of  $m_{CT}$  shown in Equation 5.2.2 violates Lorentz invariance under boosts of  
 1322 the laboratory centre-of-mass frame, and hence a modified, ‘boost-corrected’ version [23] is  
 1323 used in the analysis detailed in Chapter ???. For this analysis, the visible particles  $v_1$  and  
 1324  $v_2$  are identified as the two  $b$ -jets in the event,  $b_1$  and  $b_2$ , in order to partially reconstruct  
 1325 the  $t\bar{t}$  system. As described in [23], the  $m_{CT}$  distribution has a kinematic endpoint which  
 1326 can be calculated as shown in Equation 5.2.3.

$$m_{CT}^{\max} = \frac{m_{heavy}^2 - m_{invisible}^2}{m_{heavy}} \quad (5.2.3)$$

1327 Identifying  $m_{heavy} = m_{top}$  and  $m_{invisible} = m_W$  gives a kinematic endpoint around 135  
 1328 GeV for  $t\bar{t}$  production, which is the most dominant background in the analysis detailed in  
 1329 Chapter 6.

1330

1331 The stransverse mass variable,  $m_{T2}$  [24] is closely related to the transverse mass vari-  
 1332 able,  $m_T$ . It is again designed to reconstruct the mass of pair-produced particles, most  
 1333 relevantly here  $t\bar{t}$ , where each particle decays semi-invisibly. The  $m_{T2}$  is shown in Equation  
 1334 5.2.4 for a two-lepton final state.

$$m_{T2} = \min_{\mathbf{q}_T} [\max(m_T(\mathbf{p}_T(\ell_1), \mathbf{q}_T), m_T(\mathbf{p}_T(\ell_2), \mathbf{p}_T^{\text{miss}} - \mathbf{q}_T))] \quad (5.2.4)$$

1335 An asymmetric form of  $m_{T2}$  [25, 26], known as  $am_{T2}$ , is used in the analysis detailed  
 1336 in Chapter 7. When a pair of top quarks are produced and subsequently decay semi-  
 1337 leptonically, a selection applied to  $m_T$  above the  $W$  boson threshold will reject most  
 1338 events. However, for dileptonic  $t\bar{t}$  where one lepton is not reconstructed, cuts applied on  
 1339 the  $m_T$  variable will not be enough to reject this process, as there is  $E_T^{\text{miss}}$  from both legs  
 1340 due to the neutrinos. Selections on the  $am_{T2}$  variable can be applied in combination with  
 1341 selection on  $m_T$  to reject both semi- and dileptonic  $t\bar{t}$  decays.

### 1342 5.3 Selection optimisation methods

1343 Searches for New Physics often involve signals which have cross-sections orders of magni-  
 1344 tude lower than those of SM processes. It is therefore necessary to design analyses which

1345 minimise the background contributions in the SRs, while also maintaining a high accep-  
 1346 tance and selection efficiency for the signal of interest. Optimising SRs to satisfy these  
 1347 criteria is non-trivial, particularly when considering a large number of observables, and  
 1348 can often result in unreasonable computing times and loads.

1349

1350 Placing simple selections on the discriminating variables described previously does not  
 1351 give sensitivity to the signals of interest due to the huge irreducible SM backgrounds. In  
 1352 order to separate signals from the SM background, more sophisticated optimisation meth-  
 1353 ods are used which take advantage of numerous discriminative variables in parallel. The  
 1354 methods used for region optimisation in this Thesis can be divided into two categories;  
 1355 ‘grid-based’ methods, and machine learning methods. Grid-based methods aim to find the  
 1356 optimum selection on each of the discriminative variables used in an analysis. For each  
 1357 variable, a set of proposed selections is defined. Each candidate region is defined as one  
 1358 combination of the proposed selections, with the full set of proposed regions forming a  
 1359 ‘grid’. The total number of candidate regions is given by the product of the number of  
 1360 proposed selections for each variable, and hence rapidly grows as additional variables are  
 1361 added, or more proposed selections are tested. Therefore, for a grid with many candidate  
 1362 regions it is often impossible to test every region, and hence some grid-based algorithms  
 1363 aim to search the grid for an optimal solution without explicitly testing each candidate  
 1364 region. Machine learning (ML) classifiers do not explicitly optimise selections on individual  
 1365 discriminative variables and instead aim to classify events based upon the values of the  
 1366 variables. The inputs to ML classifiers are generally the discriminative variables of interest  
 1367 in an analysis. The classifier is trained to discriminate between the signal and the SM  
 1368 backgrounds by repeatedly being given events from each class and learning the differences  
 1369 between the distributions. ML classifiers make predictions on an event being signal-like or  
 1370 background-like, by outputting a number in the range  $\in [-1, 1]$  or  $\in [0, 1]$ , depending on  
 1371 the classifier implementation, where predictions  $\rightarrow 1$  represent a signal-like event. For ML  
 1372 classifiers, the SRs are defined by applying a lower bound selection to the distribution of  
 1373 the ML classifier predictions. The location of this selection is optimised by scanning over  
 1374 cuts and determining the optimal selection.

1375

1376 In order to determine the optimal solution in grid-based methods and determine the loca-  
 1377 tion of the optimal cut on the ML classifier output, the *significance* metric is defined. The  
 1378 definition of the significance metric used to assess the sensitivity of a region in this Thesis,  
 1379 denoted by  $Z$  and described in detail in [27], is shown in Equation 5.3.1.

$$Z = k\sqrt{2 \left( n \ln \left[ \frac{n(b + \sigma^2)}{b^2 + n\sigma^2} \right] - \frac{b^2}{\sigma^2} \ln \left[ 1 + \frac{\sigma^2(n - b)}{b(b + \sigma^2)} \right] \right)} \quad (5.3.1)$$

1380 In Equation 5.3.1,  $n$  is the number of observed events,  $b$  is the expected number of events,  
 1381 and  $\sigma$  is the uncertainty on the prediction  $b$ . The factor  $k = 1$  for  $n \geq b$ , while  $k = -1$   
 1382 for  $n < b$ . The significance is typically evaluated for several benchmark signal models  
 1383 with specific parameter choices, targeting a particular region of the signal kinematic phase  
 1384 space. In this Thesis, the  $\sigma$  is estimated as being 30%, representing a conservative estimate  
 1385 of the dominant modelling and experimental systematics. A well-optimised SR will max-  
 1386 imise the significance for the targeted signal phase space, while keeping SM background  
 1387 contributions to a minimum. However, in maximising the significance, it must be ensured  
 1388 that the SR is robust against statistical limitations arising from the MC. A SR which is  
 1389 underpopulated in MC events can give an unreasonably-high estimated significance, and  
 1390 as such it is typically required that there are at least 10 events in the MC for each major  
 1391 SM background, and also for the signal MC sample(s) used for region optimisation.

1392

1393 Details on the specific grid-based and ML methods used are given in the following subsec-  
 1394 tions.

## 1395 **Grid-based methods**

1396 Grid-based optimisation methods define a grid of proposed regions, each defined by unique  
 1397 selections on each of the discriminative variables. For each variable, there are  $N_i$  test cuts,  
 1398 where  $i$  denotes the given variable, such that the total number of combinations of cuts,  
 1399  $N$ , is given by  $N = \prod_{i=1}^M N_i$ . As  $N$  is given by a product, the number of combinations  
 1400 rapidly grows with grid granularity and the number of variables tested. In addition, these  
 1401 methods are often run on several benchmark signal models, each with different parameter  
 1402 choices. This ensures good sensitivity can be achieved across a wide range of the available  
 1403 kinematic phase space. Numerous grid-based methods were used in this Thesis, and will  
 1404 now be discussed.

## 1405 **Inclusive grid search**

1406 An ‘inclusive’ grid search finds the optimal combination of selections by calculating the  
 1407 significance for each benchmark signal model for *every* candidate region and returning the  
 1408 region with highest significance for each signal. While this method is guaranteed to find  
 1409 the region with the highest significance for each benchmark signal model, the number of  
 1410 tests rapidly grows with increasing numbers of input variables or with a large number of  
 1411 proposed regions. The limiting factor of this method is the computational time required  
 1412 to find the optimal region through evaluating the significance for every combination. The  
 1413 subsequent grid-based methods evade this issue by randomly sampling points on the grid  
 1414 of candidate regions.

### 1415 **Random grid search**

1416 The random grid search (RGS) algorithm samples random points from the grid of candidate  
1417 regions, evaluating the significance for each. To alleviate the computational requirements  
1418 of the ‘inclusive’ grid search, the RGS algorithm typically samples a small portion of the  
1419 grid, running for  $i$  iterations, calculating the significance at that point, and then removing  
1420 that point from the grid. Due to the random nature of the RGS algorithm, it is never  
1421 guaranteed that the algorithm will find an optimal solution without sampling the entire  
1422 grid. Therefore, the RGS algorithm is run numerous times to ensure the highest significance  
1423 combination it achieved can not be improved. Additionally, the RGS algorithm is run for  
1424 several benchmark signal models, to ensure sensitivity across the kinematic phase space.

### 1425 **Adaptive random grid search**

1426 The RGS algorithm enables a large portion of a potential signal phase space to be probed  
1427 without the computational expensive of studying the phase space grid at every point in-  
1428 clusively. However, the RGS method, by definition, randomly samples the grid of points  
1429 with no ‘awareness’ of the significance. Hence, the RGS algorithm can sample a point with  
1430 high significance, potentially close to the optimal solution, before randomly moving to a  
1431 region of low significance. To circumvent this, a modified version of the RGS algorithm,  
1432 known as the *adaptive* random grid search (ARGS), was developed. Instead of allowing the  
1433 movement between any two points on the grid, the ARGS algorithm adapts the step size  
1434 in a significance-aware way. Around regions of high significance, where  $Z \geq 2$ , the step size  
1435 shrinks to allow a high-granularity study of the phase space around the point of interest.  
1436 Once the significance falls below  $Z = 2$ , the step size grows again to allow bigger steps  
1437 between grid points. Finally, once the significance drops below the activation threshold,  
1438  $Z = 0.5$ , the algorithm is free to move between any points on the grid, and is equivalent  
1439 to the RGS algorithm.

### 1440 **Genetic algorithm**

1441 The genetic algorithm (GA) takes inspiration from the process of natural selection, in  
1442 which the ‘fittest’ individuals survive the sequential evolution of the system. The GA  
1443 starts by generating a ‘population’ of  $N$  combinations of cuts. The significance of each  
1444 combination is calculated, with the lowest 50% of combinations discarded. The surviving  
1445 50% of combinations, known as the ‘parents’, are then copied, and undergo ‘cross-over’  
1446 and ‘mutation’, to produce ‘offspring’. For the cross-over step, the offspring are ordered  
1447 in terms of significance. In the cross-over step, adjacent offspring randomly switch values  
1448 of cuts, while in the subsequent mutation step, random cut values are smeared using  
1449 a Gaussian distribution. The significance of both the parents and the offspring are re-  
1450 evaluated, and the process repeats, selecting the best-performing 50%. This process repeats

1451 for a predefined number of iterations,  $i = 100$ , terminating early if the best significance  
1452 found doesn't improve in 10 iterations.

## 1453 Machine learning methods

1454 Machine learning (ML) techniques are a wide and active area of research, and this section  
1455 does not aim to review the state of ML research. Instead, it aims only to give an overview  
1456 of the usage of ML in this context and describe the ML methods used in this Thesis, in  
1457 particular the use of supervised learning ML *classifiers* to separate a signal from the SM  
1458 background. Two types of classifier are relevant in this Thesis; Boosted Decision Trees  
1459 (BDTs) and Deep Neural Networks (DNNs). Each will be described in their own section,  
1460 along with details of their implementation.

1461  
1462 ML models are, when first created, a completely general model described by a set of  
1463 parameters, known as *hyperparameters*. The set of hyperparameters used are chosen to  
1464 maximise the performance of the model, while allowing the model to be robust against un-  
1465 seen data. The ML models used in this Thesis, as previously mentioned, act as classifiers,  
1466 predicting on an event-by-event basis which of a finite number of classes an event belongs  
1467 to. This is particularly useful in searches, where one wishes to discriminate a signal from an  
1468 often irreducible SM background. To give these models the ability to discriminate between  
1469 the SM backgrounds and signal, they undergo *training*. The models are trained on MC,  
1470 meaning the class of each event is known during the training phase, which is known as  
1471 *supervised* learning. ML models can be susceptible to learning the input events and hence  
1472 become unable to make meaningful predictions about unseen data, known as *overtraining*.  
1473 In order to overcome this, the performance of the model is evaluated on a statistically-  
1474 independent sample of events, known as the *validation* sample.

1475  
1476 While the structure of each type of ML model is different, the inputs to and outputs  
1477 of the models are the same. The inputs to the ML models used in this Thesis are physical  
1478 observables, such as the amount of  $E_T^{\text{miss}}$  or the transverse momentum of the objects in  
1479 the event. The outputs of the ML models used are a number within in a fixed range. In  
1480 the case of binary classification, where only two classes are defined, the output of the ML  
1481 model is in the range  $\in [-1, 1]$  for classifiers implemented in TMVA [28], and otherwise  
1482  $\in [0, 1]$ . For multiclass classification, where the number of classes  $N_{\text{class}} > 2$ , the ML  
1483 model outputs  $N_{\text{class}}$  values in the range  $\in [0, 1]$ , the sum of which are 1, where each value  
1484 represents the prediction for a given class. In this case, events are assigned a class based  
1485 upon which class score was highest.

## 1486 **Boosted Decision Trees**

1487 Boosted Decision Trees (BDTs) are constructed from an ensemble of decision trees, known  
1488 as *weak classifiers*. Decision trees are constructed from nodes and leaves, with each node  
1489 representing a test condition on one of the input variables, and each leaf representing a  
1490 class label. Each individual decision tree has limited discrimination power when evaluated,  
1491 and hence techniques such as *boosting* [29] are used to create an ensemble of weak classifiers  
1492 with strong discrimination power. The boosting technique proceeds by iteratively creat-  
1493 ing trees and assigning each tree a corresponding weight,  $w_i$ , related to the classification  
1494 accuracy of the tree.

1495

1496 During the training phase, the boosting procedure is used to minimise the differences  
1497 between the prediction of the classifier,  $F(\mathbf{x})$ , given the inputs  $\mathbf{x}$ , and the true class of the  
1498 input data,  $y_{\text{truth}}$ . The difference between the prediction of a classifier and the true class  
1499 of an event is calculated using a *loss function*. The BDTs implemented in TMVA utilise  
1500 the AdaBoost algorithm [30], while the BDTs implemented in XGBoost [31] use gradient  
1501 boosting. During training, the AdaBoost algorithm proceeds by adjusting the weight of  
1502 each decision tree in the ensemble to minimise an exponential loss function. However,  
1503 the gradient boosting algorithm creates a new tree at each training iteration, fitted to the  
1504 residual  $y_{\text{truth}} - F(\mathbf{x})$ , to minimise a logarithmic loss function.

1505

1506 The studies performed in Chapter 8 use BDTs implemented with TMVA. These BDTs  
1507 use an inverse sigmoid transformation on the output of the form  $y' = -\tau^{-1}\ln(y^{-1} - 1)$ ,  
1508 where  $\tau = 15$  [28]. The studies presented in Section 6.6 use BDTs implemented with  
1509 XGBoost.

## 1510 **Neural Networks**

1511 Neural Networks (NNs) take inspiration from the structure of neural connections in the  
1512 brain. A neural network is constructed from an input layer, an output layer and one or  
1513 more hidden layers. A NN with 1 hidden layer is classed as a ‘shallow’ NN, while NNs with  
1514 more than 1 hidden layer are classed as a ‘deep’ NN (DNN). Each layer in a NN is con-  
1515 structed from nodes, with the number of nodes in the input layer being determined by the  
1516 number of input variables, and the number of nodes in the output layer being determined  
1517 by the classification mode of the network. For binary classification, the NN will have a  
1518 single node in the output layer, while for multiclass classification there will be  $N_{\text{class}}$  nodes,  
1519 one for each class.

1520

1521 The connections between the nodes in the layers depends upon the structure of the NN. In  
1522 this Thesis, the NNs used are ‘fully-connected’, meaning each node is connected to all of  
1523 the nodes in the previous and next layer. These connections, known as *synapses*, each have

1524 a corresponding weight  $w_i$ , where  $i$  represents the index of the input node in the previous  
 1525 layer. The input to a node in a layer is given by the weighted sum of the outputs of the  
 1526 nodes in the previous layer, as follows:

$$y = \sum_i w_i x_i + b . \quad (5.3.2)$$

1527 In Equation 5.3.2,  $w_i$  represents the synaptic weight connecting the  $i$ th node in the previ-  
 1528 ous layer to the given node,  $x_i$  is the output of the  $i$ th node in the previous layer and  $b$  is  
 1529 the bias. Each layer in a NN has a defined *activation function*, which acts upon the input  
 1530 to a node to produce an output value. The hidden layers in the NNs used in this Thesis  
 1531 use a Rectified Linear Unit (ReLU) activation, which is defined as  $y(x) = \max(0, x)$ . For  
 1532 the output layer, the sigmoid activation function is used for binary classification, while the  
 1533 softmax activation function is used for the multiclass case.

1534

1535 All NNs used in this Thesis were implemented using Keras and the TensorFlow backend.

## 1536 5.4 Estimating systematic uncertainties

1537 There are two, broad classes of systematic uncertainties that need to be considered when  
 1538 performing an ATLAS analysis; *experimental* uncertainties, related to uncertainties in the  
 1539 reconstruction of the physics objects in an event, and *modelling* uncertainties, related to  
 1540 choices made in the MC simulation.

### 1541 Experimental uncertainties

1542 Uncertainties arise in the simulation and reconstruction of the physics objects described  
 1543 in Chapter 4. Experimental uncertainties can affect both the normalisation and shape of  
 1544 distributions, meaning the multiplicities of reconstructed objects passing region selections  
 1545 can vary. This Section briefly describes the experimental systematics evaluated in the  
 1546 analyses detailed in Chapters 6 and 7.

1547 **Luminosity** The integrated luminosity of the dataset is determined using van Der Meer  
 1548 scans, first described in [32] and elaborated upon for ATLAS in [33]. The luminosity un-  
 1549 certainty affects the normalisation of MC predictions, and ultimately the model-dependent  
 1550 and model-independent limits of an analysis. For the analysis detailed in Chapter 6, which  
 1551 uses data collected in 2015-2016, the luminosity uncertainty is determined to be 2.1%,  
 1552 while for the analysis detailed in Chapter 7, using the full Run-2 dataset collected between  
 1553 2015-2018, the luminosity uncertainty is determined to be 1.7%.

1554 **Jets** As previously described in Section 4.3, the energy of reconstructed jets must be  
1555 corrected to account for calorimeter non-compensation, detector acceptance and defects  
1556 and pileup. The Jet Energy Scale (JES) calibration is derived using MC simulation and  
1557 data [34], and the JES uncertainties arise from choices made when developing this calibra-  
1558 tion. The full JES uncertainty set totals around 100 nuisance parameters, while a reduced  
1559 set of JES uncertainties totalling 7-8 parameters is also provided for analyses which are  
1560 insensitive to small variations in the calibration [35].

1561 The energy of jets cannot be measured exactly, despite the corrections to the jet energy  
1562 from the JES calibration. The Jet Energy Resolution (JER) is defined as the width of the  
1563 Gaussian distribution describing the measured jet energy at the calibrated jet energy scale.  
1564 The JER is determined from both data and MC [36], with the JER uncertainty arising  
1565 from choices made when determining the JER.

1566 **Flavour-tagging** Uncertainties arise in the  $b$ -tagging calibration from experimental and  
1567 modelling sources. The flavour-tagging efficiencies are derived from the comparison of  
1568 dileptonic  $t\bar{t}$  events, and as such choices made in the generation of the  $t\bar{t}$  MC affect the  
1569 measured efficiencies.

1570 **Leptons** Uncertainties that arise in the reconstruction of leptons are related to the lep-  
1571 ton energy resolution and scale calibrations, as well as the efficiencies corresponding to  
1572 the reconstruction, identification and isolation. In this Thesis, lepton trigger efficiency  
1573 uncertainties are neglected due to the use of the  $E_T^{\text{miss}}$  triggers in the analyses detailed in  
1574 Chapters 6 and 7.

1575 **Missing transverse energy** The uncertainties on the  $E_T^{\text{miss}}$  are separated into uncer-  
1576 tainties affecting the  $E_T^{\text{miss, hard}}$  and the  $E_T^{\text{miss, soft}}$  components, as described in Section 4.4.  
1577 The uncertainties on the hard  $E_T^{\text{miss}}$  term are derived by propagating the individual energy  
1578 scale and resolution uncertainties on the physics objects in an event to the  $E_T^{\text{miss}}$ . The  
1579 energy scale and resolution of the soft  $E_T^{\text{miss}}$  term are evaluated using data and MC as  
1580 described in [37].

## 1581 **Modelling uncertainties**

1582 Numerous sources of uncertainty arise in the modelling of SM backgrounds and signal.  
1583 Typically, the dominant modelling systematics come from the specific choice of generator  
1584 used to evaluate the ME and the choice of algorithm used to model the PS. In addition,  
1585 the interference between the  $t\bar{t}$  and  $Wt$  processes is often large, as described in Section  
1586 3.2. Modelling systematics are evaluated by simulating the same physical process with two  
1587 MC production configurations, taking the difference between the nominal and variation  
1588 MC predictions as the  $1\sigma$  uncertainty. This uncertainty is then applied in the statistical

1589 analysis as a 2-sided systematic affecting the normalisation and/or shape of the nominal  
 1590 distributions of the corresponding process. A general overview of the sources of modelling  
 1591 uncertainty are described here, while specific information on the procedure used to evaluate  
 1592 the individual modelling uncertainties are given in Chapters ?? and 7.

1593 **Uncertainty calculation** As previously mentioned, modelling uncertainties are calcu-  
 1594 lated by comparing two MC predictions and taking the difference as the  $1\sigma$  variation, which  
 1595 is known as a 2-point systematic. For backgrounds which are estimated using MC-only, the  
 1596 systematic in a given analysis region is calculated using the difference of the predictions  
 1597 of the two MC samples, as shown in Equation 5.4.1. The MC sample used as a variation  
 1598 can either be a statistically-independent sample, generated in a different configuration, or  
 1599 a weight-based variation of the nominal sample, where an alternate MC weight is applied  
 1600 to the nominal MC.

$$\alpha_{\text{sys}}^{\text{process}} = \pm \left| \frac{N(\text{MC})_{\text{variation}}^{\text{process}} - N(\text{MC})_{\text{nominal}}^{\text{process}}}{N(\text{MC})_{\text{nominal}}^{\text{process}}} \right| \quad (5.4.1)$$

1601 For the analysis detailed in Chapter 6, the modelling uncertainties on the  $t\bar{t}$ ,  $Wt$  and  
 1602  $W$ +jets processes are estimated using transfer factors between the CR and SR/VR. The  
 1603 transfer factor between the CR and SR for a given process is shown in Equation 5.4.2.

$$\text{TF}_{\text{sys}}^{\text{process}} = \frac{N(\text{MC}, \text{SR})_{\text{sys}}^{\text{process}}}{N(\text{MC}, \text{CR})_{\text{sys}}^{\text{process}}} \quad (5.4.2)$$

1604 The uncertainty in the SR is then given by the difference in transfer factors estimated  
 1605 using the nominal and variation MC samples, as shown in Equation 5.4.3.

$$\alpha_{\text{sys}}^{\text{process}} = \Delta \text{TF}_{\text{sys}}^{\text{process}} = \pm \left| \frac{\text{TF}_{\text{variation}}^{\text{process}} - \text{TF}_{\text{nominal}}^{\text{process}}}{\text{TF}_{\text{nominal}}^{\text{process}}} \right| \quad (5.4.3)$$

1606 The transfer factor approach is not used in the analysis detailed in Chapter 7 as the SR  
 1607 bins each have a very different  $E_{\text{T}}^{\text{miss}}$  spectrum, while the CRs are defined using a single  
 1608  $E_{\text{T}}^{\text{miss}}$  bin, and hence the extrapolation from the single-bin CRs to SR bins is difficult to  
 1609 validate.

1610 **PDF uncertainties** The uncertainty due to the choice of the nominal PDF set was  
 1611 found to be  $\mathcal{O}(1\%)$  on the dominant backgrounds, which is far less than the dominant  
 1612 systematics and statistical uncertainties. Hence, PDF uncertainties are neglected in this  
 1613 Thesis.

1614 **Generator uncertainties** The choice of generator used to model the hard scatter is  
 1615 typically driven by the agreement between the MC predictions and data, with the generator  
 1616 which best reproduces the data across a range of phase space being deemed the nominal

1617 choice. In order to ensure the estimate of the nominal generator is robust in the analysis  
 1618 phase space, the uncertainty on the calculation of the ME is evaluated by generating an MC  
 1619 sample which uses a different generator for the hard scatter, but is interfaced to the same  
 1620 PS algorithm. Variations of the generator uncertainty are not available for all processes;  
 1621 in this Thesis, the generator uncertainties are evaluated for the top-pair, single top and  
 1622  $t\bar{t}V$  processes.

1623 **Parton showering uncertainties** Similarly to generator uncertainties, the nominal  
 1624 choice of PS algorithm is driven by the agreement between data and MC predictions.  
 1625 To estimate the impact of using a different PS algorithm, the nominal configuration is  
 1626 compared with a MC sample which is produced using the same generator for the hard  
 1627 scatter but using a different PS algorithm. Again, this is evaluated only for the top-pair,  
 1628 single top and  $t\bar{t}V$  processes.

1629 **Scale uncertainties** Numerous choices of scale are made when producing MC samples,  
 1630 such as the value of  $\alpha_S$ ,  $\mu_R$  and  $\mu_F$ . For the  $W/Z$ +jets, diboson and triboson backgrounds,  
 1631 the predictions of 7 variations of  $\mu_R$  and  $\mu_F$  are evaluated, with the values of  $\mu_R$  and  $\mu_F$   
 1632 being evaluated at  $0.5\times$ ,  $1.0\times$  and  $2.0\times$  the nominal values. The maximum downwards  
 1633 and upwards variation then define the asymmetric uncertainty on these scale choices. As  
 1634 mentioned in Section 3.2, there can be overlap between a LO with PS and NLO process,  
 1635 and hence matching and/or merging is used to remove the overlap. For the  $W/Z$ +jets  
 1636 backgrounds, the choice of scale used to perform such matching is varied from the nominal  
 1637 value of 20 GeV to 15 GeV and 30 GeV.

## 1638 5.5 Statistical analysis

1639 All statistical analyses performed in this Thesis were implemented in the HistFitter frame-  
 1640 work [38]. This framework requires an analysis structure similar to that shown in Figure  
 1641 5.1. The use of CRs in the fit allows background process yields to be corrected to data,  
 1642 such that any mismodelling of data by the MC can be minimised in the SRs.

1643

1644 Fits using this framework utilise the background CRs to make estimates of the back-  
 1645 grounds in the SR by normalising the expected number of background events from the MC  
 1646 to data. Each background with a corresponding CR, known as a *normalised* background,  
 1647 acquire a normalisation factor,  $\mu_p$ . This normalisation factor is derived by comparing the  
 1648 number of expected and observed events in a given CR for a given normalised background,  
 1649 enabling an extrapolation to the SR as shown in Equation 5.5.1.

$$N_{\text{process}}^{SR}(\text{Exp}) = \mu_p \cdot N_{\text{process}}^{SR}(\text{MC}) \quad (5.5.1)$$

1650 In Equation 5.5.1, the number of expected events in a given region for a given process,  
 1651  $N_{\text{process}}^{SR}(\text{Exp})$ , is calculated by multiplying the expected number of events for that process  
 1652 in that region from the MC,  $N_{\text{process}}^{SR}(\text{MC})$ , by the process-specific normalisation factor,  $\mu_p$ ,  
 1653 which is calculated automatically when performing the fit.

1654  
 1655 Fits are performed by constructing a likelihood function,  $L$ , depending upon the expected  
 1656 number of MC events in each CR and SR, the systematic uncertainties arising from statisti-  
 1657 cal, experimental and theoretical sources on these backgrounds, and the observed number  
 1658 of events in each CR and SR. The likelihood function used by HistFitter is shown in  
 1659 Equation 5.5.2.

$$L(n, \theta^0 | \mu_{\text{sig}}, b, \theta) = P(n_S | \lambda_S(\mu_{\text{sig}}, b, \theta)) \times \prod_{i \in CR} P(n_i | \lambda_i(\mu_{\text{sig}}, b, \theta)) \times C_{\text{syst}}(\theta^0, \theta) \quad (5.5.2)$$

1660 The likelihood function is constructed around a product of Poisson distributions of ob-  
 1661 served ( $n_S, n_i$ ) and expected ( $\lambda_S, \lambda_i$ ) events in the SR and CRs, respectively. The Poisson  
 1662 expectations,  $\lambda_S$  and  $\lambda_i$ , depend upon the background prediction,  $b$  and the corresponding  
 1663 nuisance parameters representing the systematic uncertainties,  $\theta$ , as well as the signal  
 1664 strength parameter,  $\mu_{\text{sig}}$ . The signal strength parameter can be set to 0 to remove signal  
 1665 being considered in the fit, or if considering signal can be set to 1 to include the nominal  
 1666 signal yield estimate for a signal under consideration. The systematics term,  $C_{\text{syst}}(\theta^0, \theta)$ ,  
 1667 shown in Equation 5.5.3 is defined as a product of Gaussian constraints,  $\theta_j$ , each represent-  
 1668 ing a systematic variation, which are varied around  $\theta_j^0 = 0$  when maximising the likelihood  
 1669 function.

$$C_{\text{syst}}(\theta^0, \theta) = \prod_{j \in S} G(\theta_j^0 - \theta_j) \quad (5.5.3)$$

1670 In searches for New Physics, test statistics are used to quantify the agreement between the  
 1671 expected and observed yields in a given region. Of particular interest in this Thesis are the  
 1672  $p$ -value and the  $\text{CL}_s$ . The  $p$ -value, given a hypothesis  $H_0$ , is interpreted as the probability  
 1673 that the alternate hypothesis,  $H_1$ , can provide a result at least as incompatible with  $H_0$  as  
 1674 the observed result. The definition of the  $p$ -value is given in Equation 5.5.4.

$$p = \int_{t_{\text{obs}}}^{+\infty} g(t|H_0) dt \quad (5.5.4)$$

1675 In Equation 5.5.4,  $g(t|H_0)$  is the probability density of the test statistic,  $t$ , under the as-  
 1676 sumption of the hypothesis,  $H_0$ . In the event of a discrepancy between the expected and  
 1677 observed results, it is desirable to be able to quantify the size of a discrepancy, which is  
 1678 done using the significance,  $Z$ . This significance is defined such that a result which is  $Z$   
 1679 standard deviations from the mean of a Gaussian distribution has an integral equal to the  
 1680  $p$ -value.

1681

1682 The test statistic used for the purposes of setting limits on New Physics signals is the  
1683 profile log likelihood ratio, shown in Equation 5.5.5.

$$t_{\mu_{\text{sig}}} = -2\log\left(\frac{L(\mu_{\text{sig}}, \theta)}{L(\mu_{\text{sig}}, \hat{\theta})}\right) \quad (5.5.5)$$

1684

In Equation 5.5.5,  $L$  is the likelihood function defined in Equation 5.5.2, where the denomi-  
1685 nator has parameter choices such that the likelihood is maximised, while the numerator has  
1686 parameter choices that maximise the likelihood for the specific signal hypothesis under test.

1687

1688 In the context of searches for New Physics, the  $p$ -value can be used to claim a discov-  
1689 ery of New Physics, or exclude a given signal hypothesis. To claim the discovery of New  
1690 Physics, one must reject the hypothesis that only the SM background contributes to the  
1691 observed result to a level of  $Z = 5\sigma$ , corresponding to  $p < 2.87 \times 10^{-7}$ . The requirements  
1692 to exclude a signal hypothesis are less stringent, requiring the rejection of the SM back-  
1693 ground plus BSM signal hypothesis with values of  $p < 0.05$ , corresponding to  $Z = 1.64$ .  
1694 This exclusion limit correspondes to a 95% confidence limit.

1695

1696 One issue with using the  $p$ -value as the metric by which exclusion is performed is the  
1697 case where the rates of the BSM process are small enough such that the SM-only and  
1698 SM plus BSM signal distributions are very similar. In the case where an analysis has low  
1699 sensivity to a particular signal hypothesis, or where there is a downwards fluctuation of  
1700 data, the signal hypothesis can be rejected. To circumvent this, the  $CL_s$  method [39] was  
1701 developed, where the  $CL_s$  is defined as shown in Equation 5.5.6.

$$CL_s = \frac{p_1}{1 - p_0} = \frac{\int_{t_{\text{obs}}}^{+\infty} g(t|H_1)dt}{1 - \int_0^{t_{\text{obs}}} g(t|H_0)dt} \quad (5.5.6)$$

1702

In Equation 5.5.6,  $p_1$  corresponds to the  $p$ -value that the alternate hypothesis,  $H_1$ , is at  
1703 least as incompatible with  $H_0$  as the observed result, while  $p_0$  corresponds to the  $p$ -value  
1704 that the observed result is compatible with the null hypothesis,  $H_0$ .

1705

### Background-only fit

1706

The background-only fit is independent of any signal model assumptions, including only  
1707 SM background MC in the fit. In this scenario,  $\mu_{\text{sig}}$  is set equal to 0. This fit type includes  
1708 only the CRs in the fit, and hence is not affected by the observed events in the SRs. The  
1709 purpose of this fit is to estimate the background yields in the SRs and VRs in a signal-  
1710 agnostic way, under the assumption that the CRs have negligible signal contamination.  
1711 Additionally, the results of the background-only fit can be used to test the sensitivity of a

1712 given analysis to a different signal than the one under study using the  $p$ -value hypothesis  
1713 test previously described.

### 1714 **Model-dependent fit**

1715 The model-dependent fit regime includes background events and a specific signal model,  
1716 fitting all processes together in both the CRs and SRs, including a signal strength param-  
1717 eter  $\mu_{\text{sig}}$ . The signal is included in *all* regions, to allow any signal contamination in the  
1718 CRs to be correctly accounted for when calculating the background normalisation factors,  
1719  $\mu_p$ . The model-dependent fit is performed on every signal point generated, such that the  
1720 entire phase space of signal parameters is probed.

### 1721 **Model-independent fit**

1722 The model-independent fit is used to set limits on any potential BSM process present in  
1723 the SRs. This fit includes both the CRs and SRs, but does not include a signal model or  
1724 allow signal contamination in the CRs. In this fit regime, the SRs are implemented as an  
1725 inclusive, single-bin region. The result of this fit is used to set upper limits on the visible  
1726 cross-section,  $\sigma_{\text{vis}}$ , of a generic BSM process.

1727

## Part II

1728

# Searches for New Physics in Run-2

1729

## ATLAS data

## Chapter 6

# Searches for $\tilde{\chi}_1^\pm \tilde{\chi}_2^0$ pair-production

This Chapter presents an overview of searches for the pair-production of a chargino,  $\tilde{\chi}_1^\pm$  and next-to-lightest neutralino,  $\tilde{\chi}_2^0$ , performed during the Run-2 period of data-taking. This Chapter focuses mainly on an analysis undertaken using data taken in 2015-2016, totalling  $36.1\text{fb}^{-1}$ . Later in this Chapter, the results of an analysis using the full Run-2 dataset of  $139\text{fb}^{-1}$  is presented, along with additional studies using machine learning to improve the sensitivity to the signal. Chapter 8 presents sensitivity studies for this signal at the High-Luminosity LHC, using a dataset of  $3000\text{fb}^{-1}$  collected at  $\sqrt{s} = 14$  TeV. The results of these analyses are interpreted in the context of a simplified SUSY model **INSERT REF**, in which the  $\tilde{\chi}_1^\pm$  and  $\tilde{\chi}_2^0$  are unstable and each decay to the lightest neutralino,  $\tilde{\chi}_1^0$ , via a SM  $W$  boson and Higgs boson.

This Chapter focuses on the  $Wh$  signature, where  $h$  is the lightest Higgs coming from the extended Higgs sector, and is identified with the SM Higgs boson, and hence has  $m_h = 125$  GeV and the same couplings as the SM Higgs. The final state of interest in this Chapter, and in Chapter 8, contains a single electron or muon from the decay of the  $W$  boson, two  $b$ -tagged jets from the decay of the Higgs boson, and  $E_T^{\text{miss}}$  from the neutrino and the two  $\tilde{\chi}_1^0$ . The  $h \rightarrow b\bar{b}$  decay is the most frequent decay of the Higgs boson, with a branching fraction of 58%, and therefore this channel is expected to have far higher signal yields than channels targeting other decay modes of  $h$ . A diagram of the signal process relevant for this Chapter is shown in Figure 6.1.

A search for this process was undertaken in Run 1 using  $20.3\text{fb}^{-1}$  taken at  $\sqrt{s} = 8$  TeV in this final state, as well as the dilepton, trilepton and diphoton final states. 95% confidence limits were set on this signal, excluding the process upto  $\tilde{\chi}_1^\pm/\tilde{\chi}_2^0$  masses of around 275 GeV for a massless  $\tilde{\chi}_1^0$ . The results for all four channels, as well as the statistical combination, are shown in Figure 6.2.

This Chapter first describes the simplified SUSY model used in both this Chapter and

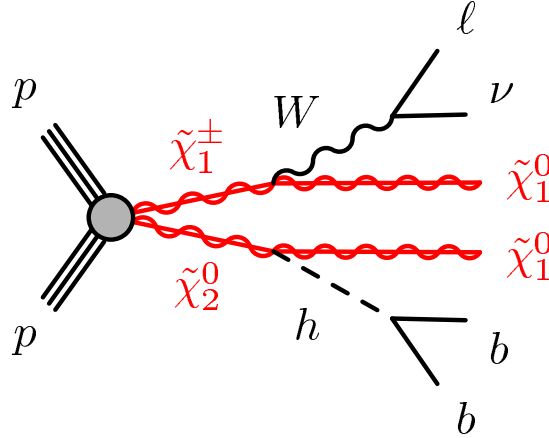


Figure 6.1: Diagram showing  $\tilde{\chi}_1^\pm \tilde{\chi}_2^0$  pair-production, with the chargino and neutralino decaying via a SM  $W$  boson and a Higgs, respectively. The assumptions made in simplified SUSY model are summarised in Table 6.1.

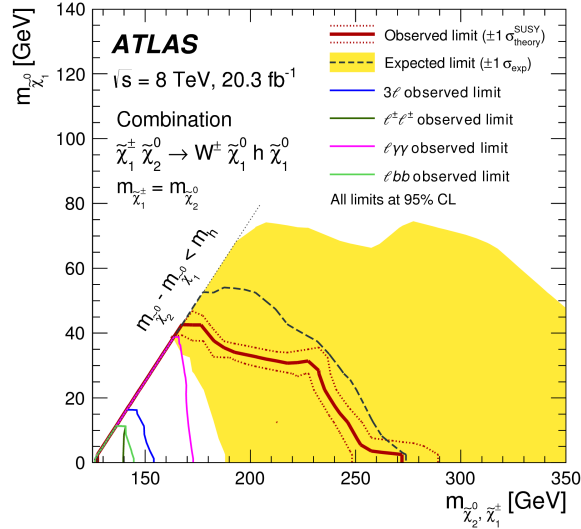


Figure 6.2: A plot showing the four exclusion limits obtained from searches for  $\tilde{\chi}_1^\pm \tilde{\chi}_2^0$  pair-production during the Run-1 data-taking period.

1760 in Chapter ???. The event selection used to describe candidate SUSY events is then de-  
 1761 scribed, followed by the background estimation strategy, before presenting the results of  
 1762 this analysis.

## 1763 6.1 SUSY signal model

1764 As discussed in Chapter 1, SUSY provides resolution to the hierarchy problem through  
 1765 the introduction of fermionic (bosonic) superpartners to the SM bosons (fermions). As  
 1766 of the time of writing, there has been no experimental observation of these superpartners  
 1767 and hence it is concluded SUSY is a broken symmetry, such that the superpartners have

1768 different masses to their SM partners. If the masses of the squarks and gluinos, the super-  
 1769 partners to the SM quarks and gluon, are much heavier than charginos and neutralinos, the  
 1770 electroweak production of SUSY particles is expected to dominate at the LHC. The mass  
 1771 eigenstates of the charginos,  $\tilde{\chi}_i^\pm$  where  $i = 1, 2$ , and neutralinos,  $\tilde{\chi}_j^0$  where  $j = 1, 2, 3, 4$ , are  
 1772 ordered from smallest to largest mass. In this Thesis, the lightest supersymmetric particle  
 1773 (LSP) corresponds to the lightest neutralino,  $\tilde{\chi}_1^0$ , and is a DM candidate in the case where  
 1774 R-parity is conserved, meaning the LSP is stable and weakly-interacting.

1775

1776 SUSY models have an enormous parameter space with over 100 free parameters, such  
 1777 as the sparticle masses and couplings. Simplified models vastly reduce the number of free  
 1778 parameters, such that a single analysis can be sensitive to a large region of the SUSY model  
 1779 phase space. As previously mentioned, it is assumed the Higgs boson present in the decay  
 1780 of the  $\tilde{\chi}_2^0$  is SM-like, such that it has a mass of  $m_h = 125$  GeV and  $\text{BR}(h \rightarrow b\bar{b}) = 0.58$ .  
 1781 It is assumed that the branching ratios of the  $\tilde{\chi}_1^\pm \rightarrow W\tilde{\chi}_1^0$  and  $\tilde{\chi}_2^0 \rightarrow h\tilde{\chi}_1^0$  are both 100%.  
 1782 Therefore, the only free parameters of the simplified model used in both this Chapter and  
 1783 Chapter 8 are  $m(\tilde{\chi}_1^\pm)$ ,  $m(\tilde{\chi}_2^0)$  and  $m(\tilde{\chi}_1^0)$ . The further assumption that the  $\tilde{\chi}_1^\pm$  and  $\tilde{\chi}_2^0$   
 1784 and degenerate in mass reduces the number of free parameters to just two;  $m(\tilde{\chi}_1^\pm/\tilde{\chi}_2^0)$  and  
 1785  $m(\tilde{\chi}_1^0)$ . The simplified model assumptions are listed again for reference in Table 6.1.

Model parameter	Assumption
$\text{BR}(\tilde{\chi}_1^\pm \rightarrow W\tilde{\chi}_1^0)$	100%
$\text{BR}(\tilde{\chi}_2^0 \rightarrow h\tilde{\chi}_1^0)$	100%
$\text{BR}(h \rightarrow b\bar{b})$	58%
$m_h$	125 GeV
Sparticle masses	$m(\tilde{\chi}_1^\pm) = m(\tilde{\chi}_2^0)$

Table 6.1: A table summarising the model parameter assumptions for the simplified SUSY model used in this Chapter and Chapter 8.

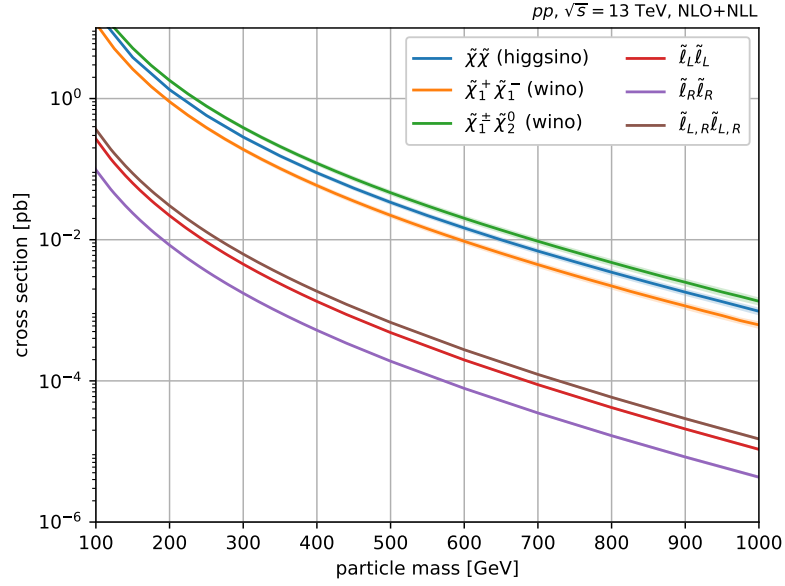


Figure 6.3

## 1786 6.2 Event selection

1787 Candidate events for this analyses are first selected using a set of loose, preliminary se-  
 1788 lections, known as ‘preselection’. The preselection cuts, summarised in Table 6.2, target  
 1789 events with an event topology which matches that of the signal, in particular events with  
 1790 a single lepton, two  $b$ -jets and  $E_T^{\text{miss}}$ . All events are required to have exactly 1 electron or  
 1791 muon passing the signal lepton requirements, with any extra baseline leptons being vetoed.  
 1792 Events are required to have either 2 or 3 jets with transverse momentum greater than 25  
 1793 GeV, and exactly two jets being  $b$ -tagged using the MV2c10 algorithm. The  $b$ -tagged jets  
 1794 are also required to have transverse momentum greater than 25 GeV. Some data/MC dis-  
 1795 crepancies were seen at low  $m_{bb}$  and  $m_T$ , and hence lower bound requirements on these  
 1796 variables are placed. Finally, all events are required to pass one of the  $E_T^{\text{miss}}$  triggers  
 1797 detailed in Section 3.1.

## 1798 6.3 Background estimation

1799 The  $t\bar{t}$ , single top and  $W$ +jets backgrounds are the most dominant backgrounds in the three  
 1800 SR bins. Each of these major backgrounds have corresponding CRs defined in which to  
 1801 evaluate the process-specific normalisations,  $\mu_{\text{process}}$ . The  $t\bar{t}$  CR is defined with 3  $m_T$  bins,  
 1802 matching the  $m_T$  ranges of the 3 SR bins, named CR( $t\bar{t}$ )-LM, CR( $t\bar{t}$ )-MM and CR( $t\bar{t}$ )-  
 1803 HM, respectively. The top-pair CRs invert the selection on the  $m_{CT}$  variable described in  
 1804 Chapter 5 to target the production of a pair of top quarks, while the selection on  $m_{bb}$  is  
 1805 inverted as the distribution is not expected to peak around the Higgs masses. A single-bin

Variable	Selection
$N_\ell^{\text{baseline}}$	= 1
$N_\ell^{\text{signal}}$	= 1
$p_T(\ell_1)$	> 27 GeV
$N_{\text{jet}}$	= 2 or 3
$p_T(\text{jet})$	> 25 GeV
$N_{b\text{-jet}}$	= 2
$p_T(b\text{-jet})$	> 25 GeV
$m_T$	> 40 GeV
$m_{bb}$	> 50 GeV

Table 6.2: A summary of the preliminary event selection used in the  $36.1\text{fb}^{-1}$  search for  $\tilde{\chi}_1^\pm \tilde{\chi}_2^0$  pair-production.

	SRLM	SRMM	SRHM
$m_{bb}$	$\in [105, 135]$ GeV		
$m_{CT}$	> 160 GeV		
$E_T^{\text{miss}}$	> 200 GeV		
$m_T$	$\in [100, 140]$ GeV	$\in [140, 200]$ GeV	> 200 GeV

Table 6.3: A summary of the signal region selections used in the  $36.1\text{fb}^{-1}$  search for  $\tilde{\chi}_1^\pm \tilde{\chi}_2^0$  pair-production.

1806 CR for the single top background,  $\text{CR}(t)$ , and a single-bin CR for the  $W$ +jets background,  
 1807  $\text{CR}(W)$ , are also defined. The single-top CR is defined by requiring the  $m_{bb}$  is large to  
 1808 target the presence of  $b$ -quarks coming from the decay of a top quark and the initial state  
 1809 gluon splitting. Finally, the  $W$ +jets CR exploits the  $m_T$  variable, as described in Chapter  
 1810 5, to target the decay of a single leptonic  $W$  boson, while rejecting the  $t\bar{t}$  background. The  
 1811 full definitions of these regions are given in Table 6.4.

Variable	Region				
	$\text{CR}(t\bar{t}\text{-LM})$	$\text{CR}(t\bar{t}\text{-MM})$	$\text{CR}(t\bar{t}\text{-HM})$	$\text{CR}(t)$	$\text{CR}(W)$
$m_T$ [GeV]	$\in [100, 140]$	$\in [140, 200]$	> 200	> 100	$\in [40, 100]$
$m_{CT}$ [GeV]	< 160	< 160	< 160	> 160	> 160
$m_{bb}$ [GeV]	$\notin [105, 135]$	$\notin [105, 135]$	$\notin [105, 135]$	> 195	< 80
$E_T^{\text{miss}}$ [GeV]	> 200	> 200	> 200	> 200	> 200

Table 6.4

1812 6 VRs are defined, 3 targeting  $m_{bb}$  values in a window around the Higgs peak,  $m_{bb} \in$   
 1813  $[105, 135]$  GeV, with 3 further VRs targeting  $m_{bb}$  values in the sideband region. The

1814 former VRs are referred to as ‘on-peak’ regions, denoted by  $\text{VR}_{\text{on}}$ , while the latter are  
 1815 referred to as ‘off-peak’ regions and are denoted by  $\text{VR}_{\text{off}}$ . Each set of VRs mirrors the SR  
 binning in the  $m_T$  variable. The explicit VR definitions are given in Table 6.5.

Variable	Region					
	$\text{VR}_{\text{on}}(\text{LM})$	$\text{VR}_{\text{on}}(\text{MM})$	$\text{VR}_{\text{on}}(\text{HM})$	$\text{VR}_{\text{off}}(\text{LM})$	$\text{VR}_{\text{off}}(\text{MM})$	$\text{VR}_{\text{off}}(\text{HM})$
$m_T$ [GeV]	$\in [100, 140]$	$\in [140, 200]$	$> 200$	$\in [100, 140]$	$\in [140, 200]$	$> 200$
$m_{\text{CT}}$ [GeV]	$< 160$	$< 160$	$< 160$	$> 160$	$> 160$	$> 160$
$m_{\text{bb}}$ [GeV]	$\in [105, 135]$	$\in [105, 135]$	$\in [105, 135]$	$< 95 \parallel \in [145, 195]$		
$E_T^{\text{miss}}$ [GeV]	$> 200$	$> 200$	$> 200$	$> 180$	$> 180$	$> 180$

Table 6.5

1816

## 1817 6.4 Systematic uncertainties

1818 Three sources of uncertainty are considered in this analysis; statistical uncertainties, arising  
 1819 from the finite statistics in both data and the MC, experimental systematics and modelling  
 1820 systematics. Section 5.4 describes the experimental systematics evaluated in this analysis.  
 1821 Modelling uncertainties are evaluated using the transfer factor prescription described in  
 Section **REF**.

Source	Size (%)
	Modelling systematics
$t\bar{t}$ modelling	
Single top modelling	
	Experimental systematics
JES	
JER	
$b$ -tagging	

Table 6.6: Table showing a summary of the dominant experimental and modelling uncertainties.

1822

## 1823 6.5 Results

### 1824 Background-only fit results

1825 The results of the background-only fit in the CRs, VRs and SRs for the  $1\ell + b\bar{b} + E_T^{\text{miss}}$  channel  
 1826 are shown in Tables 6.7, **REF** and 6.8, respectively. As explained in Chapter 5.5, the

1827 background-only fit configuration uses only the CRs to normalise the dominant back-  
 1828 grounds, in this case  $t\bar{t}$ , single top and  $W$ +jets. The  $t\bar{t}$  background has 3 separate nor-  
 1829 malisation factors, one for each  $m_T$  bin, such that data/MC differences in each region can  
 1830 be corrected independently of each other. The results of the background-only fit are then  
 1831 extrapolated to the VRs and SRs, such that an estimate of the backgrounds in the SR  
 1832 can be derived without bias from any potential excesses in the SRs, or assumptions on the  
 1833 signal model itself. Excellent data/MC agreement is observed in the CRs and most of the  
 1834 VRs. In  $VR_{\text{on-HM}}$  and  $SR_{\text{MM}}$ , there are excesses between  $1.5 - 2\sigma$ .

1835

1836 The normalisation factors derived for the  $t\bar{t}$ , single top and  $W$ +jets backgrounds using  
 1837 the background-only fit configuration are given in Table 6.9. All values are compatible  
 with unity, with the

<b>Control regions</b>	CR( $t\bar{t}$ )-LM	CR( $t\bar{t}$ )-MM	CR( $t\bar{t}$ )-HM	CR( $W$ )	CR( $t$ )
Observed events	192	359	1115	72	65
Fitted bkg events	$192 \pm 14$	$359 \pm 19$	$1115 \pm 34$	$72 \pm 9$	$65 \pm 8$
$t\bar{t}$	$147 \pm 33$	$325 \pm 32$	$1020 \pm 90$	$15 \pm 14$	$20^{+23}_{-20}$
Single top	$28 \pm 25$	$22^{+24}_{-22}$	$60^{+70}_{-60}$	$4^{+6}_{-4}$	$33 \pm 25$
$W$ +jets	$16 \pm 7$	$7.3 \pm 2.7$	$25 \pm 11$	$51 \pm 17$	$8 \pm 4$
$t\bar{t}V$	$1.16 \pm 0.20$	$2.8 \pm 0.4$	$6.9 \pm 1.1$	$0.079 \pm 0.022$	$3.2 \pm 0.6$
Diboson	$0.57 \pm 0.24$	$0.92 \pm 0.29$	$1.3 \pm 0.4$	$2.1 \pm 1.1$	$0.84 \pm 0.28$
Others	$0.125 \pm 0.032$	$0.20 \pm 0.06$	$1.9 \pm 0.5$	$0.24 \pm 0.17$	$0.10 \pm 0.04$

Table 6.7

1838

<b>Signal regions</b>	SRLM	SRMM	SRHM
Observed events	6	7	5
Fitted bkg events	$5.7 \pm 2.3$	$2.8 \pm 1.0$	$4.6 \pm 1.2$
$t\bar{t}$	$3.4 \pm 2.9$	$1.4 \pm 1.0$	$1.1 \pm 0.6$
Single top (Wt)	$1.4_{-1.4}^{+1.4}$	$0.8_{-0.8}^{+0.9}$	$1.2 \pm 1.1$
W + jets	$0.6 \pm 0.4$	$0.20 \pm 0.11$	$1.6 \pm 0.6$
$t\bar{t}V$	$0.10 \pm 0.04$	$0.32 \pm 0.09$	$0.54 \pm 0.14$
Diboson	$0.12_{-0.12}^{+0.15}$	$0.05 \pm 0.03$	$0.08 \pm 0.02$
Others	$0.10 \pm 0.05$	$0.03 \pm 0.01$	$0.04 \pm 0.02$

Table 6.8

1 $\ell$ analysis	
$\mu(t\bar{t}\text{-LM})$	<b><math>1.02 \pm 0.14</math></b>
$\mu(t\bar{t}\text{-MM})$	$1.15 \pm 0.13$
$\mu(t\bar{t}\text{-HM})$	$0.89_{-0.20}^{+0.21}$
$\mu(W)$	$1.40 \pm 0.5$
$\mu(t)$	$1.10_{-1.1}^{+0.7}$

Table 6.9

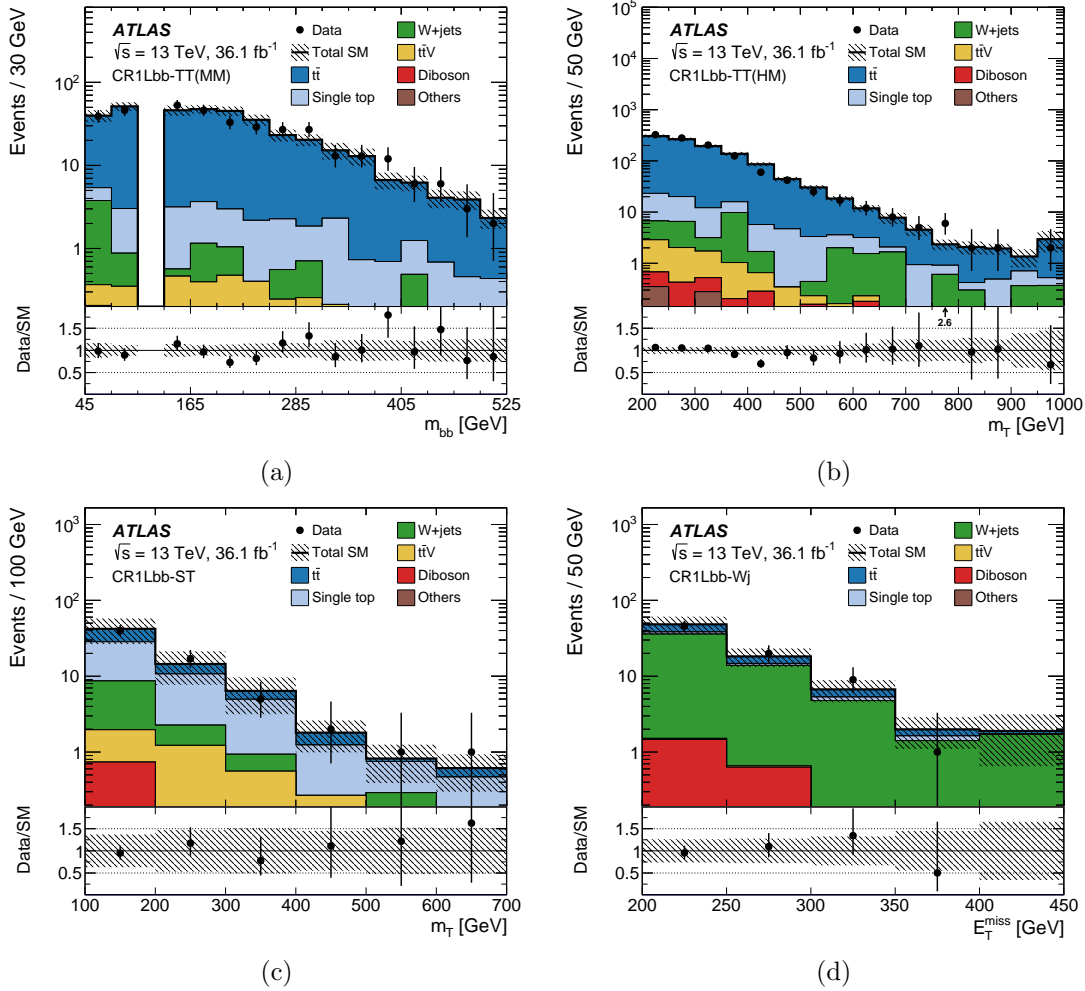


Figure 6.4

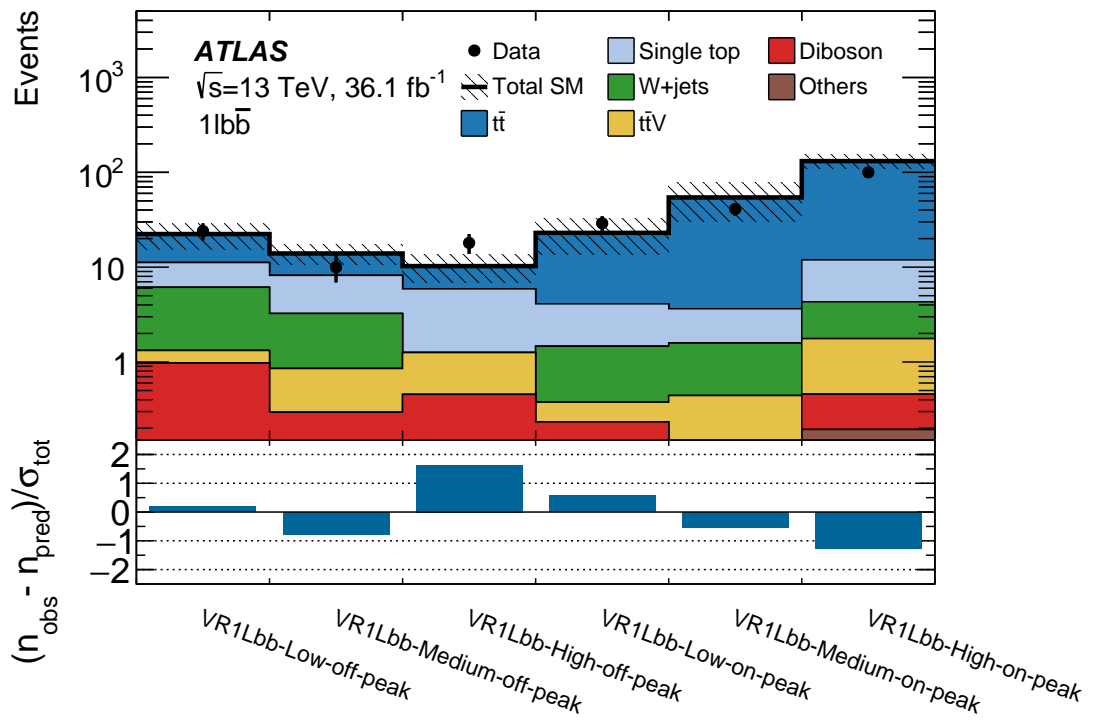


Figure 6.5

1839 **Model-dependent results**

1840 As shown in the background-only fit results presented previously, no significant excesses are  
 1841 observed in the SRs. In this case, model-dependent exclusion limits are set on  $\tilde{\chi}_1^\pm \tilde{\chi}_2^0$  pair-  
 1842 production decaying via the  $Wh$  signature to the  $1\ell + b\bar{b} + E_T^{\text{miss}}$  final state. As described in  
 1843 Section 5.5, the model-dependent fit configuration uses both the CRs and SRs to set 95%  
 1844 confidence limits on the presence of a given signal model. The model-dependent exclusion  
 1845 limits for the analysis using a dataset of  $36.1\text{fb}^{-1}$  collected at  $\sqrt{s} = 13$  TeV is shown in  
 Figure 6.6, excluding  $\tilde{\chi}_1^\pm/\tilde{\chi}_2^0$  masses upto 550 GeV for a massless  $\tilde{\chi}_1^0$ .

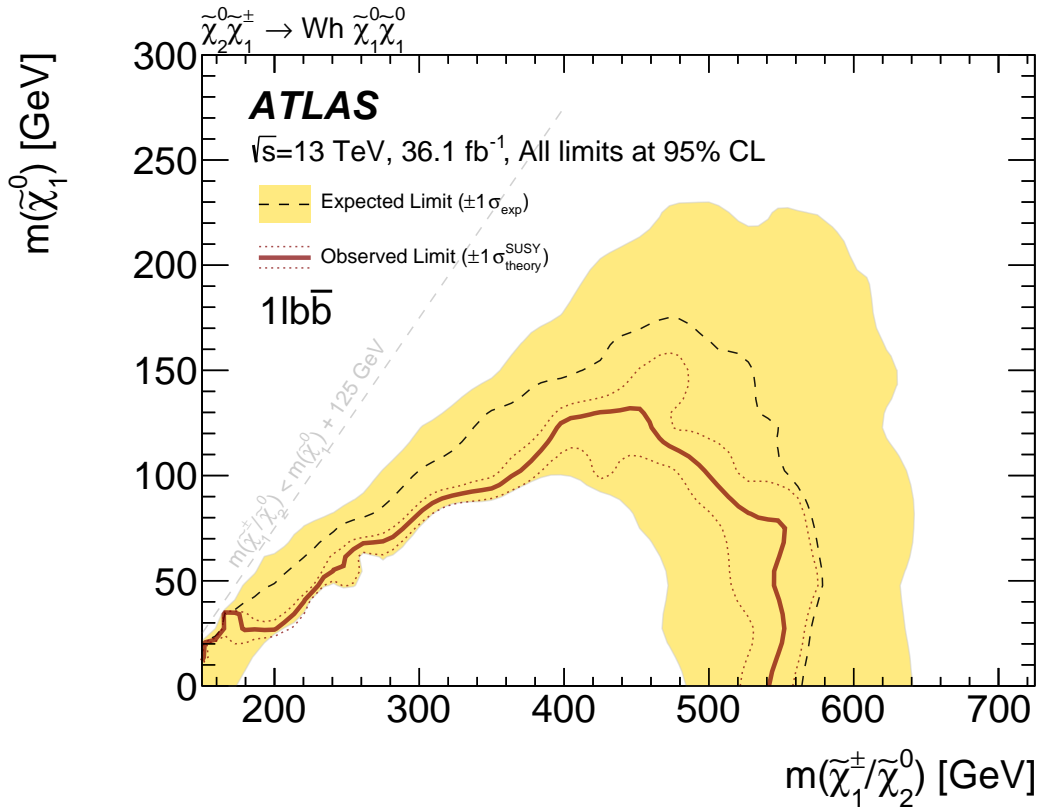


Figure 6.6

1846

1847 **Model-independent limits**

1848 In addition to the model-dependent fit, 95% confidence limits are set on a generic BSM  
 1849 process using the model-independent fit strategy detailed in Section ???. A visible cross-  
 1850 section,  $\sigma_{\text{vis}}$ , is derived which represents the product of the signal selection efficiency,  $\epsilon$ , the  
 1851 detector acceptance,  $A$  and the production cross-section for the BSM process,  $\sigma_{\text{BSM}}$ . The  
 1852 model-independent limits on  $\sigma_{\text{vis}}$  derived using the SRs defined early are shown in Table  
 1853 6.10, as well as limits on the expected and observed number of signal events.

	$\sigma_{\text{vis}}$ [fb]	$S_{\text{obs}}^{95}$	$S_{\text{exp}}^{95}$	$p_0$ -value
SRLM	0.23	8.3	$8.0_{-2.2}^{+3.3}$	0.46
SRMM	0.28	10.0	$5.6_{-1.7}^{+2.9}$	0.04
SRHM	0.18	6.4	$6.1_{-1.9}^{+3.1}$	0.44

Table 6.10: From left to right, the observed 95% CL upper limits on the visible cross-sections  $\sigma_{\text{vis}}$ , the observed ( $S_{\text{obs}}^{95}$ ) and expected ( $S_{\text{exp}}^{95}$ ) 95% CL upper limits on the number of signal events with  $\pm 1\sigma$  excursions of the expectation, and the discovery  $p$ -value ( $p_0$ ), truncated at 0.5.

## 1854 **6.6 Studies with $139\text{fb}^{-1}$**

### 1855 **ML studies**

### 1856 **Reoptimised analysis results**

## Chapter 7

# Search for Dark Matter produced in association with a Top Quark

This Chapter presents a search for the production of Dark Matter (DM) in association with a single top quark, also referred to as  $DMt$ , using the full Run-2 dataset collected by ATLAS of  $139\text{fb}^{-1}$ . The results of the analysis are interpreted in the context of a simplified model of DM production, where the DM is coupled to an extended SM Higgs sector (2HDM) by a massive, spin-0, pseudoscalar mediator,  $a$ .

This Chapter focuses mainly on the  $tW+E_T^{\text{miss}}$  signature with a single lepton final state. A complementary analysis of the two lepton final state was also performed, as documented in [40], and will not be detailed here. In addition to the  $tW+E_T^{\text{miss}}$  signature, it was found that the sensitivity of these analyses to DM produced in association with a  $t\bar{t}$  pair, referred to as  $DMt\bar{t}$ , was non-negligible. The overall sensitivity of this analysis to the  $DMt+t\bar{t}$  signal was evaluated and is detailed in the fit results. Finally, in addition to the independent analyses of the single- and two-lepton final states, both channels were statistically-combined to increase the sensitivity to the  $DMt$  and  $DMt+t\bar{t}$  signals.

This Chapter begins with a description of the simplified DM model used to interpret the results, focusing on the experimental signature of interest, the  $tW+E_T^{\text{miss}}$  signature. The SR optimisation and selections, as well as the background estimation strategy are documented, before finally presenting the analysis results. Firstly, the background-only fit results in the CRs and SRs are presented, before presenting the model-dependent and model-independent results.

### 7.1 2HDM+ $a$ signal model

As described in Section ??, there is a strong motivation for performing searches for the production of Dark Matter (DM) at the LHC. Many searches for DM production have already

1884 been carried out using ATLAS data, with the results of the searches being interpreted  
 1885 in the context of the LHC DM simplified models, as described in [41–43]. These models  
 1886 introduce a new, spin-0 pseudoscalar mediator which couples the SM to DM. However,  
 1887 such models have a limited phenomenology [44], and examples of these models violating  
 1888 gauge invariance and unitarity have also studied [45]. Therefore, while the DM simplified  
 1889 models serve as an excellent benchmark in searches for DM production, a more complete  
 1890 and theoretically-consistent description of DM production is needed.

1891

1892 The simplest extension to the LHC DM simplified models adds a second Higgs doublet  
 1893 to the SM (2HDM). This enables the mixing of the spin-0 mediator with the SM, while  
 1894 also not violating constraints set on the SM Higgs couplings. The particular model of  
 1895 interest in this thesis is the case of a 2HDM model, with an additional pseudoscalar medi-  
 1896 ator,  $a$ . For this model, the  $tW + E_T^{\text{miss}}$  signature has not been previously studied, but has  
 1897 been shown to have promising potential in sensitivity studies [44]. The dominant Feynman  
 1898 diagrams for this signature are shown in Figure 7.1. The diagram shown in Figure 7.1a  
 1899 is present in the LHC DM simplified models, while the diagram shown in Figure 7.1b is  
 1900 only present in the 2HDM+ $a$  model. The latter diagram gives an approximate order-of-  
 1901 magnitude enhancement to the  $pp \rightarrow tW\chi\chi$  cross-section through the on-shell production  
 1902 of the charged Higgs,  $H^-$ . The additional diagrams from the 2HDM+ $a$  model also interfere  
 1903 destructively with the diagrams from the LHC DM simplified model, restoring unitarity.

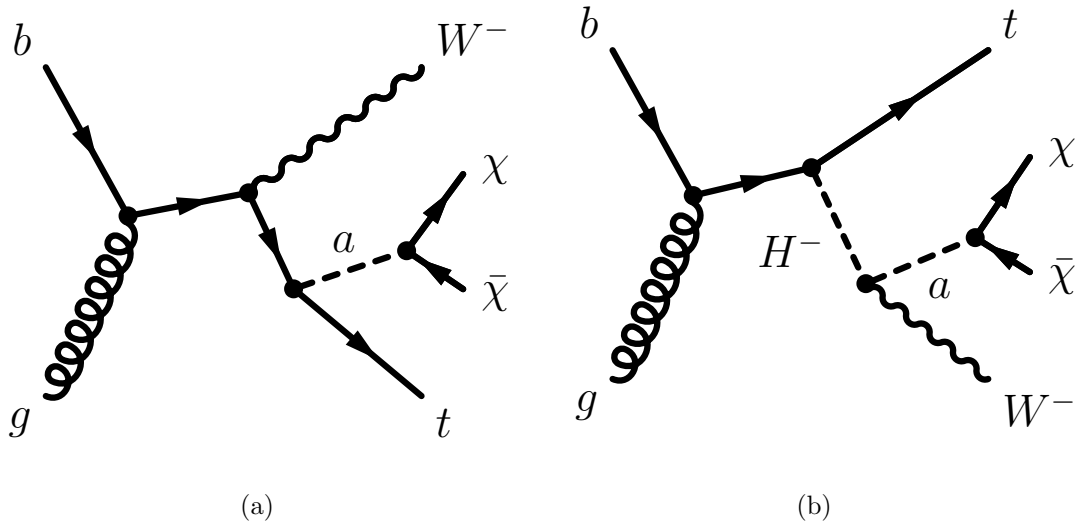


Figure 7.1: Feynman diagram for dark matter production in the  $Wt$  channel, in the context of a 2HDM+ $a$  model. This chapter documents studies done in the single lepton channel, where one of the  $W$  bosons in the event decays leptonically.

1904

In addition to the  $tW + E_T^{\text{miss}}$  signature, the analysis described in the later sections of  
 1905 this Chapter is also sensitive to the  $t\bar{t} + E_T^{\text{miss}}$  signature of associated DM production. A  
 1906 rescaling procedure is applied to the  $DMt\bar{t}$  process, which is generated, using the DMSimp

1907 framework [46], in the context of a simplified DM production model in which the pseu-  
 1908 doscalar mediator  $a$  directly couples to the SM. The Feynman diagram for this process  
 1909 is shown in Figure 7.2. The predictions of this simplified model are rescaled to correctly  
 1910 model the prediction using the 2HDM+ $a$  model using the procedure described in [47],  
 1911 which also includes contributions from the heavy pseudoscalar  $A$ .

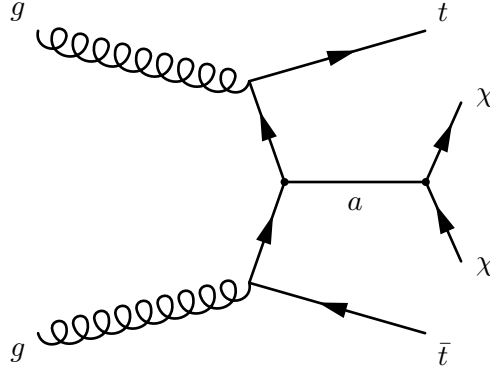


Figure 7.2: Diagram of DM produced in association with a  $t\bar{t}$  pair, in the context of the 2HDM+ $a$  model under study in this Chapter. The sensitivity of the analysis described later in this Chapter to this signal is shown in Section 7.5.

1912 The model under study in this Chapter is described in detail in [47], but an overview  
 1913 of the most prominent parameters and the choices assigned is given here. As previously  
 1914 described in Section ??, models with a second Higgs doublet comprise five physical states;  
 1915 the CP-even scalars  $h$  and  $H$ , the CP-odd pseudoscalar  $A$ , and two charged Higgs bosons  
 1916  $H^\pm$ . The coupling of the extended Higgs sector is of Type-II, such that one Higgs doublet  
 1917 couples to up-type fermions while the other couples to down-type fermions. The mixing in  
 1918 the extended Higgs sector is specified by three mixing angles,  $\alpha$ ,  $\theta$  and  $\beta$ .  $\alpha$  represents the  
 1919 mixing angle of the two CP-even states,  $\theta$  represents the mixing of the CP-odd states, and  
 1920  $\tan\beta$  represents the ratio of the VEVs of the two Higgs doublets. The *alignment limit* is  
 1921 assumed, where  $\cos(\beta - \alpha) = 0$ , such that  $h$  can be identified with the SM Higgs boson. To  
 1922 enhance the sensitivity to this model, it is assumed that there is maximal mixing between  
 1923 the Higgs sector and the mediator,  $A$  and  $a$ , and as such it is assumed that  $\sin\theta = 1/\sqrt{2}$ .  
 1924 As described in [47], it is assumed the masses of the CP-even neutral Higgs, the CP-odd  
 1925 Higgs and the charged Higgs states are degenerate, and the mass of the DM,  $m_\chi$  is set  
 1926 equal to 10 GeV. Finally, the DM coupling to  $a$  is set equal to unity,  $y_\chi = 1$ . Therefore,  
 1927 there are three free parameters;  $\tan\beta$ ,  $m_{H^\pm}$  and  $m_a$ . In order to set model-dependent  
 1928 limits on this process, two planes are defined to cover the largest possible region of the  
 1929 available model phase space. The first is a scan in the  $m_a, m_{H^\pm}$  plane, assuming  $\tan\beta = 1$ ,  
 1930 while the second plane is a scan in the  $m_{H^\pm}, \tan\beta$  plane, assuming  $m_a = 250$  GeV. The  
 1931 cross-section dependence on  $\tan\beta$  for the DM $t$  and DM $t\bar{t}$  processes is shown in Figure 7.3,  
 1932 with  $m_a = 250$  GeV and  $m_{H^\pm} = 600$  GeV. As seen, the cross-section for the DM $t\bar{t}$  process  
 1933 has a  $1/\tan^2\beta$  dependence, while the DM $t$  has a more complex dependence on the value of

1934  $\tan\beta$ . A summary of the model parameter choices is given in Table 7.1.

Fixed parameters	Assumption
$\sin\theta$	$= 1/\sqrt{2}$
$\cos(\beta - \alpha)$	$= 0$
$m_h$	$= 125$ GeV
$m_H, m_A, m_{H\pm}$	Degenerate
$m_\chi$	$= 10$ GeV
$y_\chi$	$= 1$

Table 7.1: A table summarising the model parameter assumptions for the simplified 2HDM+ $a$  model of DM production as described in [47].

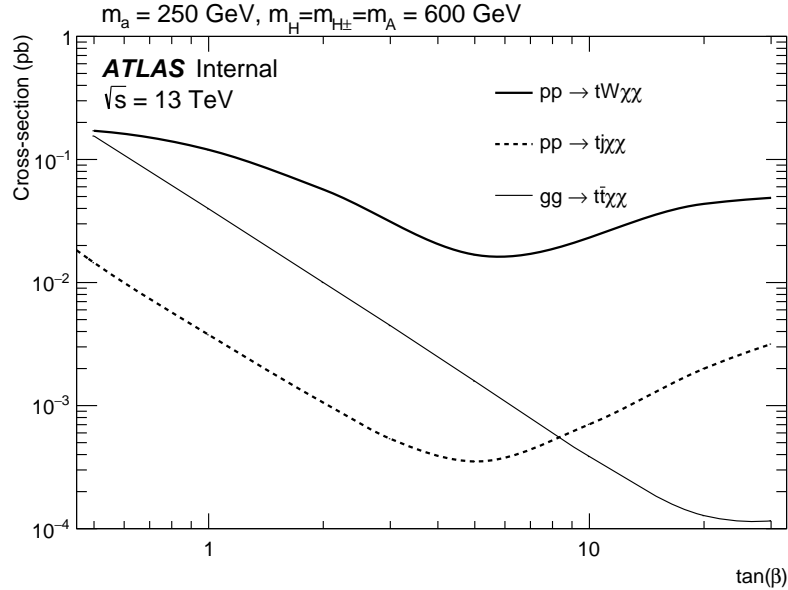


Figure 7.3: Diagram showing the production cross-section of DM produced in association with  $tW$ ,  $t$  and  $t\bar{t}$ . The associated  $t\bar{t}$  production cross-section is proportional to  $1/\tan^2\beta$  as described in [48].

## 1935 7.2 Event selection

1936 The event selection for this analysis begins with a set of preliminary, loose selections, known  
 1937 as ‘preselection’. The preselection cuts aim to select events matching the signal topology,  
 1938 while rejecting events with different topologies. All events are required to have exactly  
 1939 1 electron or muon in the final state, with any additional reconstructed leptons failing  
 1940 the ‘signal’ lepton requirements being rejected. At least three jets are required, to target  
 1941 events with at least one hadronically-decaying  $W$  boson, and at least one  $b$ -tagged jet is

required to select events with a top quark. To minimise the background contribution from  $t\bar{t}$ , events with a second  $b$ -tagged jet required it has a transverse momentum  $p_T(b_2) < 50$  GeV. The jets and  $E_T^{\text{miss}}$  must have an angular separation of at least 0.5 rad, to reject events which have mismeasured jets. All events are required to pass the event cleaning procedure described in Section 4.6, as well as passing one of the  $E_T^{\text{miss}}$  triggers as described in Section 3.1. In order to ensure a constant  $E_T^{\text{miss}}$  trigger efficiency, all events are required to have  $E_T^{\text{miss}} > 250$  GeV. The full preselection requirements for this analysis are defined in Table 7.2. The definitions for the objects used in this analysis are described in Chapter 4.

Variable	Selection
$N_\ell^{\text{baseline}}$	= 1
$N_\ell^{\text{signal}}$	= 1
$p_T(\ell_1)$	> 30 GeV
$N_{\text{jet}}$	$\geq 3$
$p_T(\text{jet})$	> 30 GeV
$N_{b\text{-jet}}$	$\geq 1$
$p_T(b\text{-jet})$	> 50 GeV
$E_T^{\text{miss}}$	> 250 GeV
$m_T$	> 30 GeV
$ \Delta\phi $	> 0.5 [rad]

Table 7.2: Preliminary selections used for the  $tW + E_T^{\text{miss}}$  analysis. All events are also required to pass the  $E_T^{\text{miss}}$  trigger, and the event cleaning requirements detailed in Section 4.6. The object definitions used are detailed in Chapter 4.

At the preselection-level, the dominant backgrounds, estimated from MC-only, are  $t\bar{t}$  (67%),  $W$ +jets (18%) and single top production (11%), where the percentages in parenthesis represents the contribution of that process to the total background. Four key variables were identified which enabled rejection of the backgrounds while maintaining a reasonably high signal selection efficiency;  $E_T^{\text{miss}}$ ,  $m_T$ ,  $am_{T2}$  and  $m_W^{\text{had}}$ . These variables are defined in Section 5.2. The  $am_{T2}$ ,  $m_T$  and  $m_W^{\text{had}}$  variables formed the inputs to simultaneous adaptive random grid search and genetic algorithms, as described in Section 5.3. The SR selections are summarised in Table 7.3.

### 7.3 Background estimation

The major backgrounds in the  $E_T^{\text{miss}}$  bins of the SR vary, depending on bin, between  $t\bar{t}$  and  $W$ +jets, with smaller contributions from  $Wt$ -channel single top production,  $t\bar{t} + V$  and the diboson backgrounds. A single-bin CR for the  $t\bar{t}$  background,  $\text{CR}(t\bar{t})$  and a 2-bin CR for the  $W$ +jets background,  $\text{CR}(W)$ , are defined. For the  $W$ +jets background, the CR is

Variable	Selection
$p_T(b_2)$	$< 50$ GeV
$m_T$	$> 200$ GeV
$am_{T2}$	$> 220$ GeV
$m_W^{\text{had}}$	$> 60$ GeV
$E_T^{\text{miss}}$ [binned]	$\in [250, 300]$ GeV
	$\in [300, 400]$ GeV
	$\in [400, 500]$ GeV
	$\in [500, 600]$ GeV
	$> 600$ GeV

Table 7.3: A table of the SR definitions, based on the

1964 separated into 2 bins of lepton charge to exploit the charge asymmetry of  $W^\pm$  production.  
 1965 The definitions of the CRs are given in Table 7.4.

Region	CR( $t\bar{t}$ )	CR( $W$ )
$N_\ell^{\text{signal}}$	= 1	
$p_T^{b1}$	$> 50$	
$p_T^{b2}$	$> 50$	$< 50$
$E_T^{\text{miss}}$	$> 250$	
$am_{T2}$	$< 220$	$> 220$
$m_T$	$> 200$	$\in [40, 100]$
$m_W$	–	$< 60$

Table 7.4: Control region definitions for the  $tW + E_T^{\text{miss}}$  analysis. The  $W$ +jets CR is split into two bins of lepton charge, such that the  $W^\pm$  production charge asymmetry can be exploited.

1966 6 validation regions are defined which are in a region of kinematic phase space that is  
 1967 between the CRs and SRs. Two  $t\bar{t}$  VRs are defined in order to validate the extrapolation  
 1968 of  $am_{T2}$  and  $m_W$ , while for the  $W$ +jets background, two VRs are defined to validate the  
 1969 extrapolation of  $m_T$  and  $m_W$ . Each of the  $W$ +jets VRs is split into two bins of lepton  
 1970 charge to mirror the CR definition. The VR definitions are explicitly defined in Table 7.5.

## 1971 7.4 Systematic uncertainties

1972 In addition to statistical uncertainties in the MC and on data, systematic uncertainties are  
 1973 evaluated on all MC background and signal samples, from both experimental and modelling  
 1974 sources. The experimental systematics considered are described in Section 5.4. The dom-  
 1975 inant experimental systematics in the SRs are from the JES, JER and  $b$ -tagging efficiency

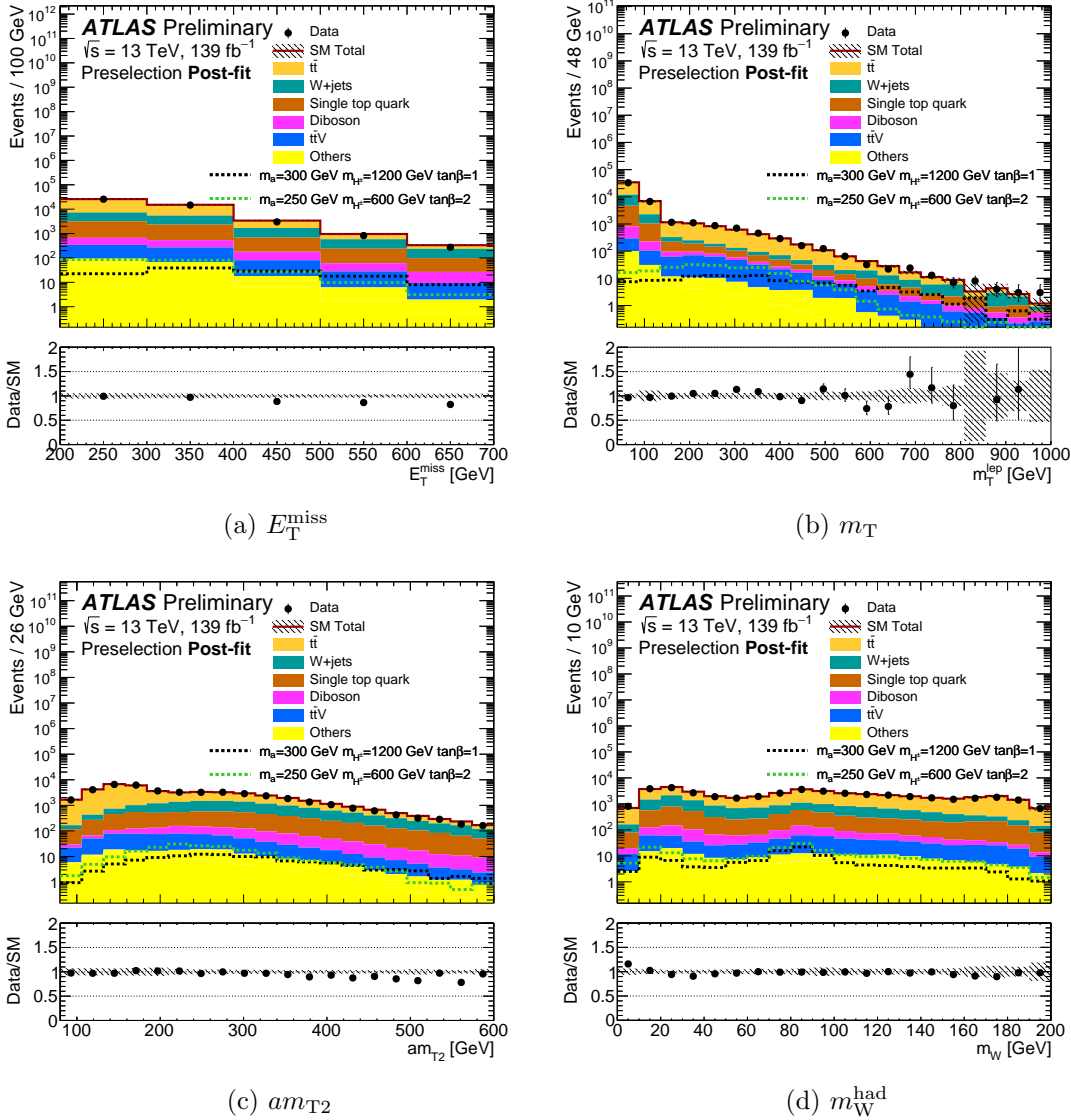


Figure 7.4: Post-fit plots of the key kinematic variables. The uncertainty band in the ratio plot contains only the MC statistical uncertainty and the experimental uncertainties.

1976 systematics. The modelling uncertainties on the  $t\bar{t}$  and single top backgrounds are the dominant  
 1977 modelling systematics in the SRs. The impact of the choice of the hard-scattering  
 1978 generator for the  $t\bar{t}$  and single-top backgrounds is evaluated by comparing the Powheg-Box  
 1979 nominal prediction with MadGraph5\_aMC@NLO, both interfaced to Pythia8. To assess the  
 1980 impact of the PS and hadronisation modelling, the nominal Powheg+Pythia8 configuration  
 1981 is compared with the nominal hard-scatter generator configuration interfaced to Herwig7.  
 1982 As previously described in Section ??, the uncertainty due to the modelling of the interference  
 1983 between the  $t\bar{t}$  and  $Wt$  processes is evaluated by comparing the DR and DS schemes,  
 1984 with the derived uncertainty applied to the nominal  $Wt$  prediction. The uncertainty due to  
 1985 the choice of renormalisation and factorisation scales, as well as the ISR and FSR param-

Region	VR1( $t\bar{t}$ )	VR2( $t\bar{t}$ )	VR1( $W$ )	VR2( $W$ )
$N_\ell^{\text{signal}}$			= 1	
$p_T^{b2}$			< 50	
$E_T^{\text{miss}}$			> 250	
$am_{T2}$	< 220	> 220	> 220	> 220
$m_T$	> 200	> 200	$\in [40, 100]$	> 100
$m_W$	–	< 60	> 60	< 60

Table 7.5: Validation region definitions for the  $tW + E_T^{\text{miss}}$  analysis. The  $W$ +jets VRs, like the CR, are each split into two bins of lepton charge.

1986 eters are varied using internal weights in the nominal sample. Table 7.6 gives an overview of the size of the dominant systematics in this analysis.

Source	Size (%)
	Modelling systematics
$t\bar{t}$ modelling	
Single top modelling	
	Experimental systematics
JES	
JER	
$b$ -tagging	

Table 7.6: Table showing a summary of the dominant experimental and modelling uncertainties.

1987

## 1988 7.5 Results

### 1989 Background-only fit results

1990 The background-only fit results in the CRs, VRs and SR bins for the single lepton channel  
 1991 are shown in Tables 7.7, 7.8 and 7.9, respectively. In this configuration, only the CRs enter  
 1992 the fit, allowing an estimate of the backgrounds in the VRs and SRs without any signal  
 1993 assumptions. Generally, excellent data/MC agreement is observed in the CRs and VRs,  
 1994 while in the SRs there are  $\sim 1\sigma$  excesses in bins 0 and 1 and an  $\sim 1\sigma$  underfluctuation of  
 1995 data in bin 4.

1996

1997 The background normalisation factors for the  $t\bar{t}$  and  $W$ +jets backgrounds, which are de-  
 1998 rived in the CRs, are shown in Table 7.10. These show excellent compatibility with the  
 1999 SM, agreeing with unity within  $1\sigma$ .

2000

2001 Figures 7.5, 7.6 and 7.7 show the key kinematic variables for the CRs, VRs and SRs, re-  
 2002 spectively, including background normalisation factors from the background-only fit. Good  
 modelling is seen in these variables.

<b>Control regions</b>	CR( $t\bar{t}$ )	CR( $W^+$ )	CR( $W^-$ )
Observed events	911	3143	1653
Fitted bkg events	$907.41 \pm 30.52$	$3135.45 \pm 56.87$	$1665.08 \pm 37.50$
Fitted Top1L events	$846.96 \pm 34.11$	$748.75 \pm 83.42$	$720.78 \pm 86.33$
Fitted SingleTop events	$19.82 \pm 11.53$	$276.59 \pm 69.50$	$257.00 \pm 70.15$
Fitted Wjets events	$3.18 \pm 0.75$	$2005.00 \pm 98.23$	$625.41 \pm 42.11$
Fitted Zjets events	$0.13^{+0.16}_{-0.13}$	$6.63 \pm 0.99$	$8.39 \pm 1.29$
Fitted Diboson events	$0.87 \pm 0.25$	$88.85 \pm 15.55$	$46.05 \pm 8.01$
Fitted ttV events	$31.01 \pm 7.12$	$8.16 \pm 2.69$	$5.96 \pm 1.52$
Fitted ttH events	$4.37 \pm 0.41$	$1.12 \pm 0.17$	$1.17 \pm 0.11$
Fitted tWZ events	$1.07 \pm 0.29$	$0.36 \pm 0.13$	$0.32 \pm 0.11$
MC exp. SM events	$887.37 \pm 88.05$	$3189.60 \pm 85.25$	$1759.71 \pm 97.50$
MC exp. Top1L events	$824.87 \pm 86.06$	$801.90 \pm 36.82$	$785.78 \pm 51.79$
MC exp. SingleTop events	$21.98 \pm 11.84$	$307.91 \pm 73.54$	$292.39 \pm 77.62$
MC exp. Wjets events	$3.06 \pm 0.75$	$1973.56 \pm 21.27$	$619.13 \pm 17.57$
MC exp. Zjets events	$0.14^{+0.17}_{-0.14}$	$6.62 \pm 0.99$	$8.46 \pm 1.33$
MC exp. Diboson events	$0.88 \pm 0.25$	$89.91 \pm 15.87$	$46.48 \pm 8.12$
MC exp. ttV events	$30.96 \pm 7.19$	$8.19 \pm 2.74$	$5.96 \pm 1.53$
MC exp. ttH events	$4.40 \pm 0.42$	$1.14 \pm 0.17$	$1.18 \pm 0.11$
MC exp. tWZ events	$1.07 \pm 0.29$	$0.36 \pm 0.13$	$0.33 \pm 0.11$

Table 7.7: Results of the background-only fit in the control regions for the single lepton channel of the search targeting the 2HDM+ $a$   $tW + E_T^{\text{miss}}$  signature. This fit includes only the control regions used to normalise the  $t\bar{t}$  and  $W$ +jets backgrounds.

2003

Validation regions	VR1( $t\bar{t}$ )	VR2( $t\bar{t}$ )	VR1( $W^+$ )	VR1( $W^-$ )	VR2( $W^+$ )	VR2( $W^-$ )
Observed events	1389	482	6127	4479	651	464
Fitted bkg events	$1394.19 \pm 87.29463.79$	$33.546721.98$	$451.825025.60$	$440.57613.26$	$69.87475.28$	$49.85$
Fitted Top1L events	$1221.12 \pm 70.15282.62$	$28.473644.44$	$331.573570.86$	$354.94282.17$	$40.09285.73$	$41.18$
Fitted SingleTop events	$53.19^{+59.36}_{-53.19}$	$56.98 \pm 24.51$	$626.01 \pm 280.23$	$612.94 \pm 274.02$	$71.09 \pm 36.09$	$73.39 \pm 38.19$
Fitted Wjets events	$39.07 \pm 8.23$	$68.62 \pm 11.942245.29$	$131.23$	$719.06 \pm 48.51203.16$	$42.05$	$70.12 \pm 12.03$
Fitted Zjets events	$3.97 \pm 2.14$	$2.67 \pm 0.46$	$7.66 \pm 1.05$	$7.33 \pm 1.00$	$3.56 \pm 0.93$	$2.38 \pm 0.39$
Fitted Diboson events	$15.29 \pm 3.21$	$27.15 \pm 5.48$	$160.21 \pm 28.44$	$85.60 \pm 15.61$	$34.51 \pm 7.06$	$25.89 \pm 5.81$
Fitted $t\bar{t}V$ events	$54.42 \pm 12.05$	$22.54 \pm 5.03$	$32.39 \pm 2.79$	$23.86 \pm 3.07$	$16.34 \pm 3.79$	$15.27 \pm 3.53$
Fitted $t\bar{t}H$ events	$3.57 \pm 0.27$	$0.71 \pm 0.04$	$4.48 \pm 0.33$	$4.37 \pm 0.43$	$0.69 \pm 0.03$	$0.71 \pm 0.05$
Fitted $tWZ$ events	$3.56 \pm 0.82$	$2.50 \pm 0.62$	$1.51 \pm 0.17$	$1.58 \pm 0.22$	$1.72 \pm 0.44$	$1.79 \pm 0.46$
MC exp. SM events	$1372.55 \pm 136.76479.15$	$31.636531.69$	$623.894916.48$	$572.80646.06$	$76.28513.95$	$55.99$
MC exp. Top1L events	$1196.25 \pm 120.04295.27$	$11.813446.89$	$545.333431.71$	$495.53307.24$	$29.76315.14$	$29.76$
MC exp. SingleTop events	$56.60^{+61.50}_{-56.60}$	$60.42 \pm 24.75$	$663.43 \pm 286.28$	$650.26 \pm 279.62$	$79.55 \pm 36.91$	$82.83 \pm 38.83$
MC exp. Wjets events	$38.71 \pm 7.57$	$67.65 \pm 10.70$	$2213.59 \pm 60.05$	$710.50 \pm 27.57202.11$	$38.29$	$69.50 \pm 10.63$
MC exp. Zjets events	$3.90 \pm 2.12$	$2.67 \pm 0.47$	$7.73 \pm 1.07$	$7.40 \pm 1.03$	$3.53 \pm 0.94$	$2.40 \pm 0.40$
MC exp. Diboson events	$15.47 \pm 3.26$	$27.35 \pm 5.53$	$161.45 \pm 28.79$	$86.62 \pm 15.95$	$34.78 \pm 7.11$	$26.22 \pm 5.91$
MC exp. $t\bar{t}V$ events	$54.45 \pm 12.19$	$22.57 \pm 5.09$	$32.55 \pm 2.84$	$23.97 \pm 3.11$	$16.41 \pm 3.85$	$15.34 \pm 3.58$
MC exp. $t\bar{t}H$ events	$3.60 \pm 0.28$	$0.72 \pm 0.04$	$4.52 \pm 0.34$	$4.42 \pm 0.44$	$0.70 \pm 0.03$	$0.72 \pm 0.05$
MC exp. $tWZ$ events	$3.58 \pm 0.83$	$2.52 \pm 0.63$	$1.52 \pm 0.18$	$1.59 \pm 0.23$	$1.73 \pm 0.44$	$1.80 \pm 0.46$

Table 7.8: Results of the background-only fit in the validation regions for the single lepton channel of the search targeting the 2HDM+ $a$   $tW + E_T^{\text{miss}}$  signature. This fit includes only the control regions used to normalise the  $t\bar{t}$  and  $W + \text{jets}$  backgrounds.

Signal regions	SR1LBin0	SR1LBin1	SR1LBin2	SR1LBin3	SR1LBin4
Observed events	182	191	60	24	12
Fitted bkg events	$169.12 \pm 13.98$	$171.28 \pm 13.34$	$54.70 \pm 6.05$	$20.16 \pm 2.84$	$15.55 \pm 2.79$
Fitted Top1L events	$101.34 \pm 11.94$	$83.65 \pm 11.53$	$20.07 \pm 4.56$	$5.12 \pm 1.70$	$2.31 \pm 1.48$
Fitted SingleTop events	$16.28 \pm 5.19$	$17.26 \pm 5.22$	$5.42 \pm 3.23$	$2.00 \pm 1.77$	$1.68^{+2.02}_{-1.68}$
Fitted Wjets events	$27.77 \pm 4.02$	$37.05 \pm 4.34$	$14.24 \pm 2.44$	$6.11 \pm 0.97$	$5.87 \pm 1.08$
Fitted Zjets events	$2.02 \pm 0.91$	$1.10 \pm 0.68$	$0.33 \pm 0.09$	$0.15 \pm 0.04$	$0.15 \pm 0.02$
Fitted Diboson events	$7.20 \pm 1.69$	$9.65 \pm 2.00$	$4.59 \pm 1.00$	$2.24 \pm 0.47$	$2.59 \pm 0.65$
Fitted ttV events	$12.28 \pm 1.36$	$19.55 \pm 3.51$	$8.71 \pm 1.20$	$4.05 \pm 0.72$	$2.53 \pm 0.45$
Fitted ttH events	$0.56 \pm 0.06$	$0.60 \pm 0.06$	$0.17 \pm 0.02$	$0.06 \pm 0.02$	$0.03 \pm 0.00$
Fitted tWZ events	$1.66 \pm 0.21$	$2.42 \pm 0.46$	$1.17 \pm 0.15$	$0.42 \pm 0.09$	$0.39 \pm 0.09$
MC exp. SM events	$172.49 \pm 16.86$	$174.00 \pm 14.12$	$55.72 \pm 6.71$	$20.60 \pm 3.05$	$16.76 \pm 3.15$
MC exp. Top1L events	$103.13 \pm 12.92$	$85.61 \pm 10.81$	$20.39 \pm 4.67$	$5.28 \pm 1.72$	$2.92 \pm 1.51$
MC exp. SingleTop events	$17.86 \pm 5.85$	$18.63 \pm 5.36$	$6.02 \pm 3.34$	$2.33 \pm 1.85$	$2.35 \pm 2.17$
MC exp. Wjets events	$27.59 \pm 3.69$	$36.22 \pm 4.24$	$14.21 \pm 2.25$	$6.06 \pm 0.87$	$5.75 \pm 1.00$
MC exp. Zjets events	$2.08 \pm 0.91$	$1.09 \pm 0.67$	$0.33 \pm 0.09$	$0.15 \pm 0.04$	$0.15 \pm 0.02$
MC exp. Diboson events	$7.30 \pm 1.72$	$9.73 \pm 2.01$	$4.64 \pm 1.02$	$2.24 \pm 0.47$	$2.62 \pm 0.66$
MC exp. ttV events	$12.30 \pm 1.38$	$19.67 \pm 3.59$	$8.77 \pm 1.22$	$4.06 \pm 0.72$	$2.55 \pm 0.46$
MC exp. ttH events	$0.56 \pm 0.06$	$0.61 \pm 0.06$	$0.18 \pm 0.02$	$0.06 \pm 0.02$	$0.03 \pm 0.00$
MC exp. tWZ events	$1.67 \pm 0.22$	$2.44 \pm 0.46$	$1.18 \pm 0.15$	$0.42 \pm 0.10$	$0.39 \pm 0.09$

Table 7.9: Results of the background-only fit in the signal region for the single lepton channel of the search targeting the 2HDM+ $a$   $tW + E_{\text{T}}^{\text{miss}}$  signature. This fit includes only the control regions used to normalise the  $t\bar{t}$  and  $W$ +jets backgrounds.

1 $\ell$ analysis	
$\mu(t\bar{t})$	$0.96 \pm 0.08$
$\mu(W)$	$1.01 \pm 0.05$
1 $\ell$ + 2 $\ell$ combination	
$\mu(t\bar{t} \ 1\ell)$	$0.96 \pm 0.08$
$\mu(t\bar{t} \ 2\ell)$	$1.00 \pm 0.03$
$\mu(W)$	$1.01 \pm 0.05$
$\mu(WZ)$	$0.75 \pm 0.26$
$\mu(t\bar{t}Z)$	$0.81 \pm 0.16$

Table 7.10: Background normalisation factors the  $tW + E_{\text{T}}^{\text{miss}}$  analysis

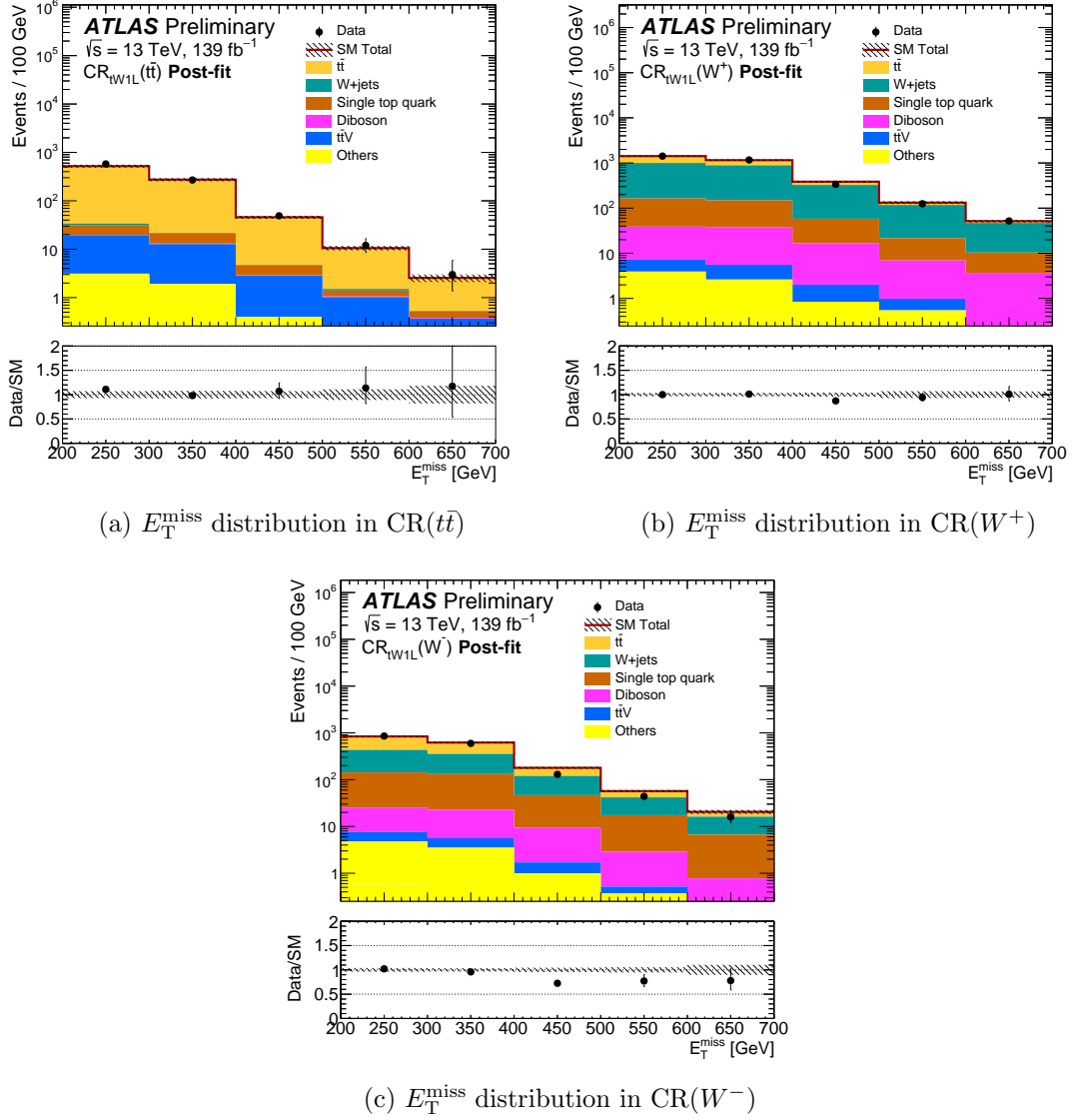


Figure 7.5: Post-fit distributions of the  $E_T^{\text{miss}}$  variable in all CRs. Excellent data/MC agreement is observed. The uncertainty band on the ratio contains the MC statistical, experimental and modelling uncertainties.

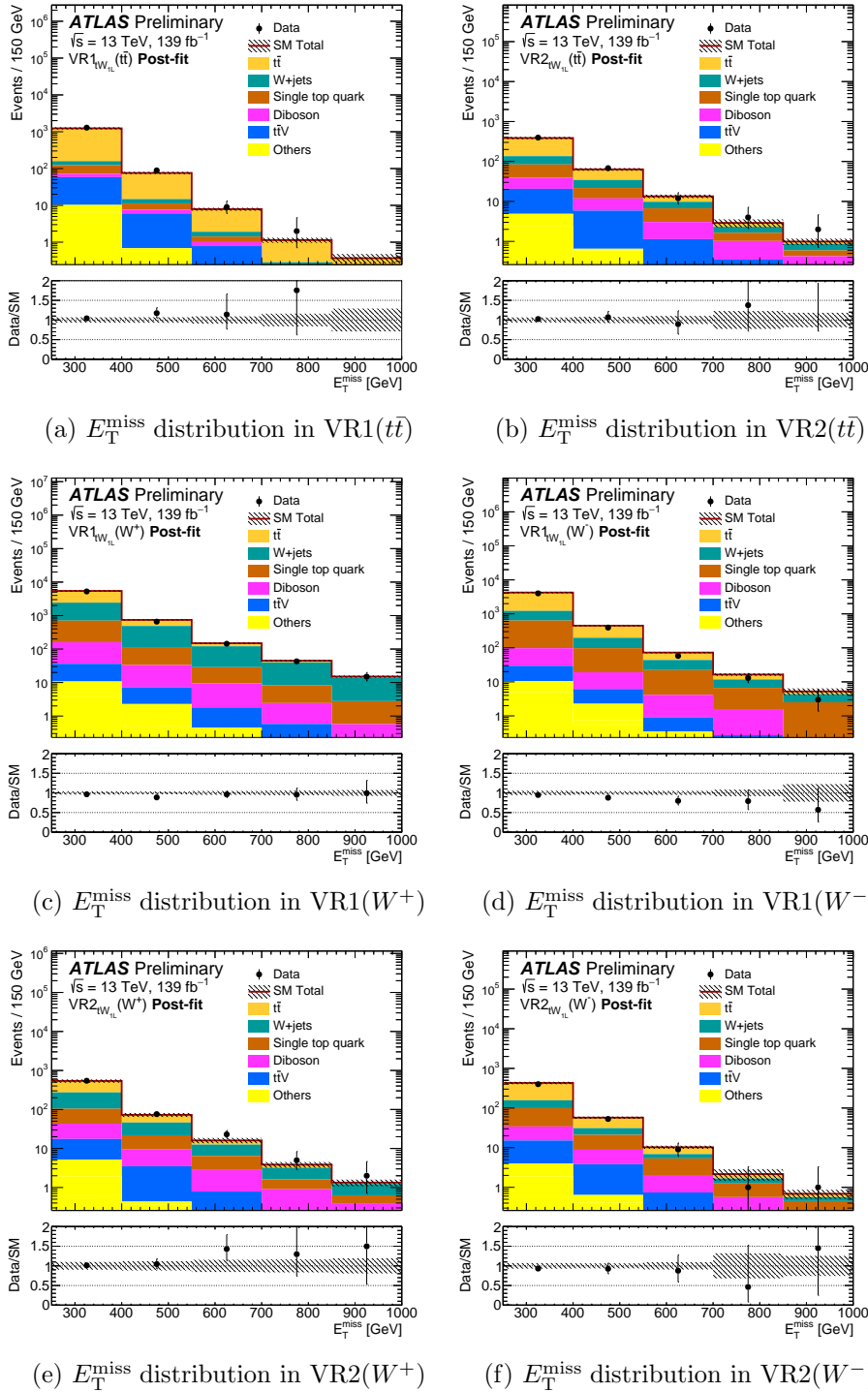


Figure 7.6: Plots showing the  $E_T^{\text{miss}}$  distribution in all VRs. Good agreement between data and MC in all regions is observed. The uncertainty band on the ratio includes MC statistical, experimental and modelling uncertainties.

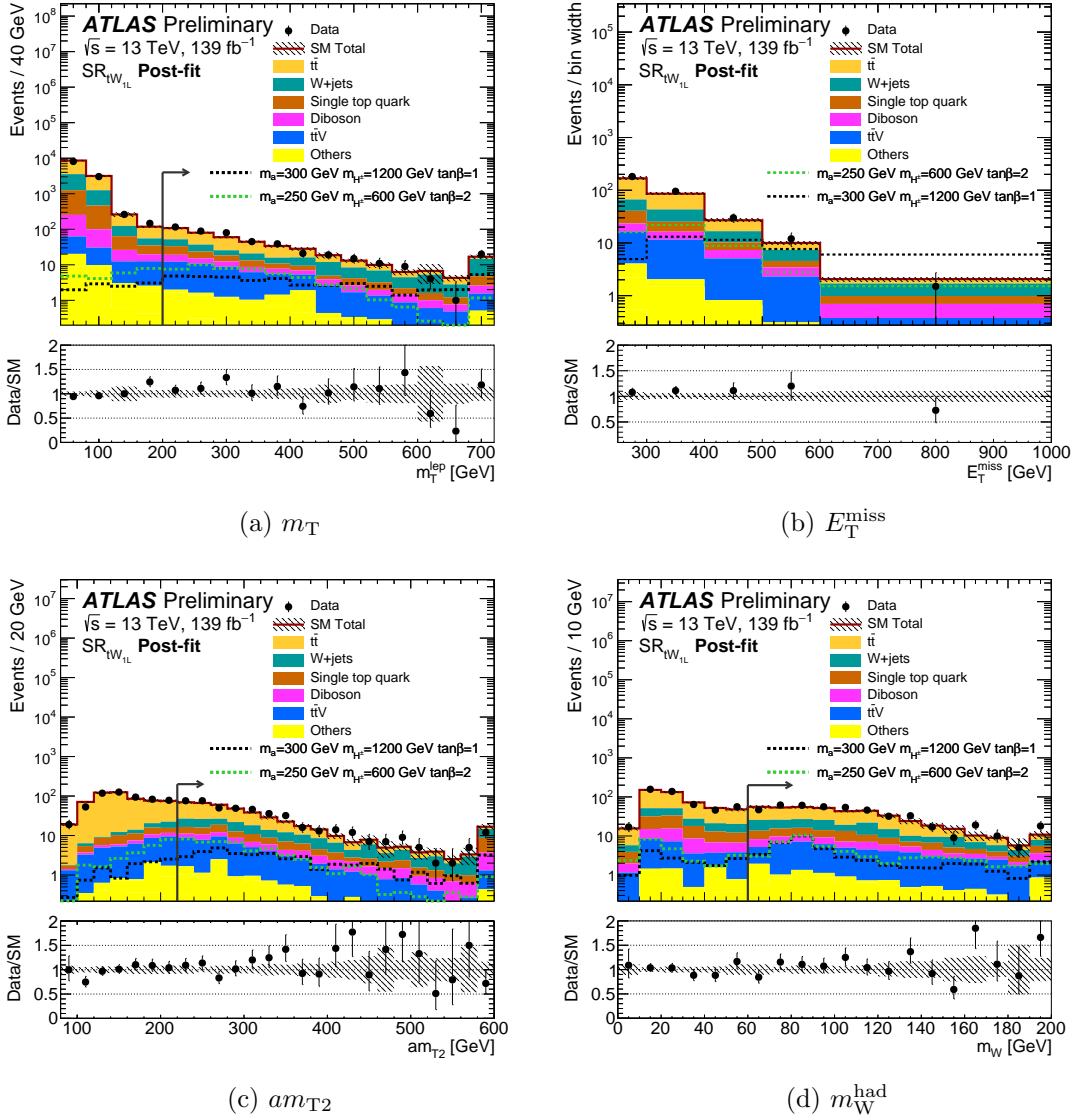


Figure 7.7: Plots showing the post-fit N-1 distributions of the key kinematic variables. In these plots, all selections are applied except those on the variable being plotted. All uncertainties are included in the error band on the ratio. No significant excess is observed in the SR bins.

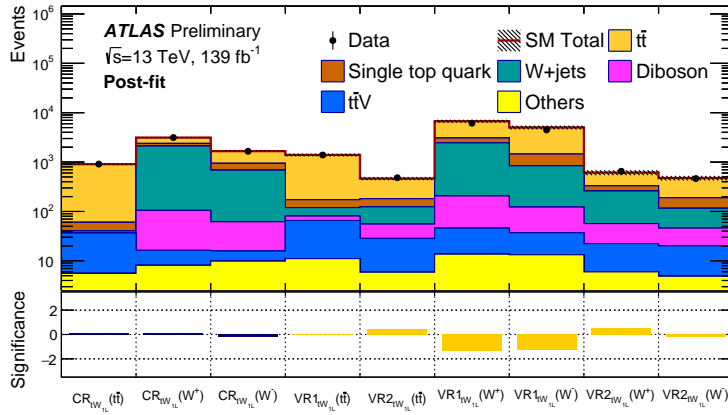
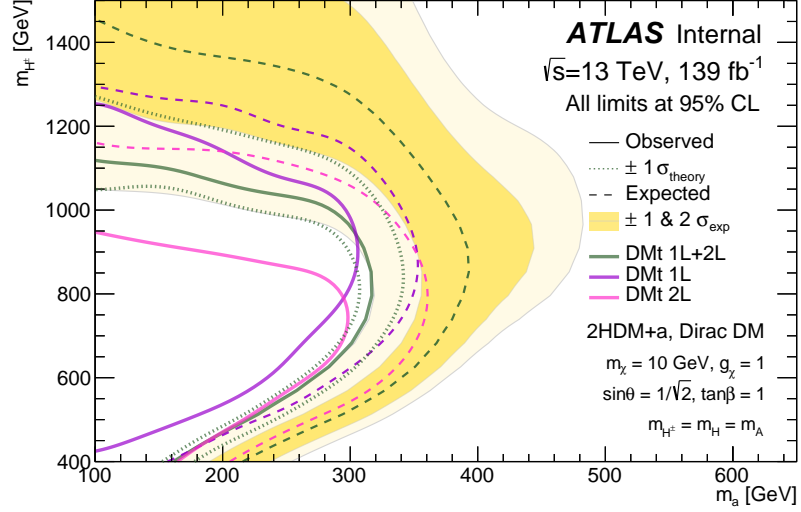


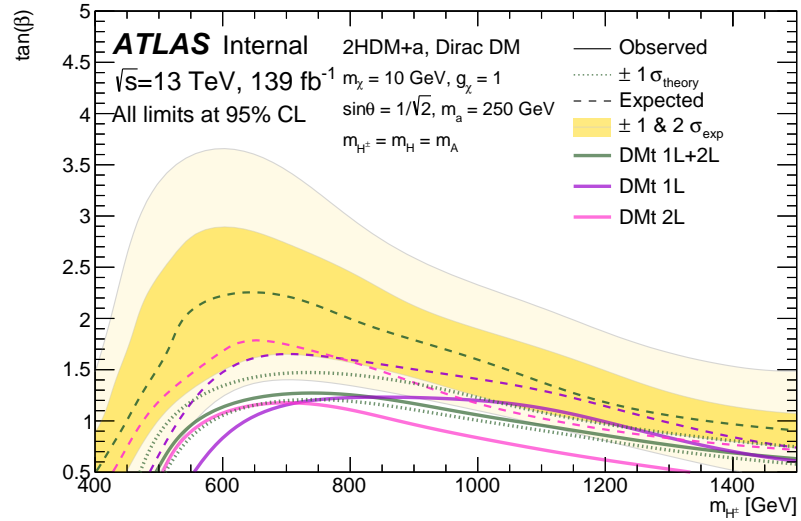
Figure 7.8: Summary plot showing the data/MC agreement in all control and validation regions for the single lepton channel of the search targeting the 2HDM+ $a$   $tW+E_T^{\text{miss}}$  signature. The uncertainty used to calculate the significance of the data/MC difference includes the statistical component on the MC and the data, as well as the total systematic uncertainty on the background estimate.

#### 2004 Model-dependent limits

2005 In the absence of a significant excess, limits are set on the 2HDM+ $a$  model at 95% con-  
 2006 fidence limits using the previously described prescription. Model-dependent limits are set  
 2007 on the DM $t$  and the DM $t + t\bar{t}$  signatures, in both the  $m_a - m_{H\pm}$  and  $m_{H\pm} - \tan\beta$  planes.  
 2008 For the DM $t$  signature,  $H^\pm$  masses are excluded upto 1250 GeV for  $m_a = 100$  GeV, while  
 2009 for the DM $t + t\bar{t}$  signature masses above 1400 GeV are excluded. The observed limit of  
 2010 the statistical combination of the  $1\ell$  and  $2\ell$  channels is not as sensitive as the dedicated  $1\ell$   
 2011 channel due to the  $2\sigma$  excess in the  $2\ell$  SR.

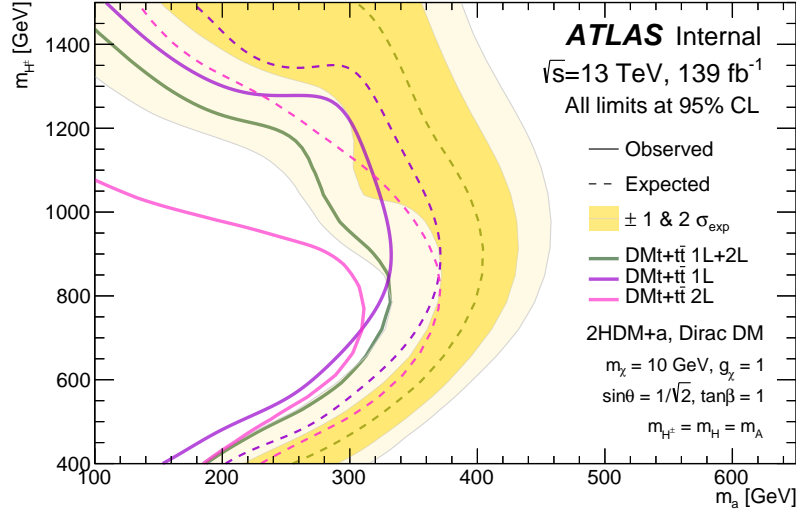


(a)

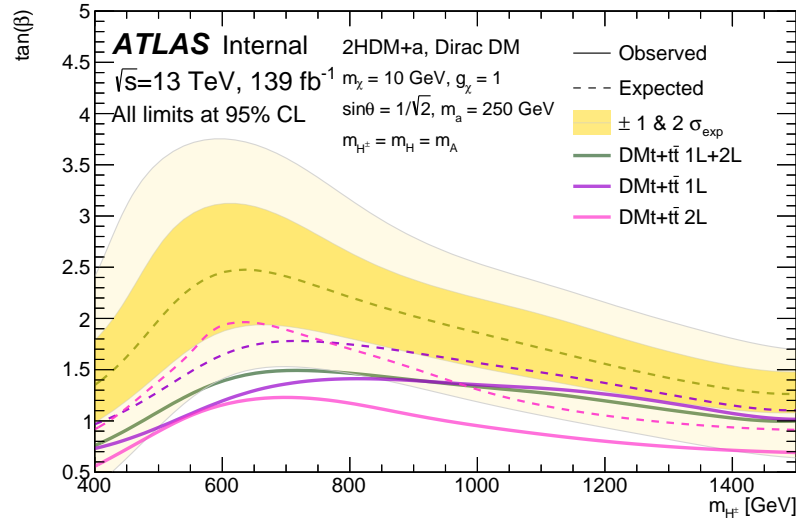


(b)

Figure 7.9: Plots showing the sensitivity to the 2HDM+a signal with the  $tW + E_T^{\text{miss}}$  signature. Limits are shown in both the  $m_a$ - $m_{H^\pm}$  plane (a) and the  $m_{H^\pm}$ - $\tan(\beta)$  plane (b). Limits are shown for the analyses targeting the single lepton and di-lepton final states, along with the statistical combination of both channels.



(a)



(b)

Figure 7.10: Plots showing the sensitivity to the 2HDM+ $a$  signal for both  $tW$  and  $t\bar{t}$  signatures. Limits are shown in both the  $m_a$ - $m_{H^\pm}$  plane (a) and the  $m_{H^\pm}$ - $\tan(\beta)$  plane (b). Limits are shown for the analyses targeting the single lepton and di-lepton final states, along with the statistical combination of both channels.

2012 **Model-independent limits**

2013 In addition to model-dependent limits being set on the 2HDM+ $a$  signal model, with both  
 2014  $tW$  and  $tW + t\bar{t}$  signatures, 95% CL limits are set on any generic BSM processes using the  
 2015 model-independent fit strategy described in Section 5.5. The limits are presented as limits  
 2016 on the *visible* cross-section,  $\sigma_{\text{vis}} = \epsilon \cdot A \cdot \sigma_{BSM}$ , where  $\epsilon$  is the signal selection efficiency,  
 2017  $A$  is the detector acceptance, and  $\sigma_{\text{vis}}$  is the production cross-section for a generic BSM  
 2018 process. To set limits on a generic BSM process, the SR definition from Table 7.3 are  
 2019 modified, such that the individual SR bins have no upper  $E_T^{\text{miss}}$  limit and rather only a  
 2020 lower  $E_T^{\text{miss}}$  threshold. The yields in these modified, ‘inclusive’ SR bins are shown in Table  
 2021 7.11. The results of the model-independent fit are shown in Table 7.12, as 95% CL limits  
 2022 on the expected and observed number of signal events.

<b>Inclusive signal regions</b>						
$E_T^{\text{miss}}$ threshold [GeV]	> 250	> 300	> 400	> 500	> 600	
Observed events	469	287	96	36	12	
Fitted bkg events	$431.47 \pm 27.12$	$261.90 \pm 20.10$	$90.65 \pm 10.07$	$35.94 \pm 5.22$	$15.54 \pm 2.77$	
Fitted Top1L events	$212.61 \pm 25.01$	$111.14 \pm 17.69$	$27.51 \pm 7.36$	$7.44 \pm 2.94$	$2.31 \pm 1.48$	
Fitted SingleTop events	$43.28 \pm 14.49$	$26.66 \pm 11.76$	$9.35 \pm 6.53$	$3.92 \pm 3.85$	$1.68^{+2.02}_{-1.68}$	
Fitted Wjets events	$91.05 \pm 7.64$	$63.29 \pm 5.47$	$26.24 \pm 2.82$	$11.99 \pm 1.67$	$5.87 \pm 1.08$	
Fitted Zjets events	$3.76 \pm 1.03$	$1.72 \pm 0.69$	$0.62 \pm 0.12$	$0.30 \pm 0.05$	$0.15 \pm 0.02$	
Fitted Diboson1L events	$26.26 \pm 5.49$	$19.06 \pm 3.92$	$9.42 \pm 1.97$	$4.83 \pm 1.01$	$2.59 \pm 0.65$	
Fitted ttV1L events	$47.01 \pm 2.76$	$34.75 \pm 2.39$	$15.27 \pm 1.17$	$6.57 \pm 0.48$	$2.53 \pm 0.33$	
Fitted ttH events	$1.42 \pm 0.09$	$0.87 \pm 0.07$	$0.26 \pm 0.02$	$0.09 \pm 0.02$	$0.03 \pm 0.00$	
Fitted tWZ events	$6.07 \pm 0.37$	$4.40 \pm 0.31$	$1.99 \pm 0.13$	$0.81 \pm 0.08$	$0.39 \pm 0.04$	
MC exp. SM events	$439.58 \pm 32.24$	$267.09 \pm 22.29$	$93.09 \pm 11.12$	$37.36 \pm 5.64$	$16.76 \pm 3.13$	
MC exp. Top1L events	$217.33 \pm 24.57$	$114.20 \pm 16.85$	$28.59 \pm 7.33$	$8.20 \pm 2.91$	$2.92 \pm 1.51$	
MC exp. SingleTop events	$47.20 \pm 15.05$	$29.34 \pm 12.03$	$10.70 \pm 6.75$	$4.69 \pm 4.00$	$2.35 \pm 2.17$	
MC exp. Wjets events	$89.83 \pm 6.17$	$62.24 \pm 4.79$	$26.02 \pm 2.29$	$11.81 \pm 1.49$	$5.75 \pm 1.00$	
MC exp. Zjets events	$3.80 \pm 1.04$	$1.72 \pm 0.68$	$0.63 \pm 0.12$	$0.30 \pm 0.05$	$0.15 \pm 0.02$	
MC exp. Diboson1L events	$26.52 \pm 5.55$	$19.23 \pm 3.96$	$9.50 \pm 1.99$	$4.86 \pm 1.01$	$2.62 \pm 0.66$	
MC exp. ttV1L events	$47.36 \pm 2.90$	$35.05 \pm 2.50$	$15.38 \pm 1.20$	$6.61 \pm 0.49$	$2.55 \pm 0.34$	
MC exp. ttH events	$1.44 \pm 0.09$	$0.88 \pm 0.07$	$0.27 \pm 0.02$	$0.09 \pm 0.02$	$0.03 \pm 0.00$	
MC exp. tWZ events	$6.11 \pm 0.38$	$4.44 \pm 0.32$	$2.00 \pm 0.13$	$0.82 \pm 0.09$	$0.39 \pm 0.04$	

Table 7.11: Table showing the expected and observed yields in the modified signal regions for the determination of the model-independent limits.

Region	$\langle\epsilon\sigma\rangle_{\text{obs}}^{95}$ [fb]	$S_{\text{obs}}^{95}$	$S_{\text{exp}}^{95}$
SR1L ( $E_{\text{T}}^{\text{miss}} > 250$ GeV)	0.72	100.6	$66.7^{+32.7}_{-16.4}$
SR1L ( $E_{\text{T}}^{\text{miss}} > 300$ GeV)	0.51	70.8	$54.1^{+16.0}_{-15.9}$
SR1L ( $E_{\text{T}}^{\text{miss}} > 400$ GeV)	0.24	32.9	$29.4^{+10.1}_{-6.4}$
SR1L ( $E_{\text{T}}^{\text{miss}} > 500$ GeV)	0.14	18.9	$18.7^{+7.6}_{-4.9}$
SR1L ( $E_{\text{T}}^{\text{miss}} > 600$ GeV)	0.08	10.6	$12.0^{+2.7}_{-3.6}$

Table 7.12: Table showing the model-independent limits derived for the five modified inclusive SRs. Visible cross-sections of BSM physics upto 0.72fb are excluded at 95% confidence limits, translating to an upper limit of around 100 events with a dataset of  $139\text{fb}^{-1}$ .

2023

## Part III

2024

# High-Luminosity LHC studies

## Chapter 8

# Sensitivity to $\tilde{\chi}_1^\pm \tilde{\chi}_2^0$ pair-production at the HL-LHC

This chapter explores the potential sensitivity of a search for chargino-neutralino pair-production using the ATLAS detector during the HL-LHC phase of operation. The HL-LHC is expected to begin operation in the latter half of the 2020's, bringing instantaneous luminosities around an order of magnitude higher than those currently at the LHC ( $7.5 \times 10^{34}$ ), along with an increase in centre-of-mass energy to  $\sqrt{s} = 14$  TeV. It is expected that by the end of the HL-LHC phase, ATLAS will have taken  $3000\text{fb}^{-1}$  of data, an expected ten-fold increase over the combination of Runs 2 and 3.

Along with the increased luminosity and collision energy delivered by the LHC, the ATLAS detector will be undergoing major upgrades in Long Shutdown 3 (LS3), providing an overhaul of many of the detector's subsystems. Of particular note is the new Inner Tracker (ITk), which will replace the current innermost tracking layers of the current ATLAS detector, vastly improving on the vertex resolution which will enable accurate track reconstruction in collisions with an average number of interactions per bunch-crossing,  $\langle\mu\rangle$ , of 200. Figure 8.1 shows a simulated  $t\bar{t}$  event display from the ATLAS ITk in the expected pileup conditions at the HL-LHC.

With the increased centre-of-mass energy and the expected  $3000\text{fb}^{-1}$  dataset, the physics analysis potential of the HL-LHC is unprecedented. Much of the HL-LHC physics program will be devoted to precision measurements of properties related to the Higgs boson and its relationship with the symmetry breaking mechanism of the electroweak sector of the SM. First sensitivity to the Higgs self-coupling is expected to be possible in the  $HH \rightarrow b\bar{b}\gamma\gamma$  channel through both a conventional cut-and-count analysis [49] and a multivariate analysis [50]. This measurement will be used in combination with measurements in other final states, such as  $b\bar{b}\tau\tau$  and  $b\bar{b}b\bar{b}$  [51], further increasing sensitivity. It is also expected that measurements of the largest Higgs boson couplings to SM particles will be done with percent-level precision. Along with increased precision in measurements and

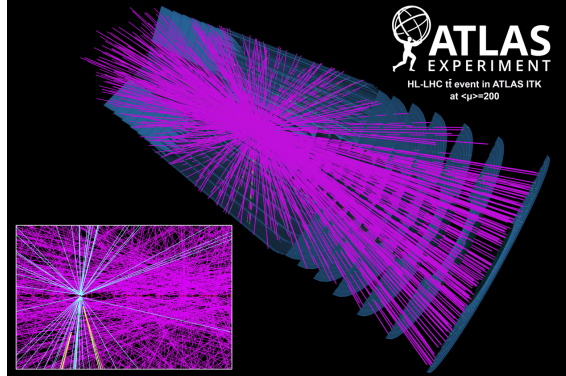


Figure 8.1: An event display of a simulated  $t\bar{t}$  event in the ATLAS ITk at the HL-LHC, where there are an expected 200 interactions per bunch-crossing.

2053 sensitivity to SM properties, the HL-LHC will also bring increased sensitivity to TeV-scale  
 2054 new physics. This chapter describes one such prospects analysis, forming part of a plethora  
 2055 of sensitivity studies [52].

2056 The analysis described in this chapter targets the same signal model as in Chapter  
 2057 ??, with a final state of a single electron/muon, two  $b$ -jets and  $E_T^{\text{miss}}$ . The sensitivity is  
 2058 assessed in the context of current expected HL-LHC conditions. Due to the huge dataset  
 2059 expected to be collected at the HL-LHC, the sensitivity is expected to reach far beyond  
 2060 the Run-2 sensitivity, and as such, mass upto 1500 GeV are considered for the  $\tilde{\chi}_1^\pm/\tilde{\chi}_2^0$ .

## 2061 8.1 MC simulation

2062 Signal samples for this study are generated at leading-order in QCD, with upto two ad-  
 2063 ditional partons, using MADGRAPH5\_aMC@NLO [53] for the matrix element (ME), while  
 2064 PYTHIA 8 [54] is used for the parton showering (PS), hadronisation and underlying event  
 2065 (UE). The A14 tune is used for PYTHIA 8 [55] while the NNPDF23LO PDF set [56] is used  
 2066 for generation. Partons are matched between the ME and PS using the CKKW-L [57] pre-  
 2067 scription, with the scale used for matching set to one quarter of the mass of the  $\tilde{\chi}_1^\pm/\tilde{\chi}_2^0$ . The  
 2068 cross-sections are evaluated at next-to-leading order in  $\alpha_s$  and next-to-leading logarithmic  
 2069 precision for the resummation of soft gluon emissions. The nominal cross section is de-  
 2070 termined by evaluating the cross section predictions with different PDF sets, factorisation  
 2071 and renormalisation scales [58]. Similarly to the analyses previously described, numerous  
 2072 generator configurations were used to generate the MC background samples. These are  
 2073 summarised in Table 8.1.

2074 All samples are generated at truth-level. A parameterised simulation of the detector  
 2075 response is applied to all truth-level MC samples. This will be described in more detail in  
 2076 the following section.

Process	Generator + fragmentation/hadronisation	Tune	PDF set	Cross-section order
$W/Z$ +jets	SHERPA 2.2.1 [?]	Default	NNPDF30NNLO [?]	NNLO
$t\bar{t}$	POWHEG-BOX v2 + PYTHIA 8.186	A14	NNPDF23LO [?]	NNLO+NNLL
Single top	POWHEG-BOX v1 or v2 + PYTHIA 6.428 [?]	PERUGIA2012 [?]	CT10 [?]	NNLO+NNLL
Diboson (fully leptonic)	SHERPA 2.2.1	Default	NNPDF30NNLO	NLO
(semi leptonic)	POWHEG-BOX v1 + PYTHIA 8.186	AZNLO [?]	CTEQ6L1	NLO
Higgs	POWHEG-BOX v2 + PYTHIA 8.186	AZNLO	CTEQ6L1	NNLO+NNLL

Table 8.1: Summary table showing the ME and PS configurations used to generate the SM MC samples for this study.

## 2077 8.2 Detector simulation

2078 In order to make meaningful predictions of sensitivity, a simulation of the ATLAS detector  
 2079 at the HL-LHC was developed through a set of parameterised smearing functions. These  
 2080 functions, known as the UpgradePerformanceFunctions, simulate the detector response by  
 2081 smearing the kinematic and angular properties of the physics objects, as well as providing  
 2082 additional collision vertices to simulate the pileup conditions at the HL-LHC. The treat-  
 2083 ment of each object relevant to this chapter will be discussed separately. Some shorthand  
 2084 will now be introduced for the following sections.  $R(m, n)$  represents a random number  
 2085 drawn from a uniform distribution in the range  $m$  to  $n$ .  $G(\mu, \sigma)$  represents a number drawn  
 2086 from a Gaussian distribution with a mean,  $\mu$ , and a standard deviation,  $\sigma$ .

### 2087 Leptons

2088 The steps taken in the reconstruction of charged leptons is highly dependent on the gener-  
 2089 ation of lepton being considered, but there are some common steps. Lepton ID working  
 2090 points are assigned for all three generations of charged leptons, and the detector response  
 2091 to the  $E_T$  for electrons and taus and  $p_T$  for muons is simulated. The charge-flip probability  
 2092 (the probability that the reconstructed lepton has the opposite charge to its true value),  
 2093  $P(\ell_{truth}^\pm \rightarrow \ell_{reco}^\mp)$ , is explicitly parameterised for electrons and is also possible for muons.  
 2094 Finally, the misreconstruction of an electron as a photon is parameterised.

2095  
 2096 A parameterisation of the lepton ID efficiencies is used in order to choose which lepton  
 2097 ID working points the lepton has passed. For each lepton generation there are three ID  
 2098 efficiency parameterisations, one corresponding to each working point. These parameteri-  
 2099 sations can be seen in Figure A.1. For a given lepton, the three ID efficiencies corresponding  
 2100 to the ID working points are retrieved, and all which satisfy  $R(0, 1) < \epsilon_{ID}^i$ , with  $i = 1, 2, 3$ ,  
 2101 are passed.

2102

2103 The  $p_T$  resolution for leptons is simulated differently for muons than for electrons and  
 2104 taus. For the former, the key quantity is the charge (in units of  $e$ ) to transverse momen-  
 2105 tum ratio,  $\frac{q}{p_T}$ , while for electrons and taus it is the energy,  $E$ . For both quantities, the  
 2106 ‘reconstructed’ value is as follows:

$$E_{reco} = E_{truth} + G(0, \Delta E)$$

$$\left(\frac{q}{p_T}\right)_{reco} = \left(\frac{q}{p_T}\right)_{truth} + G\left(0, \Delta\left(\frac{q}{p_T}\right)\right) \quad (8.2.1)$$

2107 Here,  $\Delta E$  and  $\Delta\frac{q}{p_T}$  denote the resolutions on the respective quantity. The reconstructed  
 2108 muon transverse momentum is then given by  $p_T^{reco} = \left|\left(\frac{q}{p_T}\right)_{reco}^{-1}\right|$ , while for electrons and  
 2109 taus it is given by  $p_T^{reco} = p_T^{truth} \times \frac{E_{reco}}{E_{truth}}$ .

2110

2111 The charge-flip probability for electrons is parameterised in  $\eta$  and differs slightly for the  
 2112 three ID working points, as can be seen in Figure A.1. The charge-flip probability is deter-  
 2113 mined by the tightest working point which is passed by the electron. A charge-flip occurs  
 2114 if the following condition is satisfied;  $R(0, 1) < P(e_{truth}^\pm \rightarrow e_{reco}^\mp)$ . For muons, particularly  
 2115 high- $p_T$  or  $\eta$  muons, can undergo a charge flip when the  $\frac{q}{p_T}$  is smeared.

2116

2117 Finally, electrons being misreconstructed as a photons is simulated through a parame-  
 2118 terisation in  $\eta$ . For electrons with a  $p_T > 20$  GeV, the probability of an electron being  
 2119 reconstructed as a photon is 2% for electrons with  $|\eta| < 1.37$  and is 5% for electrons with  
 2120  $|\eta| > 1.52$ . An electron is misreconstructed as a photon if  $R(0, 1) < P(e \rightarrow \gamma)$ .

## 2121 Jets and flavour tagging

2122 To simulate jet reconstruction, the first step of the detector simulation process is to smear  
 2123 the jet energy and  $p_T$ . The jet  $p_T$  is smeared by a multiplicative factor,  $G(1, \Delta E)$ , where  
 2124  $\Delta E$  represents the relative jet energy resolution determined from the parameterisation  
 2125 shown in Figure A.3a. The jet energy is smeared by multiplying the true jet energy by  
 2126  $\frac{p_T^{smeared}}{p_T^{truth}}$ .

2127

2128 Jet flavour-tagging, in particular the tagging of jets originating from  $b$ -quarks, is of great  
 2129 importance to the study described in this chapter. The  $b$ -tagging working point used in  
 2130 this study has a  $b$ -tagging efficiency  $\epsilon_b = 70\%$ , which has much-improved light-jet rejection  
 2131 compared to the  $\epsilon_b = 85\%$  working point. The flavour-tag efficiency,  $\epsilon_{ftag}^b$ , is parameterised  
 2132 in jet  $p_T$  and  $\eta$ , and can be seen in Figure A.3b. Jets which have originated from a  $b$ -quark  
 2133 at truth-level are  $b$ -tagged if  $R(0, 1) < \epsilon_{ftag}^b$ . The misreconstruction of jets as electrons,  
 2134 taus and photons is simulated by parameterising the so-called ‘fake rate’. This is rate at

2135 which an object is misreconstructed as another object.

2136  $E_T^{\text{miss}}$

2137 Smearing the  $E_T^{\text{miss}}$  requires two steps. At truth-level, the missing transverse energy,  
 2138  $E_{T, \text{truth}}^{\text{miss}}$ , is the sum of the transverse energies of all neutral particles in the event; in this  
 2139 study, only neutrinos and neutralinos contribute.

2140 To account for mismeasurement due to pileup,  $E_{T, \text{truth}}^{\text{miss}}$  is smeared by adding an addi-  
 2141 tional term,  $E_{T, \text{pileup}}^{\text{miss}}$ , drawn randomly from the distribution shown in Figure A.4a. The  
 2142  $E_T^{\text{miss}}$  resolution,  $\Delta E_T$ , is then determined from the parameterisation shown in Figure  
 2143 A.4b, using the sum of the neutral particle and pileup  $E_T^{\text{miss}}$  components as an input. The  
 2144 final  $E_T^{\text{miss}}$  is then give as:

$$E_T = E_{T, \text{truth}}^{\text{miss}} + G(0, \Delta E_T) \quad (8.2.2)$$

## 2145 Kinematic distribution comparison

2146 The effects of the detector simulation described in this section can be see in Figure 8.2.  
 2147 The ‘truth-level’  $t\bar{t}$  distribution includes no detector effects, the ‘truth-level with smearing’  
 2148  $t\bar{t}$  distributions include the detector simulation described in this section, while the ‘reco-  
 2149 level’ sample is reconstructed using the full ATLAS detector simulation.

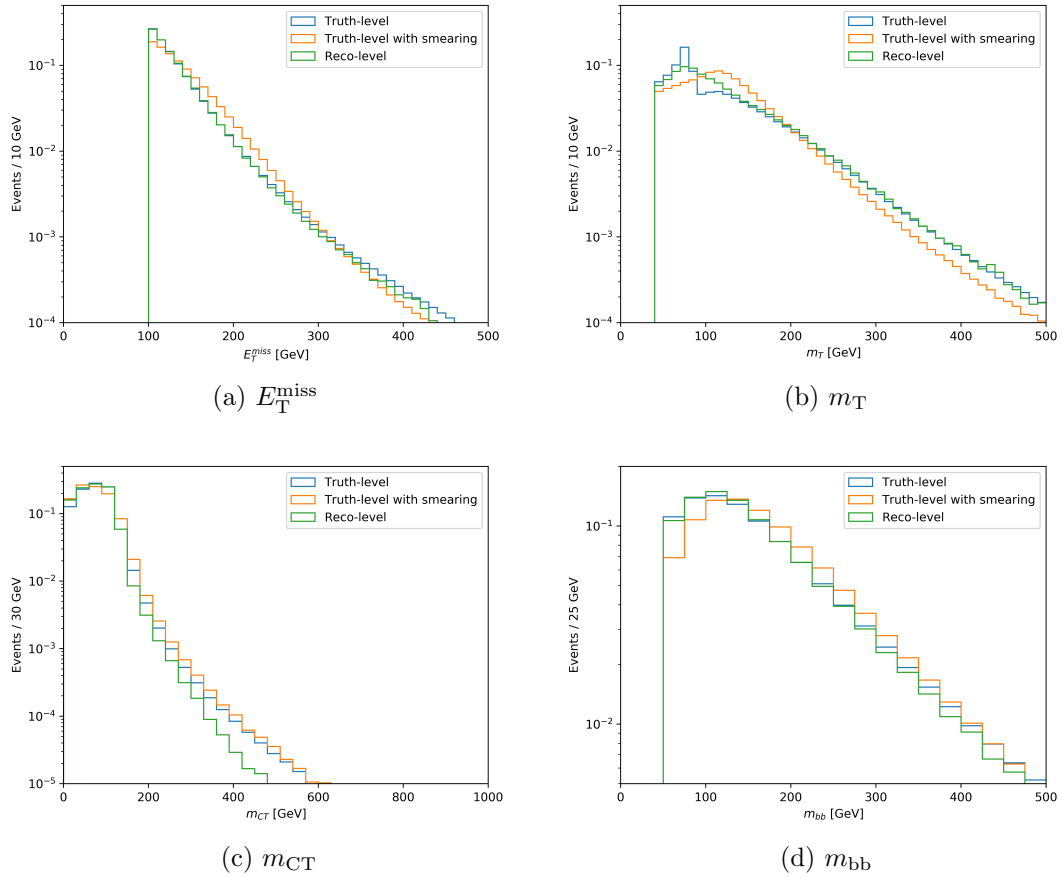


Figure 8.2: The  $E_T^{\text{miss}}$ ,  $m_T$ ,  $m_{CT}$  and  $m_{bb}$  distributions at truth-level, truth-level with the detector smearing described in this section, and a fully reconstructed samples. All distributions are normalised to unity to compare only the shape of the distributions and not normalisations.

### 2150 8.3 Event selection

2151 The object definitions used to reconstruct the leptons and jets are summarised in Table  
 2152 8.2 and Table 8.3, respectively.

	Electrons	Muons
$p_T$	25 GeV	25 GeV
$ \eta $	$< 2.47$	$< 2.7$
ID	Tight	Medium

Table 8.2: A summary of the object definitions for leptons in the HL-LHC projection.

2153 Similarly to the  $36.1\text{fb}^{-1}$  analysis described in Chapter 6, a number of preliminary  
 2154 selections are applied to select events with the single lepton, two  $b$ -jet topology, as shown  
 2155 in Table 8.4.

	jets	$b$ -jets
$p_T$	25 GeV	25 GeV
$ \eta $	$< 2.5$	$< 2.5$
Jet radius (R)	0.4	0.4
$b$ -tagging WP	-	70%

Table 8.3: A summary of the object definitions for jets in the HL-LHC projection.

Preselection	
Leptons ( $p_T \geq 25$ GeV)	1e or 1 $\mu$
Jets ( $p_T \geq 25$ GeV)	2 or 3
$b$ -jets ( $p_T \geq 25$ GeV)	2
$m_T$	$\geq 40$ GeV
$m_{bb}$	$\geq 50$ GeV
$E_T^{\text{miss}}$	$\geq 200$ GeV

Table 8.4: A summary of the preliminary selections used for for the HL-LHC projection.

2156 The loose cuts on  $m_T$  and  $m_{bb}$  are employed to combat MC mismodelling seen in the  
 2157 analysis described in Chapter ??, while the cut on  $E_T^{\text{miss}}$  is used to both reduce the SM  
 2158 background and target events containing two  $\tilde{\chi}_1^0$  in the final state.

2159

2160 Events passing the preliminary selections listed in Table 8.4 are used as inputs to Boosted  
 2161 Decision Tree (BDT) classifiers. The BDTs are implemented in Toolkit for Multivariate  
 2162 Data Analysis [28]. In this study, binary classification is performed such that the output  
 2163 of the BDT is a single value  $\in [-1, 1]$ . The key discriminatory variables which are given to  
 2164 the BDT classifiers as inputs are the  $E_T^{\text{miss}}$ ,  $m_T$ ,  $m_{CT}$ ,  $m_{bb}$  and  $\Delta R(b_1, b_2)$ . Along with  
 2165 these, the transverse momentum of the lepton and the two  $b$ -jets are useful for background  
 2166 rejection. The distributions of  $E_T^{\text{miss}}$ ,  $m_T$  and  $\Delta R(b_1, b_2)$  for the signal are highly depen-  
 2167 dent upon the mass and the mass difference of the  $\tilde{\chi}_1^\pm/\tilde{\chi}_2^0$  and  $\tilde{\chi}_1^0$ , and as such having one  
 2168 classifier which performs equally well across the entire phase space is extremely difficult  
 2169 to achieve. To aid in this, three BDT classifiers are trained, targeting ‘low’, ‘intermediate’  
 2170 and ‘high’ mass-splittings,  $\Delta M = m(\tilde{\chi}_1^\pm/\tilde{\chi}_2^0) - m(\tilde{\chi}_1^0)$ . SR-Low targets  $\Delta M < 300$  GeV,  
 2171 SR-Med targets  $\Delta M \in [300, 600]$  GeV and SR-High targets  $\Delta M > 600$  GeV. The signal  
 2172 grid, highlighted with the three targeted regions, is shown in Figure 8.3.

2173

2174 Due to the limited number of MC events in each individual signal sample, all signal  
 2175 samples in each mass-splitting regime (‘low’, ‘intermediate’ or ‘high’  $\Delta M$ ) are summed  
 2176 together with an equal weight of 1. The sum of signals for each mass-splitting region  
 2177 provide a high-statistics signal sample on which to train the BDTs, with kinematic dis-  
 tributions representing a ‘pseudo-average’ of the individual signal samples. A benchmark

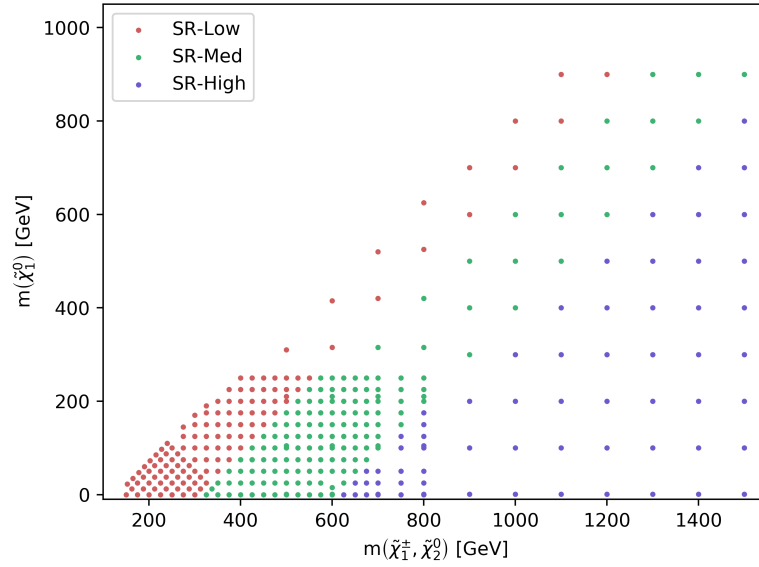
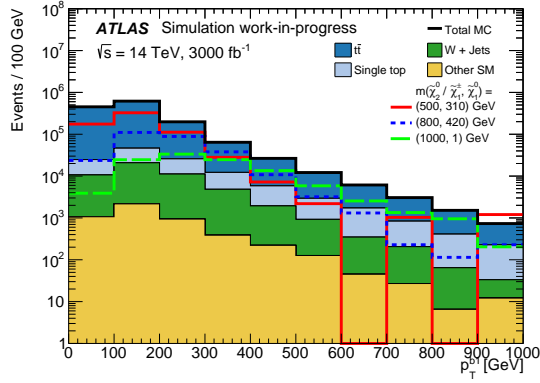
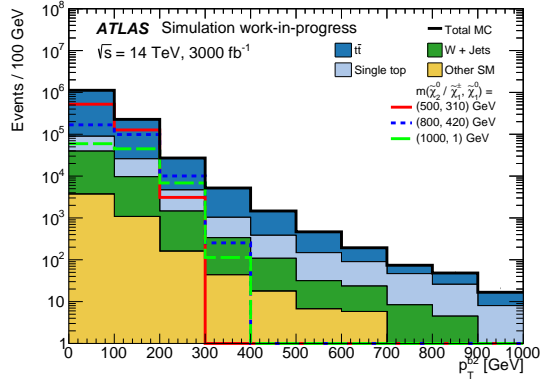
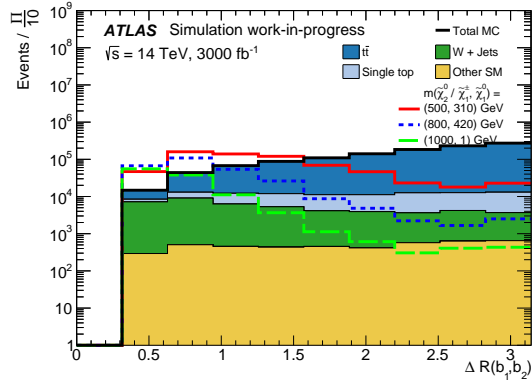
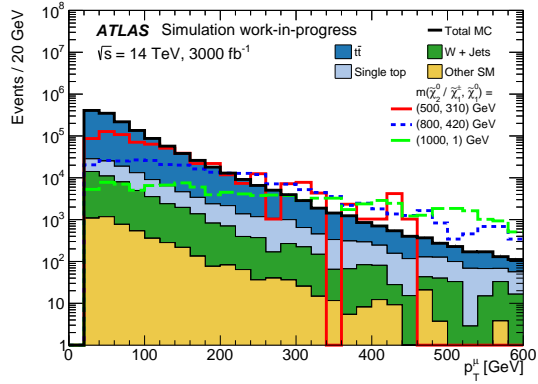
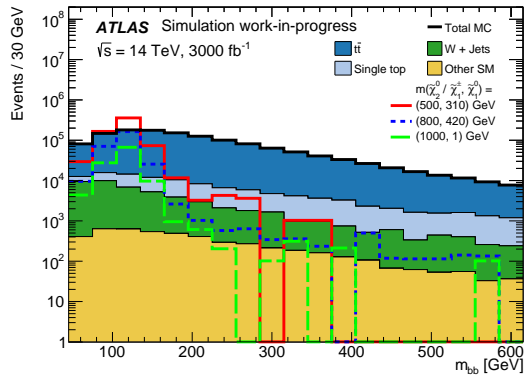
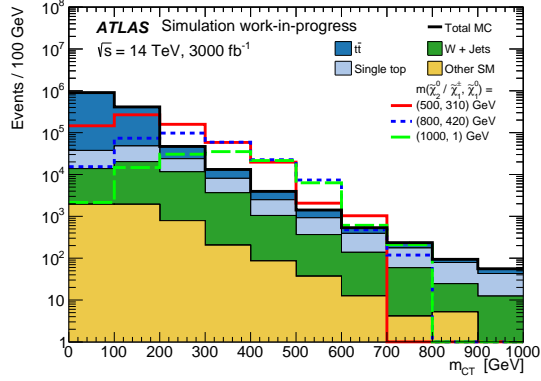


Figure 8.3: Plot showing the separation of the mass plane into the three defined categories.

2178 signal is chosen from each mass-splitting region for the purposes of comparing the kine-  
 2179 matic distributions of signal and background, and for later deriving an optimal cut on the  
 2180 BDT output. The kinematic distributions forming inputs to the BDTs are shown, with  
 2181 benchmark signals overlaid, in Figure 8.4.

(a)  $p_T^{b1}$ (b)  $p_T^{b2}$ (c)  $\Delta R(b_1, b_2)$ (d)  $p_T^{l1}$ (e)  $m_{bb}$ (f)  $m_{CT}$

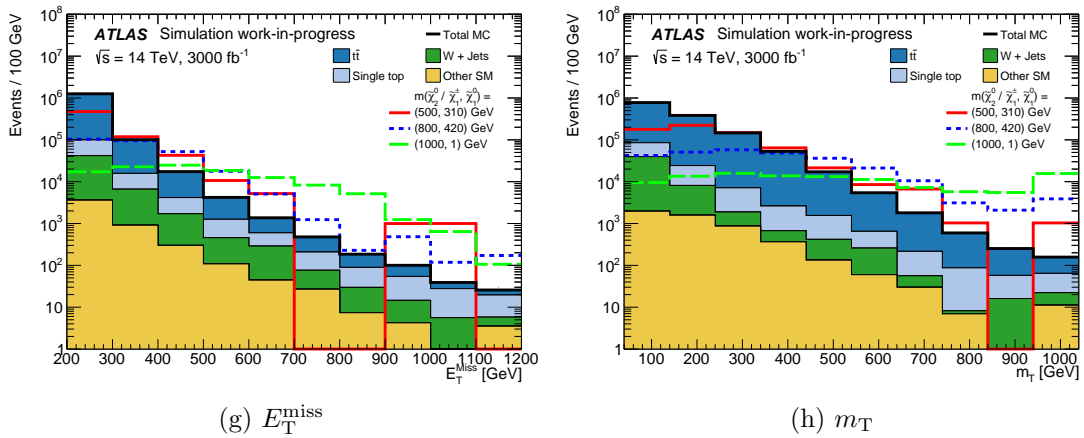


Figure 8.4: Kinematic and angular distributions for the BDT input variables at the preselection-level.

2182 The estimate for signal and background yields in the SRs is obtained by placing a cut  
 2183 on the output of the BDTs. The optimal cut value is derived by scanning over the BDT  
 2184 output with an increasing lower bound, and calculating the binomial significance,  $Z_n$ , for  
 2185 that region's benchmark model and the SM background. The optimal cuts are shown in  
 2186 Table 8.5.

SR	Signal benchmark $m(\tilde{\chi}_1^\pm / \tilde{\chi}_2^0, \tilde{\chi}_1^0)$ [GeV]	BDT range
SR-M1	(500, 310)	$> 0.25$
SR-M2	(800, 420)	$> 0.35$
SR-M3	(1000, 1)	$> 0.30$

Table 8.5: Benchmark signal models and the corresponding optimised BDT output cut, derived by maximising the binomial significance,  $Z_n$  of the benchmark signal over the SM background.

2187 The BDT output distributions for the SM backgrounds and the benchmark signal point  
 2188 for each region is shown in Figure 8.5. The arrows in these plots show the cut placed on  
 2189 the BDT output.

## 2190 8.4 Systematic uncertainties

2191 A joint strategy between the ATLAS and CMS collaborations was adopted for estimat-  
 2192 ing systematic uncertaines for HL-LHC projection studies. For analyses with an existing  
 2193 Run-2 analysis, a prescription for extrapolating the current systematic uncertainties to  
 2194  $3000 \text{ fb}^{-1}$ , where theoretical modelling uncertainties are expected to be half their current  
 2195 value. The extrapolation method for experimental uncertainties depend upon the system-

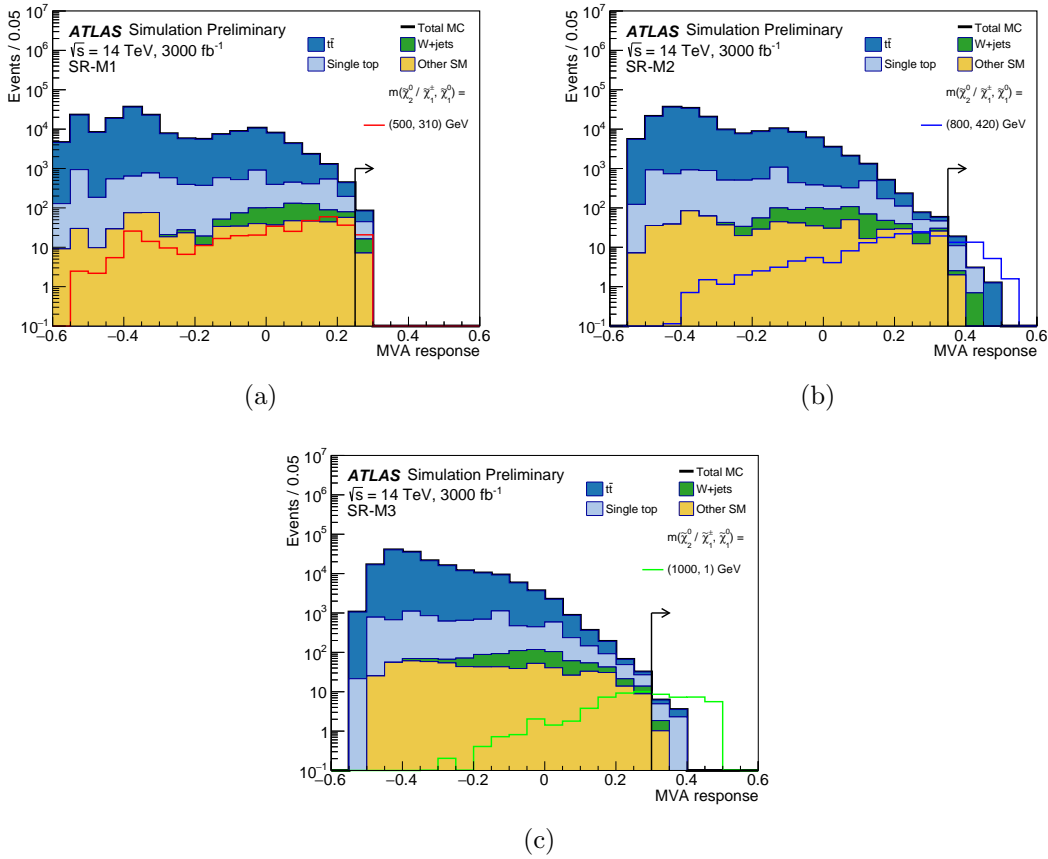


Figure 8.5: BDT outputs for HL-LHC projection. The arrow on each plot shows the cut placed on the BDT output, defining the SR.

2196 atic under consideration and are provided as multiplicative factors which are applied to  
 2197 the Run-2 systematic uncertainties.

2198

2199 In this study, the systematics from the Run-2 analysis described in Chapter ?? are ex-  
 2200 trapolated from SR1Lbb-High, which is the signal region most kinematically similar to  
 2201 the regions presented in this analysis. The Run-4 extrapolated uncertainties are shown in  
 2202 Table 8.6.

SR1Lbb-High	
JET_JER_SINGLE_NP	10.30%
Wt-Interference	8.10%
ttbar-PS	6.40%
ttbar-Generator	5.50%
ttbar-Rad	5.00%
Wt-PS	4.50%
Wt-Rad	3.30%
JET_GroupedNP_2	2.90%
JET_GroupedNP_1	2.60%
MET_SoftTrk_Scale	2.00%
Wt-Generator	1.80%
EG_RESOLUTION_ALL	1.70%
JET_GroupedNP_3	1.10%
FT_EFF_B_systematics	0.98%
FT_EFF_C_systematics	0.97%
FT_EFF_Light_systematics	0.70%
MET_SoftTrk_ResoPara	0.45%
MET_SoftTrk_ResoPerp	0.42%
FT_EFF_extrapolation_from_charm	0.41%
EG_SCALE_ALL	0.36%
FT_EFF_extrapolation	0.18%
Pileup	0.17%
MUONS_ID	0.12%
JET_EtaIntercalibration_NonClosure	0.00%
EF_EFF	0.00%
MUONS_MS	0.00%
MUON_EFF_SYS	0.00%
Quadratic sum	18.13%

Table 8.6: A table showing the extrapolated systematic uncertainties based upon the Run-2 analysis.

## 2203 8.5 Results

2204 The yields after the BDT cuts shown in Table 8.5 are shown below in Table 8.7. Entries  
 2205 denoted by ‘-’ indicate there were no events of that particular process in the corresponding  
 2206 region. Figure 8.6 shows the 95% CL exclusion limit for this channel, as well as the  $5\sigma$

Processes	SR-M1	SR-M2	SR-M3
$t\bar{t}$	$38.9 \pm 8.4$	$8.7 \pm 3.3$	$2.5 \pm 1.8$
single top	$28.3 \pm 4.8$	$10.7 \pm 3.2$	$5.4 \pm 2.5$
W+jets	$22.2 \pm 5.4$	$3.0 \pm 2.0$	$2.0 \pm 1.8$
$t\bar{t}V$	$5.1 \pm 2.4$	$2.0 \pm 1.4$	$1.0 \pm 1.0$
Diboson	$2.0 \pm 2.0$	-	-
total background	$96.5 \pm 11.8$	$24.4 \pm 5.2$	$10.9 \pm 3.4$
$m(\tilde{\chi}_1^\pm/\tilde{\chi}_2^0, \tilde{\chi}_1^0) = (500, 300)$ GeV	$20.7 \pm 4.8$	$4.6 \pm 2.3$	$1.0 \pm 1.0$
$m(\tilde{\chi}_1^\pm/\tilde{\chi}_2^0, \tilde{\chi}_1^0) = (800, 420)$ GeV	$44.3 \pm 2.3$	$33.6 \pm 2.0$	$21.2 \pm 1.6$
$m(\tilde{\chi}_1^\pm/\tilde{\chi}_2^0, \tilde{\chi}_1^0) = (1000, 1)$ GeV	$32.2 \pm 1.8$	$31.9 \pm 1.8$	$28.9 \pm 1.7$

Table 8.7: Expected signal and background yields. The errors are statistical uncertainties. Entries marked – indicate a negligible background contribution.

2207 discovery potential. The three signal regions are combined by taking the best expected  
 2208 sensitivity for each signal point. The systematics band, represented by the yellow area  
 2209 around the 95% CL exclusion line includes the extrapolated experimental and modelling  
 2210 systematics on the SM backgrounds, as well as the statistical uncertainty on all MC sam-  
 ples.

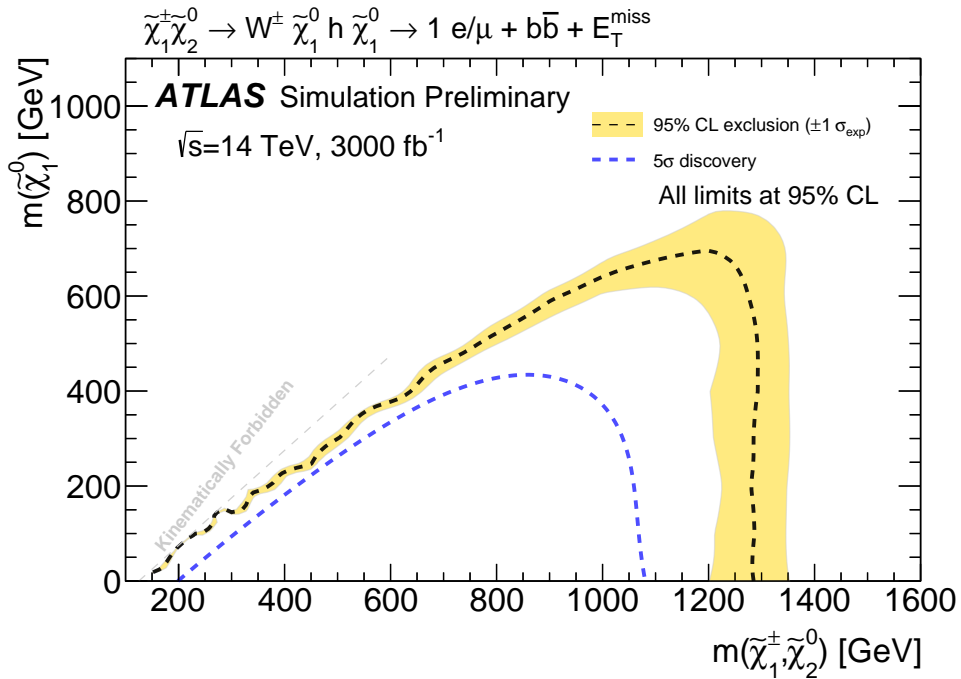


Figure 8.6: 95% CL exclusion limit and  $5\sigma$  discovery limit for the analysis presented in this chapter.

2211

2212

2213 As shown in Figure 8.6, it is expected that this channel can be excluded upto 1280 GeV,  
2214 while there is discovery potential upto 1070 GeV. This far exceeds the exclusion limits at  
2215 the end of Run-2, with results shown in Chapter 6 for both  $36.1\text{fb}^{-1}$  and  $139\text{fb}^{-1}$ . During  
2216 this analysis, studies were performed using a both a conventional cut-based analysis and  
2217 also using a deep neural network to perform binary classification of signal and background.  
2218 These studies are included in Appendix A.



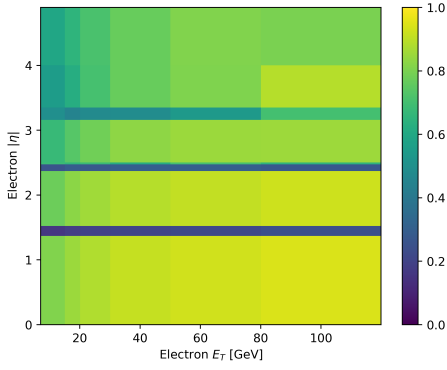
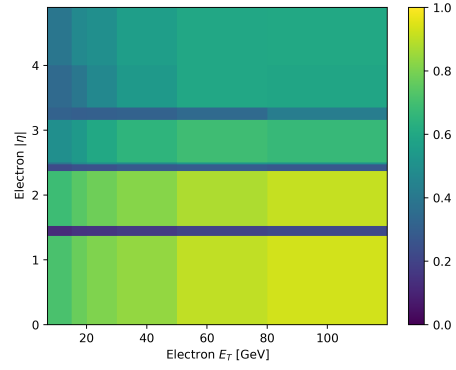
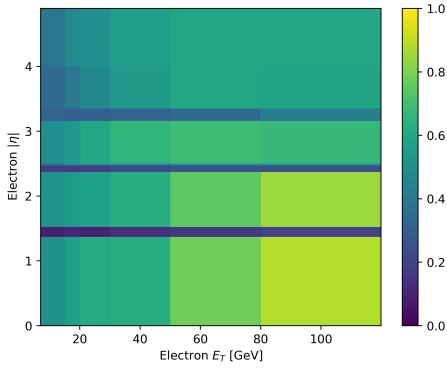
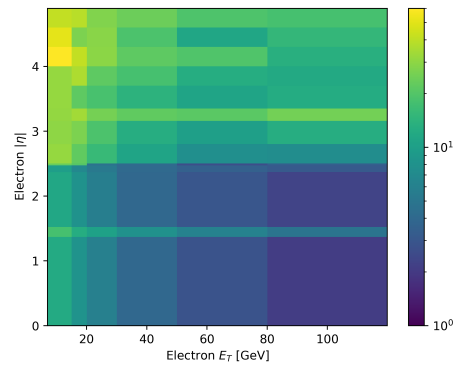
## 2219 **Appendix A**

# 2220 **Sensitivity to $\tilde{\chi}_1^\pm \tilde{\chi}_2^0$ pair-production** 2221 **at the HL-LHC**

2222 The first part of this appendix is dedicated to documenting the detector simulation pa-  
2223 rameterisations detailed in Chapter 8.

### 2224 **A.1 Detector simulation parameterisations**

#### 2225 **Electrons**


 (a)  $\epsilon_{rec}$  for 'loose' electron working point.

 (b)  $\epsilon_{rec}$  for 'medium' electron working point.

 (c)  $\epsilon_{rec}$  for 'tight' electron working point.


(d) Electron energy resolution (MeV).

Figure A.1: Electron ID efficiencies, energy resolution and charge-flip probability for the prospects study presented in Chapter 8. The

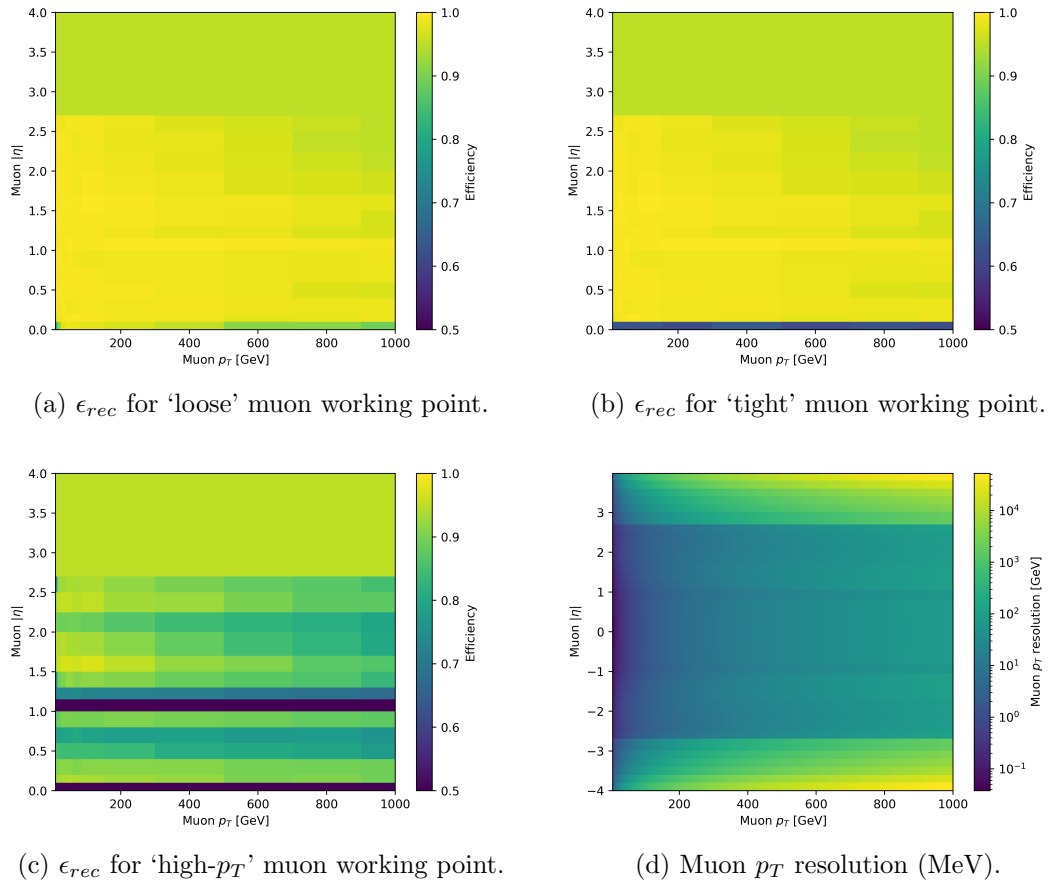


Figure A.2: Muon ID efficiencies and  $p_T$  resolution for the prospects study presented in Chapter 8. The

2227 **Taus**

2228 **Jets**

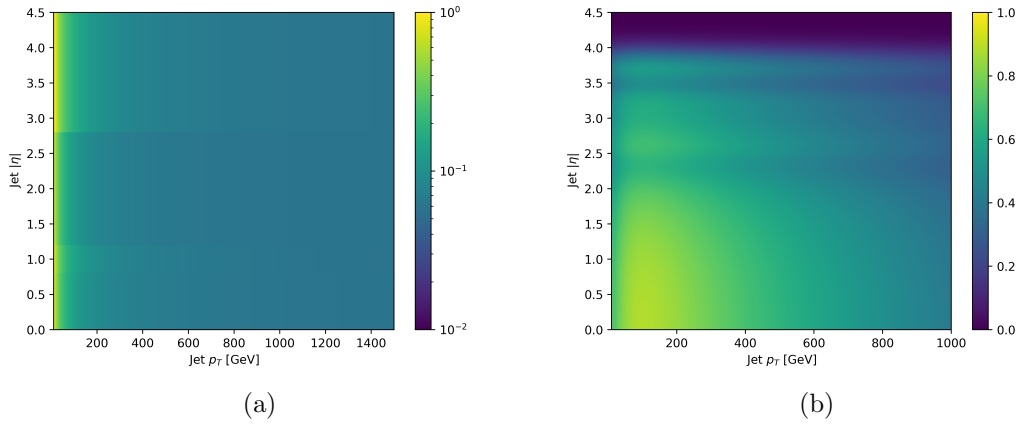


Figure A.3: Parameterised relative jet energy resolution, shown in Figure A.3a, and parameterised  $b$ -tagging efficiency, shown in Figure A.3b, used in the HL-LHC detector simulation.

2229  $E_T^{\text{miss}}$

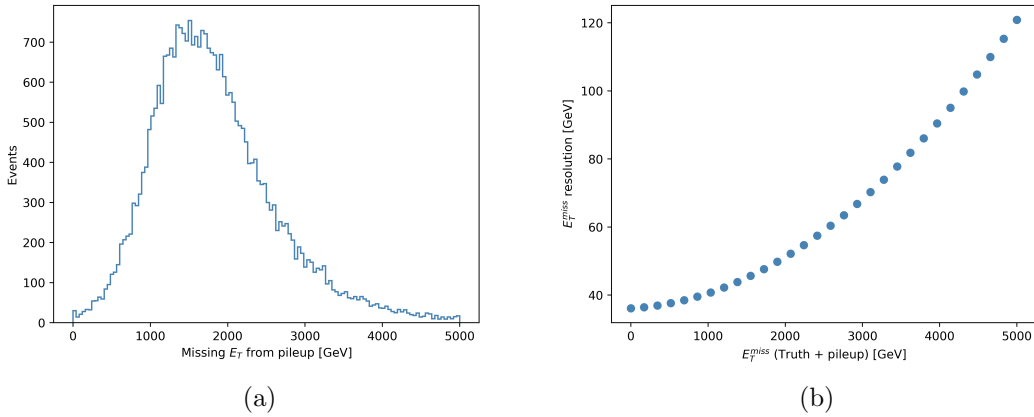


Figure A.4: Parameterised  $E_T^{\text{miss}}$  distribution from pileup, shown in Figure A.4a, and parameterised  $E_T^{\text{miss}}$  resolution, shown in Figure A.4b, used in the HL-LHC detector simulation.

## 2230 A.2 Cut & count studies

2231 A reoptimisation of the signal regions defined in Table 6.3 was performed to compare the  
 2232 potential sensitivity of the conventional analysis to the multivariate analysis described in  
 2233 Chapter 8. During the reoptimisation, the selections on the  $m_{bb}$  and  $m_{CT}$  variables are  
 2234 unchanged from Table 6.3. A scan over the lower bound of the  $m_T$  and  $E_T^{miss}$  variables  
 2235 was performed in steps of 10 GeV, with no upper bound. The lack of an upper bound on  
 2236 these variables means the regions are able to overlap, and therefore lose their orthogonal-  
 2237 ity. However, as the final fit result takes the best expected sensitivity for each point, the  
 2238 orthogonality of signal regions is not required. The cuts maximising the binomial signif-  
 2239 icance,  $Z_n$ , for the benchmark signal points shown in Table 8.5 are chosen for the three  
 signal regions. These cuts are summarised in Table A.1. The sensitivity to each signal

	SRLM	SRMM	SRHM
$m_{bb}$	$\in [105, 135]$		
$m_{CT}$	$> 160$		
$E_T^{miss}$	$> 320$	$> 380$	$> 420$
$m_T$	$> 180$	$> 280$	$> 280$

Table A.1: Reoptimised signal region selections for conventional analysis in order to compare sensitivity with the multivariate analysis described in Chapter 8. All cuts are in units of GeV.

2240  
 2241 point is assessed by calculating the binomial significance,  $Z_n$ , for each signal point in all  
 2242 three signal regions, and the combination of the regions takes the best expected significance  
 2243 for each point. The expected sensitivities can be seen in Figure A.5.

## 2244 A.3 Deep learning studies

2245 In addition to the the reoptimisation of the signal regions, described in the previous section,  
 2246 a study of the expected sensitivity using a DNN as a binary classifier was undertaken. A  
 2247 diagram of the DNN used in this study is shown in Figure A.6, and the model itself is  
 2248 implemented using Keras and Tensorflow. The inputs to the classifier are the same as  
 2249 described in Chapter 8 for the BDT analysis, and the same procedure for separating the  
 2250 signal samples into three sets targetting different mass-splitting regimes is also the same.  
 2251 The DNN is trained on a GPU for a maximum of 10000 epochs, or until the accuracy of the  
 2252 classifier, evaluated using test data, has not improved in 2 epochs. To avoid overtraining,  
 2253 a dropout of 20% is used, such that upto 20% of the inputs to each layer can be ignored, at  
 2254 random, in each training epoch. Similarly to the BDT analysis described in Chapter 8, 3  
 2255 classifiers are trained, one per mass-splitting region. The signal-background discrimination  
 2256 can be seen in Figure A.7.

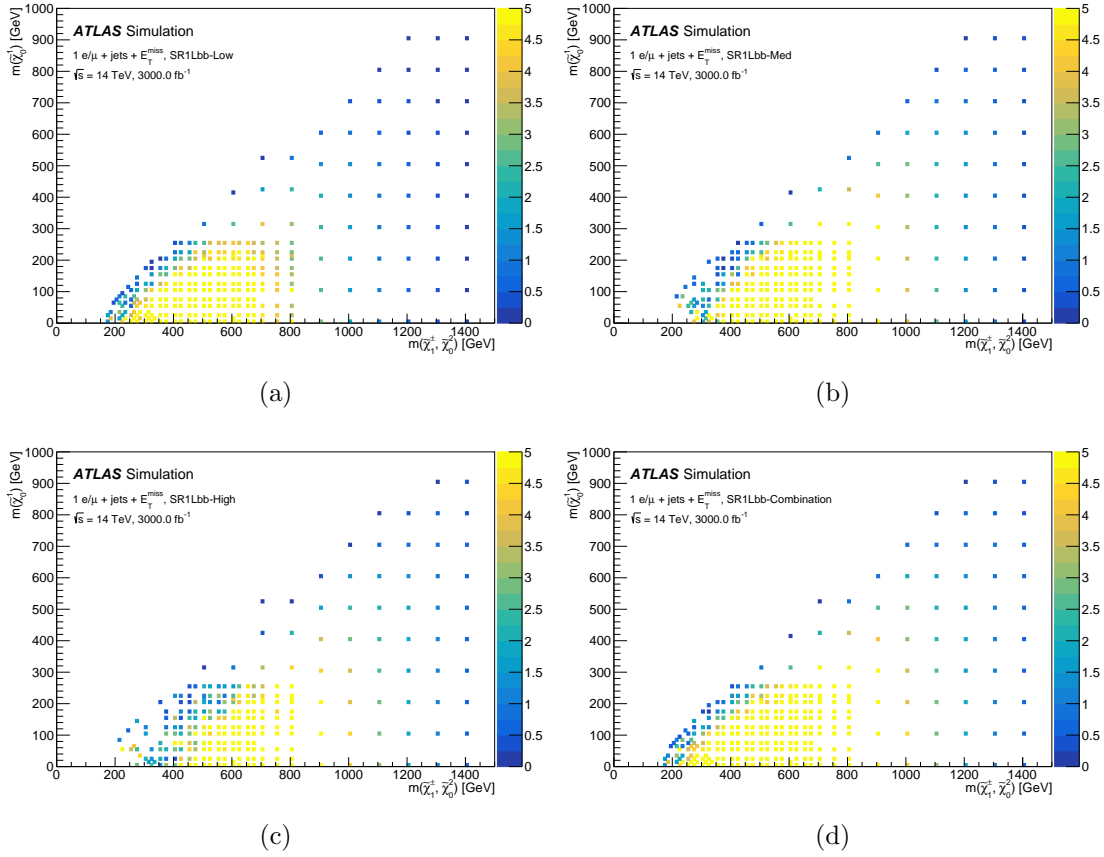
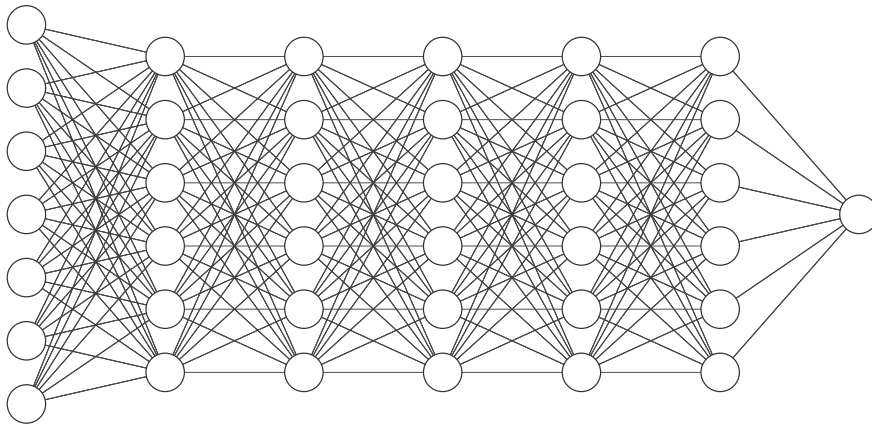


Figure A.5: Plots showing the binomial significance,  $Z_n$ , of each signal point in the reoptimised SRMLM (A.5a), SRMM (A.5b), SRHM (A.5c), and the best expected combination (A.5d). All plots are produced assuming a total 15% background uncertainty.



Input Layer  $\in \mathbb{R}^7$  Hidden Layer  $\in \mathbb{R}^6$  Hidden Layer  $\in \mathbb{R}^6$  Hidden Layer  $\in \mathbb{R}^6$  Hidden Layer  $\in \mathbb{R}^6$  Output Layer  $\in \mathbb{R}^1$

Figure A.6: A diagram showing the structure of the fully-connected Deep Neural Network tested as a binary classifier in the HL-LHC sensitivity study.

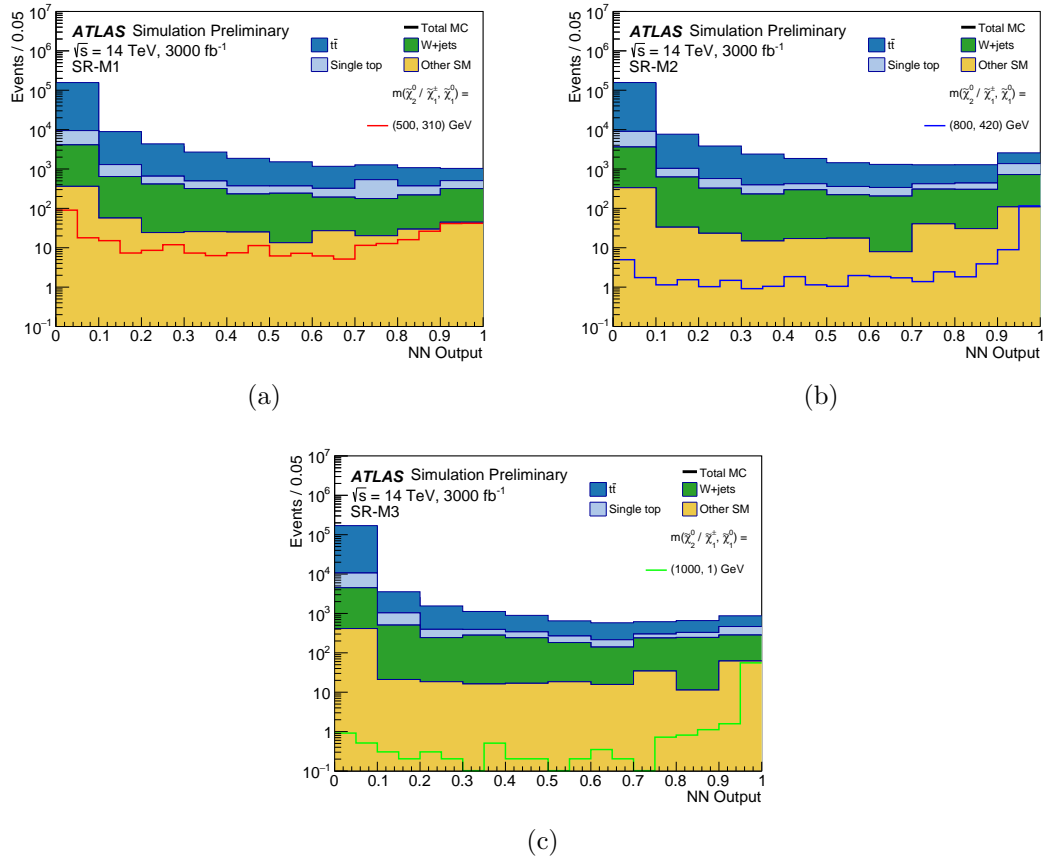


Figure A.7: Outputs for each of the DNN classifiers trained on the signal ensemble of each region and the dominant  $t\bar{t}$  background.

2257 The shape and range of the output of the DNN classifiers is due to the use of the  
 2258 sigmoid/softmax activation on the output layer of the classifier, while TMVA performs a  
 2259 transformation of the form  $y(x) = -\frac{1}{15} \left(\frac{1}{x} - 1\right)$  on the output of the classifier [28]. The  
 2260 DNN classifiers were not used in the final analysis as the sensitivity to the signal using a  
 2261 cut on the output of the DNN classifiers is much lower than for the BDT classifiers. While  
 2262 these studies were not performed due to time and resource constraints, it is expected that  
 2263 with larger MC statistics for the signal samples, fine-tuning of the DNN hyperparameters,  
 2264 and performing multi-class classification instead of binary classification, the DNN could  
 2265 achieve superior classification performance over the BDT classifiers.

#### 2266 A.4 Extending $W$ +jets sample statistics

2267 After applying all selections listed in Table 8.4 and the cuts on the BDT output listed  
 2268 in Table 8.5, the MC statistics in the  $W$ +jets sample was extremely low, such that the  
 2269 MC statistical uncertainty was  $\sim 100\%$ . For the final statistical analysis, a procedure was  
 2270 developed for extending the  $W$ +jets sample statistics in order to predict realistic yields and  
 2271 uncertainties. Using the detector simulation method described in Chapter 8, individual  
 2272 events in the nominal  $W$ +jets samples were smeared  $N = 10$  times, to produce an extended  
 2273 sample with  $\leq N$  times the input sample statistics. Due to the significant computing time  
 2274 of running this procedure, only  $B$ -filtered slices of the  $W$ +jets MC with  $W \rightarrow e\nu/\mu\nu$  were  
 2275 used as the input for this procedure. A plot comparing the shape of the  $E_T^{miss}$  distribution  
 2276 for the nominal  $B$ -filtered samples with electrons, muons and taus and extended samples  
 2277 for  $B$ -filtered samples with electrons and muons is shown in Figure A.8.

2278 The normalisation of the extended sample is corrected for the multiple smearing method  
 2279 by weighting each event by a factor  $\frac{1}{N}$ , and corrected for the missing  $W \rightarrow \ell\nu$  slices by  
 2280 multiplying the expected yield of the extended sample by  $N_{MC}^{nominal}/N_{MC}^{extended}$  evaluated at  
 2281 preselection level. The correction factor for the missing MC slices was found to be 1.21.

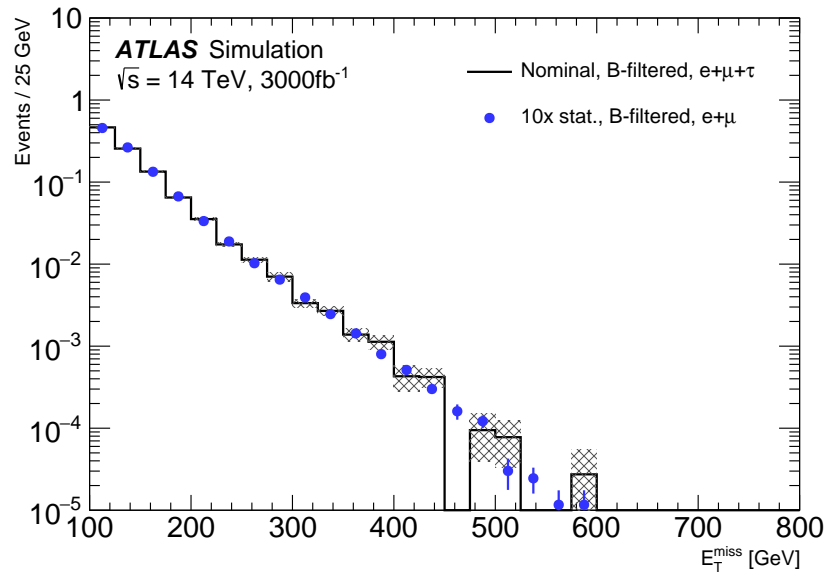


Figure A.8: A comparison of the  $E_T^{\text{miss}}$  distributions at preselection level for the nominal  $W$ +jets sample and the sample with extended MC statistics from the multiple event smearing method described in this section.

## 2282 Appendix B

# 2283 Testbeam studies of FE-I4 and 2284 RD53A performance at HL-LHC

2285 The Run-2 period of data taking concluded in 2018, with ATLAS having recorded a dataset  
2286 totalling  $139 \text{ fb}^{-1}$ , making way for the start of Long Shutdown 2 (LS2). With LS2 comes  
2287 the start of preparations for the next phase of the scientific programme of the LHC and  
2288 ATLAS, the High-Luminosity phase. The High-Luminosity LHC (HL-LHC) will begin run-  
2289 ning in the mid-2020s, bringing instantaneous luminosities around 5 times higher than in  
2290 Run-2, reaching  $7.5 \times 10^{34} \text{ cm}^{-2}\text{s}^{-1}$  at  $\sqrt{s} = 14 \text{ TeV}$ . The total integrated luminosity to be  
2291 recorded by ATLAS during this period is expected to total 3000-4000  $\text{fb}^{-1}$ . Both the LHC  
2292 and ATLAS will undergo numerous upgrades to prepare for the HL-LHC operations phase.

2293  
2294 The first set of upgrades to the ATLAS detector, known as the Phase I upgrades, will take  
2295 place in Long Shutdown 2 (LS2), between 2019-2021. The New Small Wheel (NSW) [59]  
2296 will replace the current muon end-cap system, providing precision tracking and triggering  
2297 capabilities. In addition, upgrades will be made to the electronics of the LAr calorimeter  
2298 system, providing higher-granularity information to the L1 trigger [60].

2299  
2300 Following the completion of Run-3 of LHC operations, both ATLAS and LHC will go  
2301 into Long Shutdown 3 (LS3). During the High-Luminosity LHC (HL-LHC) phase, the  
2302 instantaneous luminosity is estimated to result in an average of 200 inelastic  $pp$  collisions  
2303 in each bunch-crossing, with bunch-crossings occurring every 25 ns. This instantaneous  
2304 luminosity far exceeds the design of the ATLAS detector described in Chapter 2. The  
2305 increase in luminosity will render the current ID of the ATLAS detector inoperable, and  
2306 hence a new tracker will be installed, known as the ATLAS Inner Tracker (ITk). The ITk  
2307 will be constructed using only silicon pixel and strip modules, as these technologies are  
2308 suited for high-occupancy, high-radiation environments. This Appendix documents studies  
2309 performed on the performance of pixel modules for the upcoming ATLAS Inner Tracker

2310 (ITk) upgrade.

2311 **B.1 ATLAS ITk upgrade**

2312 **B.2 Experimental setup**

2313 **B.3**

2314

# Bibliography

- 2315 [1] G. Aad, T. Abajyan, B. Abbott, J. Abdallah, S. Abdel Khalek, A.A. Abdelalim,  
2316 O. Abdinov, R. Aben, B. Abi, M. Abolins, and et al. Observation of a new particle  
2317 in the search for the standard model higgs boson with the atlas detector at the lhc.  
2318 *Physics Letters B*, 716(1):1–29, Sep 2012.
- 2319 [2] S. Chatrchyan, V. Khachatryan, A.M. Sirunyan, A. Tumasyan, W. Adam, E. Aguilo,  
2320 T. Bergauer, M. Dragicevic, J. Erö, C. Fabjan, and et al. Observation of a new  
2321 boson at a mass of 125 gev with the cms experiment at the lhc. *Physics Letters B*,  
2322 716(1):30–61, Sep 2012.
- 2323 [3] M. Tanabashi et al. Review of Particle Physics. *Phys. Rev.*, D98(3):030001, 2018.
- 2324 [4] William Martin McClain. *Axioms of group theory*, pages 55–58. Springer New York,  
2325 New York, NY, 2008.
- 2326 [5] V. Agrawal, S. M. Barr, John F. Donoghue, and D. Seckel. Viable range of the mass  
2327 scale of the standard model. *Physical Review D*, 57(9):5480–5492, May 1998.
- 2328 [6] Esma Mobs. The CERN accelerator complex. Complexe des accélérateurs du CERN.  
2329 Jul 2016. General Photo.
- 2330 [7] Werner Herr and B Muratori. Concept of luminosity. 2006.
- 2331 [8] A. Airapetian and V. et. al. Grabsky. *ATLAS detector and physics performance:*  
2332 *Technical Design Report, 1*. Technical Design Report ATLAS. CERN, Geneva, 1999.
- 2333 [9] G. Aad et al. The ATLAS Experiment at the CERN Large Hadron Collider. *JINST*,  
2334 3:S08003, 2008.
- 2335 [10] M Capeans, G Darbo, K Einsweiler, M Elsing, T Flick, M Garcia-Sciveres, C Gemme,  
2336 H Pernegger, O Rohne, and R Vuillermet. ATLAS Insertable B-Layer Technical Design  
2337 Report. Technical Report CERN-LHCC-2010-013. ATLAS-TDR-19, Sep 2010.
- 2338 [11] Richard D. Ball, Valerio Bertone, Stefano Carrazza, Christopher S. Deans, Luigi  
2339 Del Debbio, Stefano Forte, Alberto Guffanti, Nathan P. Hartland, José I. Latorre,

- 2340 and et al. Parton distributions for the lhc run ii. *Journal of High Energy Physics*,  
2341 2015(4), Apr 2015.
- 2342 [12] Stefano Frixione, Eric Laenen, Patrick Motylinski, Chris White, and Bryan R Webber.  
2343 Single-top hadroproduction in association with awboson. *Journal of High Energy*  
2344 *Physics*, 2008(07):029–029, Jul 2008.
- 2345 [13] Joao Pequenao and Paul Schaffner. How ATLAS detects particles: diagram of particle  
2346 paths in the detector. Jan 2013.
- 2347 [14] M. Aaboud, G. Aad, B. Abbott, D. C. Abbott, O. Abdinov, B. Abeloos, D. K. Ab-  
2348 hayasinghe, S. H. Abidi, O. S. AbouZeid, and et al. Electron reconstruction and  
2349 identification in the ATLAS experiment using the 2015 and 2016 LHC proton–proton  
2350 collision data at  $\sqrt{s} = 13$  TeV. *The European Physical Journal C*, 79(8), Aug 2019.
- 2351 [15] M. Aaboud, G. Aad, B. Abbott, O. Abdinov, B. Abeloos, D. K. Abhayasinghe, S. H.  
2352 Abidi, O. S. AbouZeid, N. L. Abraham, and et al. Measurement of the photon identi-  
2353 fication efficiencies with the ATLAS detector using LHC Run 2 data collected in 2015  
2354 and 2016. *The European Physical Journal C*, 79(3), Mar 2019.
- [16] G. Aad, B. Abbott, J. Abdallah, O. Abdinov, B. Abeloos, R. Aben, M. Abolins, O. S.  
AbouZeid, N. L. Abraham, and et al. Muon reconstruction performance of the atlas  
detector in proton–proton collision data at  
$$\sqrt{s}$$
  
s =13 tev. *The European Physical Journal C*, 76(5), May 2016.
- 2356 [17] Measurement of the tau lepton reconstruction and identification performance in the  
2357 ATLAS experiment using  $pp$  collisions at  $\sqrt{s} = 13$  TeV. Technical Report ATLAS-  
2358 CONF-2017-029, CERN, Geneva, May 2017.
- 2359 [18] G. Aad, B. Abbott, J. Abdallah, O. Abdinov, R. Aben, M. Abolins, O. S. AbouZeid,  
2360 H. Abramowicz, H. Abreu, and et al. Topological cell clustering in the atlas calorime-  
2361 ters and its performance in lhc run 1. *The European Physical Journal C*, 77(7), Jul  
2362 2017.
- 2363 [19] Michele Livan and Richard Wigmans. Misconceptions about calorimetry. *Instruments*,  
2364 1(1):3, May 2017.
- 2365 [20] Georges Aad et al. ATLAS b-jet identification performance and efficiency measure-  
2366 ment with  $t\bar{t}$  events in pp collisions at  $\sqrt{s} = 13$  TeV. *Eur. Phys. J. C*, 79(11):970,  
2367 2019.

- [21] M. Aaboud, G. Aad, B. Abbott, O. Abidinov, B. Abeloos, S. H. Abidi, O. S. AbouZeid, N. L. Abraham, H. Abramowicz, and et al. Search for top-squark pair production in final states with one lepton, jets, and missing transverse momentum using 36 fb

–1

of

$$\sqrt{s} = 13$$

2368     tev pp collision data with the atlas detector. *Journal of High Energy Physics*, 2018(6),  
2369     Jun 2018.

2370 [22] Daniel R Tovey. On measuring the masses of pair-produced semi-invisibly decaying  
2371     particles at hadron colliders. *Journal of High Energy Physics*, 2008(04):034–034, Apr  
2372     2008.

2373 [23] Giacomo Polesello and Daniel R. Tovey. Supersymmetric particle mass measurement  
2374     with the boost-corrected contranverse mass. *Journal of High Energy Physics*, 2010(3),  
2375     Mar 2010.

2376 [24] C.G Lester and D.J Summers. Measuring masses of semi-invisibly decaying particle  
2377     pairs produced at hadron colliders. *Physics Letters B*, 463(1):99–103, Sep 1999.

2378 [25] Partha Konar, Kyoungchul Kong, Konstantin T. Matchev, and Myeonghun Park.  
2379     Dark matter particle spectroscopy at the lhc: generalizing m t2 to asymmetric event  
2380     topologies. *Journal of High Energy Physics*, 2010(4), Apr 2010.

2381 [26] Christopher G. Lester and Benjamin Nachman. Bisection-based asymmetric m t2  
2382     computation: a higher precision calculator than existing symmetric methods. *Journal  
2383     of High Energy Physics*, 2015(3), Mar 2015.

2384 [27] William Buttinger and Michel Lefebvre. Formulae for Estimating Significance. Tech-  
2385     nical Report ATL-COM-GEN-2018-026, CERN, Geneva, Oct 2018.

2386 [28] A. Hoecker, P. Speckmayer, J. Stelzer, J. Therhaag, E. von Toerne, H. Voss,  
2387     M. Backes, T. Carli, O. Cohen, A. Christov, D. Dannheim, K. Danielowski, S. Henrot-  
2388     Versille, M. Jachowski, K. Kraszewski, A. Krasznahorkay Jr., M. Kruk, Y. Mahalalel,  
2389     R. Ospanov, X. Prudent, A. Robert, D. Schouten, F. Tegenfeldt, A. Voigt, K. Voss,  
2390     M. Wolter, and A. Zemla. Tmva - toolkit for multivariate data analysis, 2007.

2391 [29] Harris Drucker and Corinna Cortes. Boosting decision trees. In *NIPS*, 1995.

2392 [30] Yoav Freund and Robert E Schapire. A decision-theoretic generalization of on-line  
2393     learning and an application to boosting. *J. Comput. Syst. Sci.*, 55(1):119–139, August  
2394     1997.

- 2395 [31] Tianqi Chen and Carlos Guestrin. Xgboost. *Proceedings of the 22nd ACM SIGKDD*  
2396 *International Conference on Knowledge Discovery and Data Mining*, Aug 2016.
- 2397 [32] S van der Meer. Calibration of the effective beam height in the ISR. Technical Report  
2398 CERN-ISR-PO-68-31. ISR-PO-68-31, CERN, Geneva, 1968.
- [33] M. Aaboud, G. Aad, B. Abbott, J. Abdallah, O. Abdinov, B. Abeloos, R. Aben, O. S.  
AbouZeid, N. L. Abraham, and et al. Luminosity determination in pp collisions at
- $$\sqrt{s}$$
- 2399  $s = 8$  tev using the atlas detector at the lhc. *The European Physical Journal C*, 76(12),  
2400 Nov 2016.
- 2401 [34] The ATLAS Collaboration. Determination of jet calibration and energy res-  
2402 olution in proton-proton collisions at  $\sqrt{s} = 8$  TeV using the ATLAS detec-  
2403 tor. Technical Report arXiv:1910.04482, CERN, Geneva, Oct 2019. 110  
2404 pages in total, author list starting page 94, 58 figures, 7 tables, submit-  
2405 ted to Eur. Phys. J. C. All figures including auxiliary figures are available at  
2406 <https://atlas.web.cern.ch/Atlas/GROUPS/PHYSICS/PAPERS/PERF-2014-02/>.
- 2407 [35] A method for the construction of strongly reduced representations of ATLAS exper-  
2408 imental uncertainties and the application thereof to the jet energy scale. Technical  
2409 Report ATL-PHYS-PUB-2015-014, CERN, Geneva, Jul 2015.
- 2410 [36] G. Aad, T. Abajyan, B. Abbott, J. Abdallah, S. Abdel Khalek, A. A. Abdelalim,  
2411 O. Abdinov, R. Aben, B. Abi, and et al. Jet energy resolution in proton-proton  
2412 collisions at  $\sqrt{s} = 7$  TeV recorded in 2010 with the atlas detector. *The European*  
2413 *Physical Journal C*, 73(3), Mar 2013.
- [37] M. Aaboud, G. Aad, B. Abbott, O. Abdinov, B. Abeloos, S. H. Abidi, O. S. AbouZeid,  
N. L. Abraham, H. Abramowicz, and et al. Performance of missing transverse mo-  
mentum reconstruction with the atlas detector using proton–proton collisions at
- $$\sqrt{s} = 13 \text{ TeV}$$
- 2414 . *The European Physical Journal C*, 78(11), Nov 2018.
- 2415 [38] M. Baak, G. J. Besjes, D. Côté, A. Koutsman, J. Lorenz, and D. Short. Histfitter  
2416 software framework for statistical data analysis. *The European Physical Journal C*,  
2417 75(4), Apr 2015.
- 2418 [39] A L Read. Presentation of search results: theCLstechnique. *Journal of Physics G:*  
2419 *Nuclear and Particle Physics*, 28(10):2693–2704, sep 2002.

- 2420 [40] Search for dark matter associated production with a single top quark in  $\sqrt{s} = 13$  TeV  
2421 (pp) collisions with the ATLAS detector. Technical Report ATLAS-CONF-2020-034,  
2422 CERN, Geneva, Aug 2020.
- 2423 [41] Jalal Abdallah, Adi Ashkenazi, Antonio Boveia, Giorgio Busoni, Andrea De Simone,  
2424 Caterina Doglioni, Aielet Efrati, Erez Etzion, Johanna Gramling, Thomas Jacques,  
2425 Tongyan Lin, Enrico Morgante, Michele Papucci, Bjoern Penning, Antonio Walter  
2426 Riotto, Thomas Rizzo, David Salek, Steven Schramm, Oren Slone, Yotam Soreq,  
2427 Alessandro Vichi, Tomer Volansky, Itay Yavin, Ning Zhou, and Kathryn Zurek. Sim-  
2428 plified models for dark matter and missing energy searches at the lhc, 2014.
- 2429 [42] Jalal Abdallah, Henrique Araujo, Alexandre Arbey, Adi Ashkenazi, Alexander  
2430 Belyaev, Joshua Berger, Celine Boehm, Antonio Boveia, Amelia Brennan, Jim Brooke,  
2431 and et al. Simplified models for dark matter searches at the lhc. *Physics of the Dark*  
2432 *Universe*, 9-10:8–23, Sep 2015.
- 2433 [43] Daniel Abercrombie, Nural Akchurin, Ece Akilli, Juan Alcaraz Maestre, Brandon  
2434 Allen, Barbara Alvarez Gonzalez, Jeremy Andrea, Alexandre Arbey, Georges Azuelos,  
2435 Patrizia Azzi, and et al. Dark matter benchmark models for early lhc run-2 searches:  
2436 Report of the atlas/cms dark matter forum. *Physics of the Dark Universe*, 27:100371,  
2437 Jan 2020.
- 2438 [44] Priscilla Pani and Giacomo Polesello. Dark matter production in association with a  
2439 single top-quark at the lhc in a two-higgs-doublet model with a pseudoscalar mediator.  
2440 *Physics of the Dark Universe*, 21:8–15, Sep 2018.
- 2441 [45] Felix Kahlhoefer, Kai Schmidt-Hoberg, Thomas Schwetz, and Stefan Vogl. Implica-  
2442 tions of unitarity and gauge invariance for simplified dark matter models. *Journal of*  
2443 *High Energy Physics*, 2016(2), Feb 2016.
- 2444 [46] url: <http://feynrules.irmp.ucl.ac.be/wiki/DMSimp>.
- 2445 [47] Tomohiro Abe, Yoav Afik, Andreas Albert, Christopher R. Anelli, Liron Barak, Mar-  
2446 tin Bauer, J. Katharina Behr, Nicole F. Bell, Antonio Boveia, Oleg Brandt, Giorgio  
2447 Busoni, Linda M. Carpenter, Yu-Heng Chen, Caterina Doglioni, Alison Elliot, Mo-  
2448 toko Fujiwara, Marie-Helene Genest, Raffaele Gerosa, Stefania Gori, Johanna Gram-  
2449 ling, Alexander Grohsjean, Giuliano Gustavino, Kristian Hahn, Ulrich Haisch, Lars  
2450 Henkelmann, Junji Hisano, Anders Huitfeldt, Valerio Ippolito, Felix Kahlhoefer, Greg  
2451 Landsberg, Steven Lowette, Benedikt Maier, Fabio Maltoni, Margarete Muehleitner,  
2452 Jose M. No, Priscilla Pani, Giacomo Polesello, Darren D. Price, Tania Robens, Giu-  
2453 lia Rovelli, Yoram Rozen, Isaac W. Sanderson, Rui Santos, Stanislava Sevova, David  
2454 Sperka, Kevin Sung, Tim M. P. Tait, Koji Terashi, Francesca C. Ungaro, Eleni Vry-

- 2455 onidou, Shin-Shan Yu, Sau Lan Wu, and Chen Zhou. Lhc dark matter working group:  
2456 Next-generation spin-0 dark matter models, 2018.
- [48] M. Aaboud, G. Aad, B. Abbott, D. C. Abbott, O. Abdinov, D. K. Abhayasinghe, S. H.  
Abidi, O. S. AbouZeid, N. L. Abraham, and et al. Constraints on mediator-based dark  
matter and scalar dark energy models using  
$$\sqrt{s}$$
  
= 13 tev pp collision data collected by the atlas detector. *Journal of High Energy  
Physics*, 2019(5), May 2019.
- 2459 [49] Study of the double Higgs production channel  $H(\rightarrow b\bar{b})H(\rightarrow \gamma\gamma)$  with the ATLAS  
2460 experiment at the HL-LHC. Technical Report ATL-PHYS-PUB-2017-001, CERN,  
2461 Geneva, Jan 2017.
- 2462 [50] Jung Chang, Kingman Cheung, Jae Sik Lee, and Jubin Park. Probing the trilinear  
2463 Higgs boson self-coupling at the high-luminosity LHC via multivariate analysis. *Phys.  
2464 Rev. D*, 101(1):016004, 2020.
- 2465 [51] M. Cepeda et al. *Report from Working Group 2: Higgs Physics at the HL-LHC and  
2466 HE-LHC*, volume 7, pages 221–584. 12 2019.
- 2467 [52] Xabier Cid Vidal et al. *Report from Working Group 3: Beyond the Standard Model  
2468 physics at the HL-LHC and HE-LHC*, volume 7, pages 585–865. 12 2019.
- 2469 [53] J. Alwall, R. Frederix, S. Frixione, V. Hirschi, F. Maltoni, O. Mattelaer, H.-S. Shao,  
2470 T. Stelzer, P. Torrielli, and M. Zaro. The automated computation of tree-level and  
2471 next-to-leading order differential cross sections, and their matching to parton shower  
2472 simulations. *Journal of High Energy Physics*, 2014(7), Jul 2014.
- 2473 [54] Torbjörn Sjöstrand, Stefan Ask, Jesper R. Christiansen, Richard Corke, Nishita De-  
2474 sai, Philip Ilten, Stephen Mrenna, Stefan Prestel, Christine O. Rasmussen, and Pe-  
2475 ter Z. Skands. An introduction to pythia 8.2. *Computer Physics Communications*,  
2476 191:159–177, Jun 2015.
- 2477 [55] ATLAS Run 1 Pythia8 tunes. Technical Report ATL-PHYS-PUB-2014-021, CERN,  
2478 Geneva, Nov 2014.
- 2479 [56] Stefano Carrazza, Stefano Forte, and Juan Rojo. Parton distributions and event  
2480 generators, 2013.
- 2481 [57] Leif Lönnblad and Stefan Prestel. Merging multi-leg nlo matrix elements with parton  
2482 showers. *Journal of High Energy Physics*, 2013(3), Mar 2013.

- 2483 [58] Christoph Borschensky, Michael Krämer, Anna Kulesza, Michelangelo Mangano, San-  
2484 jay Padhi, Tilman Plehn, and Xavier Portell. Squark and gluino production cross sec-  
2485 tions in  $pp$  collisions at  $\sqrt{s} = 13, 14, 33$  and 100 tev. *The European Physical Journal*  
2486 *C*, 74(12), Dec 2014.
- 2487 [59] T Kawamoto, S Vlachos, L Pontecorvo, J Dubbert, G Mikenberg, P Iengo, C Dal-  
2488 lapiccola, C Amelung, L Levinson, R Richter, and D Lellouch. New Small Wheel  
2489 Technical Design Report. Technical Report CERN-LHCC-2013-006. ATLAS-TDR-  
2490 020, Jun 2013. ATLAS New Small Wheel Technical Design Report.
- 2491 [60] The ATLAS Collaboration. Technical Design Report for the Phase-I Upgrade of the  
2492 ATLAS TDAQ System. Technical Report CERN-LHCC-2013-018. ATLAS-TDR-023,  
2493 Sep 2013. Final version presented to December 2013 LHCC.